ENGINYERIA ELECTRÒNICA ELÈCTRICA I AUTOMÀTICA

UNIVERSITAT ROVIRA I VIRGILI

Graduate Students Meeting on Electronics Engineering

Tarragona, Spain. June 25 - 26, 2015

# BOOK OF ABSTRACTS

DIPUTACIÓ DE TARRAGONA

IEEE

FUNDACIÓ URV

ENGINYERIA ELECTRÒNICA ELÈCTRICA I AUTOMÀTICA

UNIVERSITAT ROVIRA I VIRGILI

Graduate Students Meeting on Electronics Engineering

Tarragona, Spain. June 25 - 26, 2015

# Programme

ENGINYERIA ELECTRÒNICA ELÈCTRICA I AUTOMÀTICA

UNIVERSITAT ROVIRA I VIRGILI

Graduate Students Meeting on Electronics Engineering

Tarragona, June 25th and 26th of 2015

# Programme

## Thursday, June 25th

**15:30 – 15:30 Check-In and Poster Placement**

**15.30 - 15:35 Opening**

**15.35 - 17.00 Oral Presentations from the Doctoral Programme Students**

- **15:35 Fish consumption, omega-3 fatty acids, and NMR lipoprotein subfractions in 26034 apparently healthy women. Núria Amigó et al.** (Sipomics)**.**
- **15:55 Dolphin 1D: Improving automation of targeted metabolomics in multi-matrix datasets of 1H-NMR spectra. Josep Gómez et al.** (Sipomics)
- **16:15 Control en Modo de Deslizamiento de la Tensión de Entrada del Convertidor Buck-Boost Versátil para Aplicaciones Fotovoltaicas. Juan Francisco Méndez et al.** (GAEI)
- **16:35 Limit cycle generation in a self-oscillating parallel resonant converter. Ricardo Bonache et al.** (GAEI)

**17:00 - 18:00: Evening Break and Poster Session**

## Friday, June 26th

**09:30 - 10:45 Invited Talk: Transparent and Flexible Large Area Electronics.**
**Dr. Arokia Nathan.** The Hetero-Genesys Laboratory, Electrical Engineering Division. *Universitat de Cambridge*

**10:45 – 11:00 Coffee break**

**11:00 -12:15 Invited Talk: Wireless power transfer and energy harvesting for RFID and wireless sensors.**
**Dr. Apostolos Georgiadis,** Communication Technologies,. *Centre Tecnològic de Telecomunicacions de Catalunya*

**12:15 -13:30 Invited Talk: Can an engineer fix a cell ?**
**Dr. Jesús Picó Marco,** Control of Complex Systems Group. *Universitat Politècnica de València*

**13:30 – 15:00 Lunch**

**15:00 - 16:30 Oral Presentations from the Doctoral Programme Students**

- **15:00 Wireless identification and positioning of a FSS transponder with a FMCW radar. Javier Lorenzo et al.** (NePhoS)
- **15:20 Interplay between Morphology, Optical Properties and Electronic Structure of Solution-Processed Bi2S3 Colloidal Nanocrystals. Peilin Han et al.** (NePhoS)
- **15:40 Deep cavitand self-assembled on Au NPs-MWCNT as highly sensitive benzene sensing interface. Pierrick Clément et al.** (Minos)
- **16:00 Development of an electronic nose to assess the VOCs profile to identify patients with seasonal allergic rhinitis. Tarik Saidi et al.** (Minos) *Laboratory electronics automatics and biotechnology in University of Moulay Ismail*

**16:30 Closing Session**

ENGINYERIA ELECTRÒNICA ELÈCTRICA I AUTOMÀTICA

UNIVERSITAT ROVIRA I VIRGILI

Graduate Students Meeting on Electronics Engineering

Tarragona, Spain. June 25 - 26, 2015

# Invited Sessions

ENGINYERIA ELECTRÒNICA ELÈCTRICA I AUTOMÀTICA
UNIVERSITAT ROVIRA I VIRGILI
Graduate Students Meeting on Electronics Engineering
Tarragona, June 25th and 26th of 2015

# Transparent and Flexible Large Area Electronics

**Arokia Nathan**

*The Hetero-Genesys Laboratory*
*Electrical Engineering Division, Cambridge University*
*9 JJ Thomson Avenue, Cambridge CB3 0FA, UK*

**Abstract:**
Amorphous oxide semiconductors have opened a new realm of applications whereby transparency and mechanical flexibility associated with low-temperature processing on flexible substrates are important requirements. They are known for their high electron mobility even when processed at room temperature, making oxides a strong candidate for the next-generation thin film transistor (TFT) technology. Compared to existing well-established TFT technologies, the oxide transistor shows superiority in terms of process simplicity and cost, and stable device behaviour in the dark. While its non-uniformity over large areas is comparable to that of thin film silicon transistors, its photo-instability at low wavelengths can be an issue due to persistence in photoconductivity. This talk will review the mechanisms underlying light sensitivity in oxide transistors. Although this class of materials is optically transparent, the presence of oxygen deficiency defects, such as vacancies and interstitials located at gap states, gives rise to absorption of blue and green photons due to their ionization. In particular, the oxygen defects remain ionized even after illuminating, leading to persistent photoconductivity. This can limit the frame-rate of pixelated arrays for imaging and displays. However, despite material weaknesses, considerable progress has been made in designing oxide-based large area flat panel systems. This talk will address the design approaches employed for operationally stable pixel circuits for large area displays and imagers.

**Biography:**
Professor Arokia Nathan holds the Chair of Photonic Systems and Displays in the Department of Engineering, Cambridge University. He received his PhD in Electrical Engineering from the University of Alberta.
Following post-doctoral years at LSI Logic Corp., USA and ETH Zurich, Switzerland, he joined the University of Waterloo where he held the DALSA/NSERC Industrial Research Chair in sensor technology and subsequently the Canada Research Chair in nano-scale flexible circuits. He was a recipient of the 2001 NSERC E.W.R. Steacie Fellowship.
In 2006, he moved to the UK to take up the Sumitomo Chair of Nanotechnology at the London Centre for Nanotechnology, University College London, where he received the Royal Society Wolfson Research Merit Award. He has held Visiting Professor appointments at the Physical Electronics Laboratory, ETH Zürich and the Engineering Department, Cambridge University, UK.
He has published over 500 papers in the field of sensor technology and CAD, and thin film transistor electronics, and is a co-author of four books. He has over 50 patents filed/awarded and has founded/cofounded four spin-off companies. He serves on technical committees and editorial boards in various capacities. He is a Chartered Engineer (UK), Fellow of the Institution of Engineering and Technology (UK), Fellow of IEEE (USA), and an IEEE/EDS Distinguished Lecturer.

ENGINYERIA ELECTRÒNICA ELÈCTRICA I AUTOMÀTICA
UNIVERSITAT ROVIRA I VIRGILI
Graduate Students Meeting on Electronics Engineering
Tarragona, June 25th and 26th of 2015

# Wireless power transfer and energy harvesting for RFID and wireless sensors

**Apostolos Georgiadis**
*Department of Microwave Systems and Nanotechnology*
*Centre Tecnològic de Telecomunicacions de Catalunya (CTTC)*

http://www.cttc.es/people/ageorgiadis/
ageorgiadis@cttc.es

**Abstract:**
RFID technology provides a foundation, an enabling technology towards the realization of 'zero-power' wireless sensors and implementing the Internet-of-Things (IoT) and machine-to-machine (M2M) communication. Interest in RFID technology is further enhanced by its fundamental capability for wireless powering of devices, allowing for battery-less operation. The presentation begins with an overview of ambient energy availability and energy harvesting technology challenges for low power circuits and sensors. Design challenges and novel technologies and materials, such as paper, textiles, and inkjet printing are presented. Special focus is placed on electromagnetic energy transfer and harvesting for range maximization of passive RFID systems. Rectenna design and optimization under different operating conditions and in different operating frequencies from HF to millimeter waves is addressed. Multiple technology harvesters leading to the development of energy harvesting assisted RFIDs are discussed. Low profile and conformal solar antennas and solar-electromagnetic harvesters including examples implemented on paper and textile substrates are presented. The integration of an antenna with a thermo-electric generator is demonstrated. Finally, waveform optimization in wireless power transfer is addressed, and the ability to improve the RF-DC power conversion efficiency of electromagnetic energy harvesting devices by tailoring the characteristics of the transmitted signals is discussed.

**Biography:**
Apostolos Georgiadis was born in Thessaloniki, Greece. He received the Ph.D. degree in electrical engineering from the University of Massachusetts at Amherst, in 2002.
In 2007, he joined Centre Tecnologic de Telecomunicacions de Catalunya (CTTC), Barcelona, Spain, as a Senior Researcher, where he is involved in energy harvesting and radio-frequency identification (RFID) technology and active antennas and antenna arrays.
Since Apr. 2013 he is Coordinating the Microwave Systems and Nanotechnology Department at CTTC. He was the Chair of the 2011 IEEE RFID Technologies and Applications (RFID-TA) Conference. He was the Chair of EU COST Action IC0803, RF/Microwave communication subsystems for emerging wireless technologies (RFCSET) and presently he is vice-Chair of EU COST Action IC1301 on Wireless Power Transfer for Sustainable Electronics.
He serves as an Associate Editor of the IEEE Microwave Wireless Components Letters, IEEE RFID Virtual Journal and IET Microwaves Antennas and Propagation journals. He is past Chair of the IEEE MTTS Technical Committee MTT-24 on RFID Technologies and member of IEEE MTT-26 on wireless energy transfer and conversion.

ENGINYERIA ELECTRÒNICA ELÈCTRICA I AUTOMÀTICA
UNIVERSITAT ROVIRA I VIRGILI
Graduate Students Meeting on Electronics Engineering
Tarragona, June 25th and 26th of 2015

# Can an engineer fix a cell ?

**Jesús Picó Marco**

*Control of Complex Systems Group*
*Universitat Politècnica de València*

https://gcsc.ai2.upv.es//
jpico@ai2.upv.es

**Abstract:**
Industrial biotechnology has traditionally used enhanced and/or genetically modified micro-organisms as cell factories to produce specialty metabolites of importance for the health, chemical, food and energy sectors (e.g. amino acids, vitamins, food additives, biofuels,...). The scientific and technological needs of the field, traditionally an area shared by biology and chemical engineering, are pushing it towards becoming a multidisciplinary one where new emergent technologies and methodologies arise, like Systems and Synthetic Biology. Among the research and technological challenges posed in the field we find:

• Mathematical modelling of microbial metabolism, directed towards both steady state and dynamic models.
• Design of new pathways and synthetic micro-organisms for the synthesis of molecules and products new to nature. • Novel and efficient production systems focusing on protein synthesis and expression to develop new or improved enzymes.
• Optimization of biocatalysts by directed evolution and/or rational design.
• Development of engineering tools to design strategies for process intensification (optimization), such as alternative novel reactor concepts, advanced control strategies and simulation tools for modelling fermentation processes on different scales.

These developments involve multidisciplinary problems integrating expertise, among others, from biology, mathematics, statistics, computer science and engineering.
In this talk we will review some examples of the kind of problems faced at different scales, from the bioreactor level down to the intracellular one, and the solutions that (control) engineering can provide.

**Biography:**

Prof. Jesús Picó got his PhD in Industrial Engineering in 1996. Since 2010 is Full Professor of Automatic Control at the Department of Systems Engineering and Control of the Universitat Politècnica de València (UPV). He has authored or co-authored over 45 papers in journal papers, 10 book chapters, and a large number of conference papers. His works have been cited over 1000 times. He has been principal investigator in national and international research projects, mostly related to application of advanced feedback control strategies to process and biotechnological industry. He is the leader of the Synthetic Biology and BioSystems Control Lab (http://sb2cl.ai2.upv.es) at the Institut d'Automàtica i Informàtica Industrial (ai2) at the UPV.

His main research contributions deal with modeling and control of nonlinear uncertain systems. In particular:

- Interval and posibilistic analysis for modeling and control of systems with structured uncertainty.
- Sliding mode control and observers for fedbatch bioreactors.
- Multiphase PCA and PLS methods for batch proceses monitoring.

Currently he is mostly interested in application of systems engineering and feedback control methodologies to Synthetic Biology. He is instructor of the UPV team at the International Genetically Engineered Machine (iGEM) Competition organized by the M.I.T.

ENGINYERIA ELECTRÒNICA ELÈCTRICA I AUTOMÀTICA

UNIVERSITAT ROVIRA I VIRGILI

Graduate Students Meeting on Electronics Engineering

Tarragona, Spain. June 25 - 26, 2015

# Regular Sessions

# Dolphin 1D: Improving automation of targeted metabolomics in multi-matrix datasets of 1H-NMR spectra.

Josep Gómez[1,2*], Maria Vinaixa[1,2], Miguel A. Rodríguez[1,2], Reza M. Salek[3], Xavier Correig[1,2], Nicolau Canyellas[1,2]

1 Metabolomics Platform, IISPV, Universitat Rovira I Virgili, Campus Sescelades, Carretera de Valls, s/m, 43007 Tarragona, Spain
2 CIBERDEM, Spanish Biomedical Research Centre in Diabetes and Associated Metabolic Disorders, Bonanova 69, 6th floor, 08017 Barcelona, Spain.
3 European Bioinformatics Institute (EMBL-EBI) European Molecular Biology Laboratory, Wellcome Trust Genome Campus Hinxton, Cambridge CB10 1SD, UK
*josep.gomez@urv.cat

## Abstract

Nuclear magnetic resonance (NMR) is one of the main tools applied in the field of metabolomics. Extracting all the valuable information from large datasets of $^1$H-NMR spectra is a huge challenge for high throughput metabolomics analysis. The tools that currently exist to improve signal assignment and metabolite quantification do not have the versatility of allowing the quantification of unknown signals or choosing different quantification approaches in the same analysis. Moreover, graphical features and informative outputs are needed in order to be aware of the reliability of the final results in a field where position shifting, baseline masking and signal overlap may produce errors between samples. Here we present a software package called Dolphin 1D, which aim is to improve targeted metabolite analysis in large datasets of $^1$H-NMR by combining user interactivity with automatic algorithms. Its performance has been tested on a multi-matrix set composed by total serum, urine, liver aqueous extracts and brain aqueous extracts of rat. Our strategy pretends to offer a useful solution for every kind of matrix, avoiding black-box processes and subjectivities user-user in automatic signal quantification.

## 1. Introduction

$^1$H-NMR spectra may contain hundreds of signals coming from a variable number of metabolites. The final number of detectable metabolites depends on the kind of biological matrix, the organism, the sample preparation and the experimental design. All this variability makes extremely difficult the automation of metabolite profiling due to signal overlapping, position shifts and baseline masking .Nowadays, the reliability and time consumption of metabolite profiling in $^1$H-NMR samples depends directly on user experience.

In this paper we perform a metabolite profile analysis in a multi matrix set of total serum, urine, liver aqueous extracts and brain aqueous extracts of rats using a software tool called Dolphin1D which aims to improve the targeted metabolite profile analysis in large sets of $^1$H-NMR spectra. This tool combines an easy and intuitive user interaction with assisted metabolite assignment and different methods of automatic quantification in order to obtain reliable results for posterior statistical analysis and optimize processing times.

## 2. Methods

Dolphin1D works under a very simple and intuitive user-friendly GUI and is able to quantify a flexible set of target signals using easily editable libraries and Region Of Interest (ROI) patterns. A ROI is a spectral window containing relevant signals for metabolite quantification. The tool works with shimmed and phase corrected Bruker spectra as input, and gives the user several options to import the data (in terms of alignment, region suppressions and normalization). When the whole dataset has been imported, the user can choose between a fully automatic high-throughput analysis and a manual supervised analysis. We recommend a manual supervised analysis the first time you work on a new dataset, because it allows the user to verify graphically how the patterns fit the new data. This mode allows the user to edit some parameters to adjust the final pattern to a new experiment before being applied to the whole dataset. For following analysis of previously analyzed data we recommend executing the

fully automatic high-throughput analysis directly (see Figure 1). All the functions are programmed under the matrix calculation platform MATLAB (ver. 7.5.0; The Mathworks, Inc., Natick, MA, USA).

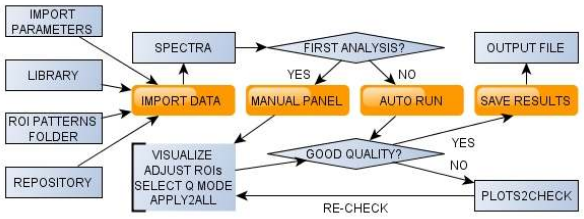


**Fig.1.** Dolphin 1D graphical overview.

The tool facilitates metabolite assignations through signal suggestions in the Manual Panel. These signal suggestions come from an internal curated database built from public databases such as the Human Metabolome Database (HMDB) [1], the Birmingham Metabolite Library [2] and the BioMagResBank (BMRB) [3]. The curation is based on the selection of the most useful signals of the most relevant metabolites which frequently appear in $^{1}$H-NMR spectra of biofluids and tissues according to recent literature.

The user can expand and reduce the library and the number of ROI pattern files, and adjust the features within the ROI patterns to the experiment requirements. In the Manual Panel, the user has the option to plot a single spectrum, all spectra or the average spectrum of a ROI, which is very useful to check graphically the ROI behavior between samples.

Once all signals for a ROI pattern have been chosen the user can try and select which quantification mode is the most appropriate in each case before running it along the whole dataset samples.

## 3. Results & Discussion

We performed a metabolite profile analysis in a total set of 168 spectra of 4 different biological matrices of rat. Figure 3 shows the number of spectra, metabolites, ROI patterns and quantification modes used in each matrix. The signals used for metabolite annotation and quantification appear in the signals repository of Dolphin1D and have been contrasted with the literature and the HMDB. Depending on the baseline conditions, metabolite quantification has been performed using simple bucket integration and two different modes of line-shape fitting. The line-shape-fitting algorithms used for the package are the same used for the previously published tool Dolphin, and its accuracy has been already tested [4].

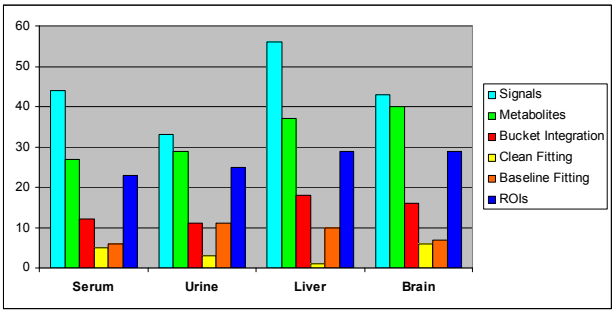


**Fig.3.** Summary of the metabolite profiling in each matrix.

Dolphin1D aim is to quantify a flexible set of target signals using only $^{1}$H-NMR spectra and avoiding black-box processes. The number of signals can be reduced or extended depending on the user criteria, and unknown signals, artifacts and solvents can also be quantified. Dolphin1D rises as the versatile alternative of its predecessor Dolphin, whose dependence of 2-dimensional data is a clear limitation for being applied in large datasets in terms of spectroscopy acquisition times. The new package maintains the automation in terms of quantification along samples but introduces the option of user-editing ROI patterns and visual tools for tracking the process.

## 4. Conclusions

This tool has been created as an evolution of Dolphin in terms of usefulness and versatility for targeted metabolite profiling in $^{1}$H-NMR samples. While new algorithms need to be developed in order to improve automation in metabolite identification and quantification, a package that combines user interaction with automatic assistance can be an optimal solution in order to obtain the most information possible from $^{1}$H-NMR spectra in large datasets. The package has the benefits of fully automatic algorithms for quantification purposes and also the benefits of manual parameters edition and graphical checking for users to be assured their final results are reliable. The package is not matrix dependent and has default libraries and ROI patterns for different biofluids and tissues. A detailed manual of how to use it is now under construction.

**References**

[1] Wishart, DS, et al.: HMDB 3.0-The Human Metabolome Database in 2013. Nucleic Acids Research 41 (January 2013) D801-D807

[2] Ludwig, C, et al.: Birmingham Metabolite Library: a publicly accessible database of 1-D H-1 and 2-D H-1 J-resolved NMR spectra of authentic metabolite standards (BML-NMR). Metabolomics 8 (Febrary 2012) 8-18

[3] Ulrich, E.L. et al.: BioMagResBank. Nucleic Acids Research 36 (January 2008) D402-D408

[4] Gómez, J et al.: Dolphin: a tool for automatic targeted metabolite profiling using 1d and 2d H-1-NMR data. Analytical and Bioanalytical Chemistry 406 (December) 7967-7976

# Control en Modo de Deslizamiento de la Tensión de Entrada del Convertidor Buck-Boost Versátil para Aplicaciones Fotovoltaicas.

Mendez-Diaz, F.; Ramirez-Murillo, H.; Calvente, J.; Giral, R.

Departament d'Enginyeria Electrònica, Elèctrica i Automàtica, ETSE, Universitat Rovira i Virgili.

***Abstract*— El convertidor buck-boost versátil presenta interesantes características tales como corrientes de entrada y salida continuas o su facilidad de control tanto en modo elevador como en modo reductor. Este trabajo aborda su utilización en aplicaciones fotovoltaicas en las que la característica estática I-V de tipo fuente de corriente no lineal de los módulos fotovoltaicos hace necesaria la inclusión de un condensador de entrada en la estructura original del convertidor.**

## I. INTRODUCCIÓN

EN este trabajo se plantea la substitución del convertidor elevador por el convertidor elevador-reductor versátil propuesto en [1]–[2] cuya corriente de salida es continua y fácilmente controlable cuando ello sea necesario.

La posibilidad de utilizar una característica de reducción permitiría utilizar baterías de tensión inferior a la del MPP nominal, dando mayor flexibilidad al diseñador en el caso de cargas de tensión nominal también inferior. Centraremos este trabajo en el estudio del control en modo de deslizamiento del convertidor buck-boost versátil bidireccional.

## II. ANÁLISIS TEÓRICO.

Esta investigación toma como punto de partida principal [3] donde se estudia el control de la tensión de entrada. A diferencia de [3] donde solo se consideró el control proporcional del error de tensión, se agrega una sexta ecuación de estado a las cinco ecuaciones de estado originales de la etapa de potencia. La sexta ecuación corresponde al termino integral agregado para eliminar el error en estado estacionario.

Escogemos la misma función de conmutación propuesta en [4] basada en la corriente del condensador $C_g$ que pretende que la tensión de entrada $v_g$ siga a una referencia externa $v_r$. Agregando el término integral para compensar los efectos de la no linealidad como perdida y retrasos la superficie de deslizamiento será:

$$S(x) = i_{pv} - i_g + G\left(v_g - v_r\right) + k(int_{err}) = \\ = C_g \frac{dv_g}{dt} + G\left(v_g - v_r\right) + k(int\_err) = 0 \quad (1)$$

La función de transferencia entre la tensión de entrada y la tensión de la referencia es:

$$H(s) = \frac{V_g(s)}{V_r(s)} = \frac{Gs+k}{C_g s^2+Gs+k} \quad (2)$$

Como se puede observar los dos polos se encuentran en el semiplano izquierdo si G>0, $C_g > 0\ y\ k > 0$

Tomando en consideración las mismas operaciones [3], el convertidor buck-boost versátil opera como un convertidor reductor con filtro de entrada o como un convertidor elevador con filtro de salida.

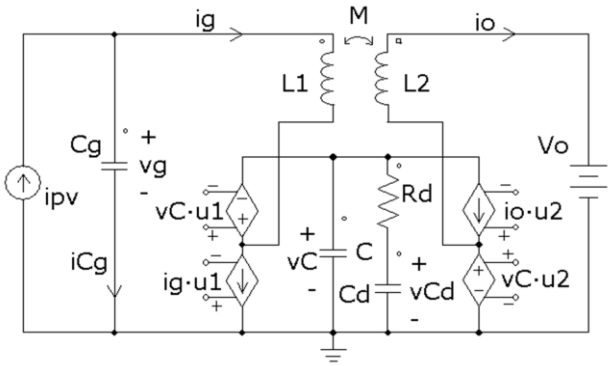


Fig. 1. Modelo simplificado del sistema panel-convertidor-batería.

Para el análisis, se ha utilizado el modelo circuital simplificado de la Fig. 1, en el que se han sustituido los interruptores por fuentes de tensión y corriente controladas [5].

Para describir el sistema en lazo abierto se utilizan las mismas cinco ecuaciones diferenciales de la forma $\frac{dx}{dt} = f(x, u_1, u_2)$ [4] agregando ahora la parte integral en forma de ecuación y una variable más al vector de estado definida por $int\_err$, quedando el vector de estado de la siguiente manera

$$x = \left[i_g, i_o, v_C, v_{Cd}, v_g, int\_err\right]^T$$

### A. *Modo buck:* $u_1 = 1, f(x, 1, u_2) = f_{buck}(x, u_2)$

Para comprobar que existe deslizamiento en modo buck con la superficie de conmutación propuesta en (1), vamos a proceder a determinar el control equivalente.

$$u_{2eq} = \frac{v_o}{v_c} + \frac{L_2}{M}\left(1 - \frac{v_g}{v_c}\right) + \\ + \frac{L_1 L_2 - M^2}{M v_c}\left[\frac{G}{C_g}\left(i_{pv} - i_g\right) + k(v_g - v_r) + \frac{di_{pv}}{dt} - G\frac{dv_r}{dt}\right] \quad (3)$$

Es importante que exista acopló magnético ($M$ = 0) de lo contrario el control equivalente en modo buck $u_{2eq}$ tiende a infinito.

La dinámica de deslizamiento ideal (lazo cerrado) se obtiene substituyendo $u_{2eq}$ por el control equivalente en $f_{buck}(x, u_2)$ e imponiendo que $S(x) = 0$. Al igual que [3] tomamos los mismos supuesto es decir, Imponiendo que, tanto las derivadas de las variables de estado $f_{buck}(x, u_{2eq}) = 0$,

como las derivadas de las entradas $\frac{dw}{dt} = 0$ ($W = [I_{pv}, V_o, V_r]^T$) sean cero obtenemos el punto de equilibrio $X = \left[I_{pv}, \frac{V_r I_{pv}}{V_o}, V_r, V_r, V_r, 0\right]^T$ que es el que cabe esperar en un buck con filtro de entrada ideal. Linealizando la dinámica de deslizamiento ideal en torno al punto de equilibrio obtenemos la expresión del polinomio característico de cuarto orden siguiente:

$$\left(s^2 + \frac{G}{C_g}s + \frac{k}{C_g}\right)(s^3 + a_2 s^2 + a_1 s + a_0) \qquad (4)$$

$$a_2 = \frac{1}{R_d}\left(\frac{1}{C_d} + \frac{1}{C}\right) + \frac{I_{pv}}{V_O C}\left(\frac{L_2}{M} - \frac{V_O}{V_r}\right) \; a_1 = \frac{V_O}{V_r MC} + \frac{I_{pv}}{V_O R_d C_d C}\left(\frac{L_2}{M} - \frac{V_O}{V_r}\right) \; a_0 = \frac{V_O}{V_r R_d C_d C M}$$

Uno de los puntos más importantes del polinomio característico (4) es que uno de sus polos es el que hemos impuesto en la dinámica de deslizamiento (1), y que habíamos anticipado en (2) el cual simplifica el análisis de estabilidad. El sistema es estable en modo Buck ($V_O < V_r$) si $L_2 > M > 0$.

## III. EJEMPLO

Los parámetros del convertidor son los siguientes: $L_M = L_A = L_B = 22\ \mu H$, $C_g = 44\ \mu F$, $C = 10\ \mu F$, $C_d = 44\ \mu F$,(100 $\mu F$) $R_d = 1\ \Omega$. Se desea que la frecuencia de conmutación en el punto de trabajo nominal, $V_g = 18\ V$, $V_o = 12{,}8\ V$, sea aproximadamente de 90 kHz por lo que se han ajustado la ganancia y el ancho de histéresis del comparador del lazo de control para conseguirlo. También se ha seleccionado $G = 6\ S$, $k = 22000\ Ss$ en la superficie (1), lo que corresponde a una función de transferencia según (2) y en (5)

$$H(s) \approx 136400\,\frac{s+3670}{(s+3770)(s+132600)}. \qquad (5)$$

En el punto de trabajo nominal (modo buck), el resto de los polos, según (9), son las raíces de $(s^3 + a_2 s^2 + a_1 s + a_0) \approx (s + 107400) \cdot ((s + 13000)^2 + 22700^2)$.

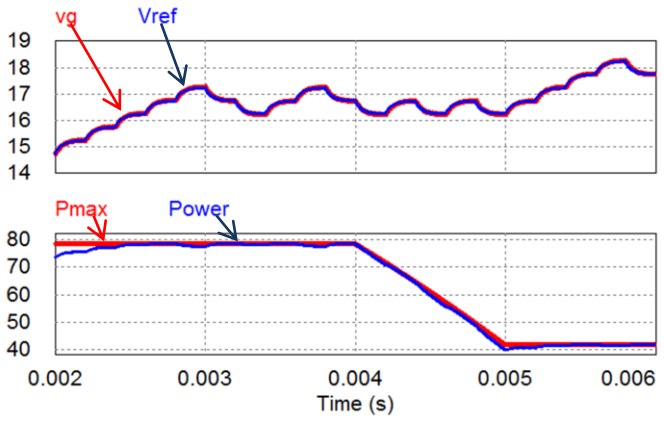


Fig. 2. En la gráfica superior se parecía la simulación de la tensión de entrada siguiendo a la referencia activando MPPT. En la gráfica inferior se aprecia la potencia máxima que puede suministrar el módulo PV y la potencia instantánea extraída realmente del módulo.

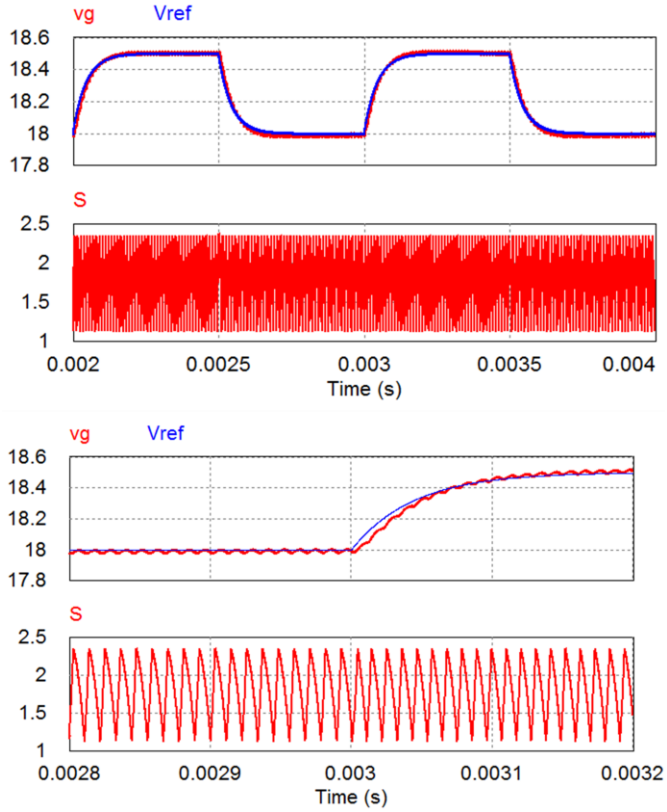


Fig. 3. Simulación de la tensión de entrada y de la señal de referencia.

La Fig. 3 muestra resultados de una primera simulación del convertidor en modo Buck en dos diferentes periodos en los cuales se ve que la tensión de entrada sigue a una referencia variable que oscila a 1 kHz entre 18 V y 18,5 V. donde el error en estado estacionario desaparece.

## IV. CONCLUSIONES

Tras realizar un análisis teórico, se ha comprobado por simulación que es posible realizar un control en modo de deslizamiento a frecuencia de conmutación variable de la tensión de entrada del convertidor buck-boost versátil en una aplicación fotovoltaica.

## REFERENCES


[1] C. Restrepo, J. Calvente, A. Cid-Pastor, A. El Aroudi, and R. Giral, "A Noninverting Buck–Boost DC–DC Switching Converter With High Efficiency and Wide Bandwidth," *IEEE Trans. Power Electron.*, vol. 26, no. 9, pp. 2490–2503, Sep. 2011.

[2] C. Restrepo, T. Konjedic, J. Calvente, M. Milanovic, and R. Giral, "Fast Transitions Between Current Control Loops of the Coupled-Inductor Buck–Boost DC–DC Switching Converter," *IEEE Trans. Power Electron.*, vol. 28, no. 8, pp. 3648–3652, Aug. 2013.

[3] Mendez Diaz F, Ramirez Murillo H, Garces P, Romero A, Clavente J, Giral R. "Control en Modo Deslizante de la Tension de Entrada del Convertidor Buck-Boost Versatil para Aplicaciones Fotovoltaicas". en SAEI 2014, pp 1-6.

[4] D. Gonzalez-Montoya, C. A. Ramos-Paja, and R. Giral, "A new solution of maximum power point tracking based on sliding mode control," in *IECON 2013 - 39th Annual Conference of the IEEE Industrial Electronics Society*, 2013, pp. 8350–8355.

[5] E. Van Dijk, J. N. Spruijt, D. M. O'Sullivan, and J. B. Klaassens, "PWM-switch modeling of DC-DC converters," *IEEE Trans. Power Electron.*, vol. 10, no. 6, pp. 659–665, 1995.

# Limit cycle generation in a self-oscillating parallel resonant converter

R. Bonache Samaniego*, C. Olalla, L. Martínez Salamero

Department of Electrical, Electronic and Control Engineering

Rovira i Virgili University. Tarragona, Spain

*ricardo.bonache@urv.cat

**Abstract**

A mathematical model is derived for a self-oscillating parallel resonant converter in which a simple comparator applied to the inductor current is used to establish stable oscillations at the resonant frequency in cases of high Q. Second order differential equations are solved to construct a piecewise phase-plane trajectory explaining the generation of a stable limit cycle and predicting its amplitude and period. Measurements in a 60 W parallel resonant converter prototype oscillating around 500 kHz are in good agreement with the theoretical predictions.

## 1. Introduction

The basic problem underlying a self-oscillating behaviour in resonant converters is to find the parametric conditions for the existence of the resulting limit cycle together with an accurate prediction of its amplitude and period [1]. In this paper, we explain the generation of the limit cycle under the optics of a variable structure system with a switching surface where no sliding regime can exist, given that the trajectories in either side of the boundary move away from it [2]. The phase trajectories of the two substructures involved in the parallel resonant converter are combined to generate a growing spiral starting from the origin of the phase-plane [3] and eventually becoming an ellipse when reaching the attracting perimeter of the limit cycle.

## 2. Limit cycle generation

Variable structure systems (VSS) are systems whose physical structure is changed in accordance with the actual state of the system. The circuit structure of the parallel resonant converter is shown in Fig. 1. A VSS may be synthesized in the PRC by composing the portions of the trajectories of $T_{ON}$ and $T_{OFF}$ intervals.

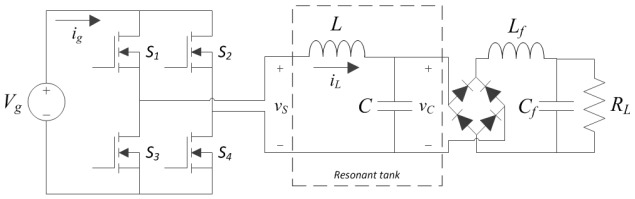


**Fig. 1**. Power stage of a parallel resonant converter.

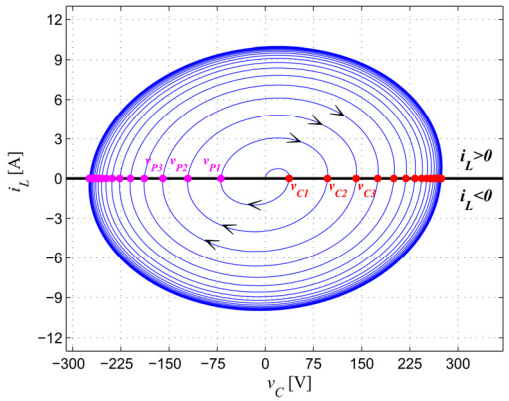


**Fig. 2**. VSS made up of the two substructures of the PRC ($C = 10.5\,nF$ , $L = 8\,\mu H$ , $R_{eq} = 300\,\Omega$ , $V_g = 20\,V$)

The structure-control law may be stated as

- Network topology $T_{ON}$ holds for $i_L(t) > 0$
- Network topology $T_{OFF}$ holds for $i_L(t) < 0$

Their composition results in a growing spiral that eventually becomes an ellipse representing a limit cycle as shown in Fig. 2, which corresponds to sustainable oscillations of $v_C(t)$ and $i_L(t)$.

Provided that a sufficiently large Q factor is ensured, two successive zero crossing points of the spiral corresponding to the trajectory intersection with axis $i_L = 0$ during the $T_{on}$ subinterval are related by the following recurrence

$$v_{C(K+1)} = V_g(1 + e^{-\xi\pi})^2 + v_{C(K)}e^{-2\xi\pi} \qquad (1)$$

where K=[ 1, 2, 3, …], $\xi$ is the damping factor defined by $\xi = \sqrt{LC}\,/\,2CR_{eq}$ and $R_{eq} = R_L\pi^2\,/\,8$. In the PRC, the $Q$ factor is defined as $R_{eq}\,/\,\sqrt{L/C}$, hence under conditions of high $Q$, it is apparent that $\xi << 1$, and the stability of this recurrence is assured by the fact that $e^{-2\xi\pi} < 1$, which guarantees stable self-oscillation at all times, as shown in Fig.3. Defining the maximum amplitude of the limit cycle as $V_C$, it can be derived

$$V_C = V_g\left(\frac{1+e^{-\xi\pi}}{1-e^{-\xi\pi}}\right) \qquad (2)$$

The period of the limit cycle will be given by

$$T = \frac{2\pi}{\omega_0} \qquad (3)$$

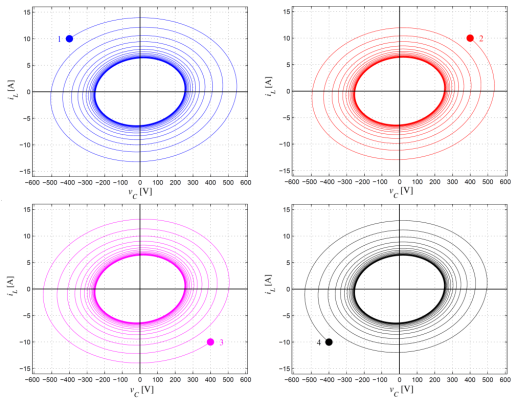

**Fig. 3.**Trajectories reaching the limit cycle from different initial conditions.

which is the period of the steady-state sinusoidal waveforms $v_C(t)$ and $i_L(t)$ at resonant frequency, being $\omega_0$ the resonant frequency.

## 3. Experimental results

An experimental prototype of the PRC with the converter parameters used in the simulations of Fig. 2 and the VSS control based on the sign of the inductor current has been implemented. Fig.4 shows the circuit diagram of both power stage and VSS controller.

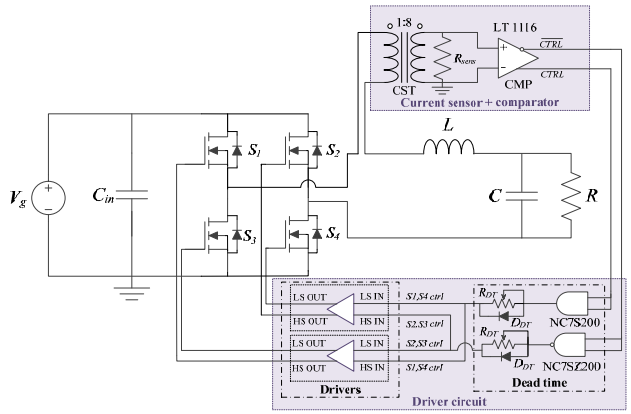


**Fig. 4.** Implementation diagram of the parallel resonant converter with the proposed VSS-based controller.

Steady-state waveforms of the PRC in self-oscillating mode are shown in Fig. 5 with an oscillation frequency of 547 kHz while supplying 57 W to the load with an efficiency of 90 %. The corresponding experimental generation of the limit cycle for self-oscillating mode is illustrated in Fig. 6

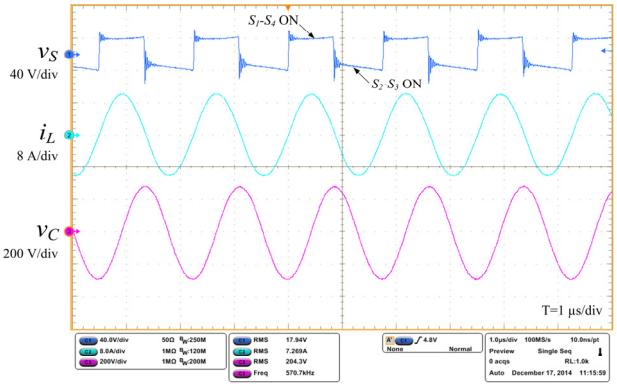


**Fig. 5.** Experimental waveforms of the PRC with VSS control

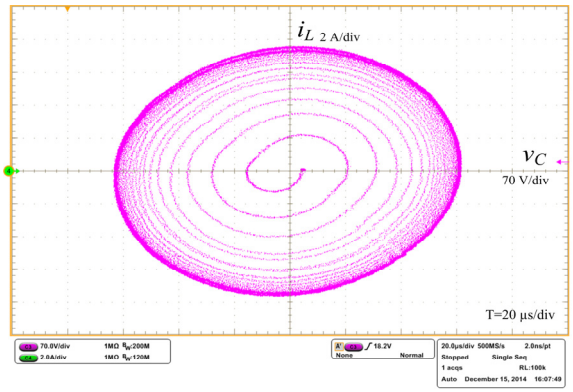


**Fig. 6.** Experimental phase-plane trajectory on closed-loop

## 4. Conclusions

The generation of a limit cycle in a self-oscillating high-$Q$ PRC under a VSS control law has been explained and the amplitude and frequency of the limit cycle calculated. The control mechanism is simple and it is based on the change of sign of the inductor current. Experimental results are in good agreement with the theoretical predictions and confirm that the implemented VSS control law is able to operate at the maximum resonant frequency, provided that a certain minimum value of $Q$ is used.

Potential applications of self-oscillating resonant converters are induction heating [6], LED driving [7] or power interfacing of photovoltaic systems [8].

## References


[1] Williams, D., Bingham, C., Foster, M., Stone, D.: 'Hamel locus design of self-oscillating DC-DC resonant converters', IET Power Electronics, 2010, 3, (1), pp. 86

[2] Utkin, V., Guldner, J., and Shi, J.: 'Sliding mode control in electromechanical systems' (CRC Press, 2nd edition, Taylor and Francis Group, 2009)

[3] Erickson, R.W., and Maksimovic, D.: 'Fundamentals of Power Electronics' (2nd. Ed. Norwell, MA. Kluver, 2001)

[4] Langmuir, R.W.: 'Repetitively switched circuits', IEEE Trans. on Aerospace and Electronic Systems, 1973, 9, (1), pp. 59-64

[5] Babaa, I.M.H., Wilson, T.G., Yu, Y.: 'Analytic solutions of limit cycles in a feedback regulated converter system with hysteresis', IEEE Trans. on Automatic Control, 1968, 13, (5), pp. 524-531

[6] Lucia, O., Carretero, C., Burdio, J.M., et al: 'Multiple-Output Resonant Matrix Converter for Multiple Induction Heaters', IEEE Transactions on Industry Applications, 2012, 48, (4), pp. 1387-1396

[7] Teodosescu, P.D., Bojan, M., and Marschalko, R., 'Resonant Led Driver with Inherent Constant Current and Power Factor Correction', Electronics Letters, 2014, 50, (15), pp. 1086-1088.

[8] Kuei-Hsiang, C., Chun-Hao, H.: 'Bidirectional DC-DC soft-switching converter for stand-alone photovoltaic power generation systems', IET Power Electronics, 2014, 7, (6), pp. 1557-1565

# Wireless identification and positioning of a FSS transponder with a FMCW radar

J. Lorenzo, A. Lázaro, R. Villarino, D. Girbau

Dept. of Electronics, Electrics and Automatic control Engineering, Rovira i Virgili University, Av.Països Catalans 26, 43007 Tarragona, Spain

## Abstract

This paper describes an actively-controlled frequency selective surface (FSS) to implement a backscatter transponder. The FSS is composed by dipoles loaded with switching PIN diodes. The transponder exploits the change in the radar cross section (RCS) of the FSS with the bias of the diodes to modulate the backscattered response of the tag to the FMCW radar. The basic operation theory of the system is explained here. An experimental setup based on a commercial X-band FMCW radar working as a reader is proposed to measure the transponders. The transponder response can be distinguished from the interference of non-modulated clutter, modulating the transponder's RCS. Experimental results at several distances are provided.

## 1. Introduction

FMCW (Frequency Modulated Continuous Wave) radar differs from pulsed radar in that an electromagnetic signal is continuously transmitted [1]. The FMCW radar emits a RF signal that is usually swept linearly in frequency. The received signal is then mixed with the emitted signal and due to the delay caused by the time of flight for the reflected signal, a frequency difference, called beat frequency, is produced. The range from the radar to the target is proportional to the beat frequency. Due to their ability to determine range, FMCW based systems are commonly used for measuring distances in applications such as tank level gauging, where high resolution non-contact measurements in harsh conditions are required [2]. In recent years, FMCW radar has been proposed in the literature for wireless local positioning systems [3]. The major challenges for wireless local positioning systems are disturbances caused by the multipath reflections. In order to mitigate these common problems, a modulated backscatter transponder has been proposed in [4].

The frequency selective surfaces (FSS) are periodic structures in each direction of the plane which act as a filter. This filter property has been exploited in several applications [5]. FSS can be frequency tunable, introducing some switching elements (e.g. PIN diode) [6] or tuning elements (e.g. varactors). Depending on the diode state, the frequency response of the FSS is shifted. Therefore, a large differential radar cross section (RCS) can be achieved over a large frequency bandwidth. This frequency bandwidth is often difficult to reach if backscatter transponders based on low-profile antennas such as patch antennas are used. Another challenge is the transponder detection. This can be improved increasing the differential radar cross section (RCS). To this end, an array of antennas can be used. However, increasing the number of FSS elements, the differential RCS can be easily increased as will be shown in this work. The cost that must be paid is an increase of the power consumption due to the large number of diodes during the forward state. However, reasonable values of RCS can be achieved with a small number of dipoles, for example with 10 dipoles with a current consumption of 2 mA assisted by a 3 V battery.

## 2. Tag based on FSS structure

A block diagram of the proposed system is shown in Fig. 1. It is composed by the tag and the reader. In this case, a FMCW radar is used as a reader enabling the measurement of the tag to reader distance. The radar interrogates the tag which answers modulating its RCS. Depending on the application, data from sensors or identification codes can be sent back to the reader.

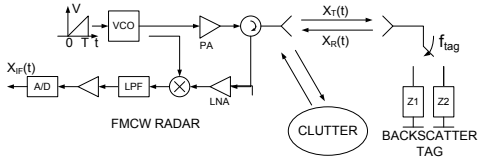


**Fig. 1.** Schematic block diagram of a FMCW radar using a modulated backscatter tag.

The tag consists of a FSS loaded with PIN diodes that modulate the backscattered field of the tag (see Fig.2). The IF-signal at the output of the mixer and low-pass filtered can be expressed as:

$$x_{IF}(t) = A''\cos(2\pi(f_{tag} + \mu\tau)t + \phi_1) + A''\cos(2\pi(f_{tag} - \mu\tau)t + \phi_2) \quad (1)$$

where A'' is the amplitude at the IF-output, and $\phi 1$, $\phi 2$, are phase constants generated from the mixing process that do not influence in the result. The two cases

(non-modulated tag and modulated target) are schematically shown in Fig.3. In Fig.3a the tag is difficult to be distinguished due to the phase noise and it is interfered by the strong clutter reflections. Whereas when the tag is modulated (Fig.3b) a pair of peaks appears around $f_{tag}$ whose separation is proportional to the distance

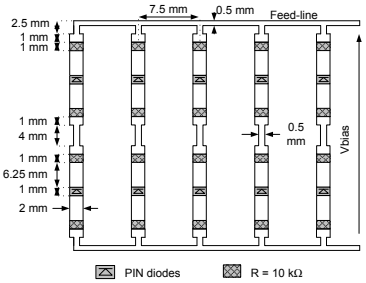


**Fig. 2.** Diagram of a designed FSS.

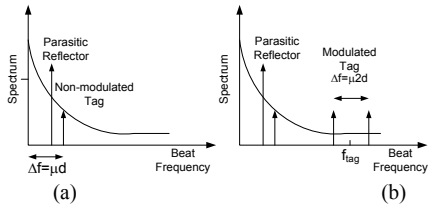


**Fig. 3.** Spectrum after low-pass filter in the IF stage: (a) Non-modulated Tag (b) Modulated Tag.

## 3. Measurements and results

The FSS are designed using Rogers 4003 substrate ($\varepsilon_r$=3.54, tanδ=0.003, and height of 32 mil). The FSS are designed to cover the frequency band between 9.25 GHz and 10.75 GHz, which is the frequency band of the radar used in the experimental results (Siversima model RS3400X). Low-cost NXP BAP51-03 PIN diodes are selected to reconfigure the response of the FSS. Fig. 4 shows the differential RCS obtained subtracting the complex RCS for the two states.

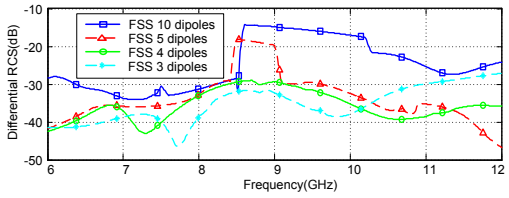


**Fig. 4.** Differential RCS of different tags as function of the number of dipoles.

This figure shows that the level of the differential RCS increases because the effective area of the FSS increases, but also that the bandwidth increases with the number of dipoles. Fig. 5 shows results at 10 m distance. Without modulation, the tag signal cannot be detected because it is masked by the strong reflection of the reflector, clutter and phase noise interference. However, when the tag is modulated, two peaks appear at the spectrum of the IF signal around the frequency modulation. Furthermore, some clutter removal can be achieved if the non-modulated signal is subtracted. Fig. 6 shows the maximum deviation error in the measurement of the distance.

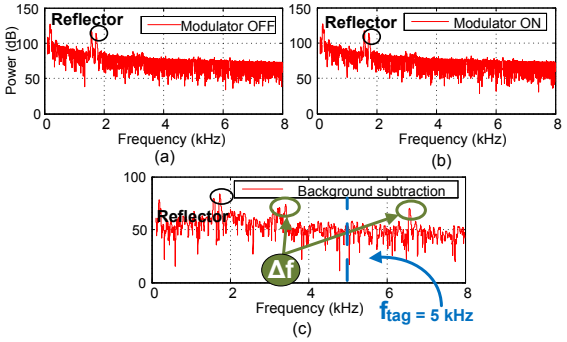


**Fig. 5.** Measurement comparison of the tag and the reflector at 10 m. Tag measurements in case of no modulation, or with $f_{tag}$=5 kHz modulation.

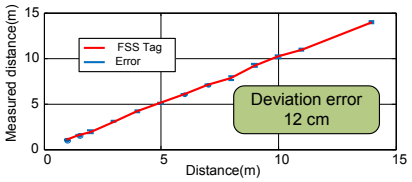


**Fig. 6.** Maximum deviation error measuring the distance of the transponder with the two peaks of modulation

## 4. Conclusions

This work has studied the feasibility to use actively controlled frequency selective surfaces (FSS) with FMCW radars. The communication between the tag and the reader is produced using the backscattering technique. The basic operation theory of the system is explained. In order to increase the tag detection the maximization of the differential RCS is required. Given that the RCS is modulated, interference from non-modulated clutter can be removed using a simple background subtraction technique. An experimental setup based on commercial low-power FMCW radar working as a reader is proposed to measure the modulated RCS of the tags. Good results are obtained up to 11 m in spite of the presence of a reflector.

### References


[1] SKOLNIK, M.I., Introduction to Radar Systems , 2nd ed. Singapure: McGraw-Hill , 1981.

[2] BRUMBI, D. Low power FMCW radar system for level gauging. In IEEE MTT-S International Microwave Symposium Digest. Boston, MA (USA), 2000, vol.3, p.1559–1562.

[3] VOSSIEK, M., ROSKOSCH,R. HEIDE,P. Precise 3-D object position tracking using FMCW radar. In 29th European Microwave Conference, Munich (Germany), 1999, vol. 1, p.234-237.

[4]THORNTON J., EDWARDS, D.J. Range measurement using modulated retro-reflectors in FM radar system. IEEE Microwave Guided Wave Lett., 2000, vol. 10, p. 380–382.

[5] MUNK, B.A. Frequency selective surfaces. New York: Wiley, 2000.

[6]IZQUIERDO, B. S., PARKER, E. A. , ROBERTSON, J. B., BATCHELOR, J. C. Tuning technique for active FSS arrays. Electron.Letters, 2009, vol. 45, p.1107–1109.

# Deep cavitand self-assembled on Au NPs-MWCNT as highly sensitive benzene sensing interface

Pierrick Clément, Saša Korom, Claudia Struzzi, Enrique J. Parra, Carla Bittencourt, Pablo Ballester, Eduard Llobet

P. Clément, Dr. E. J. Parra, Pr. E. Llobet
MINOS-EMaS, Universitat Rovira i Virgili, Avenida Paisos Catalans 26, 43007, Tarragona, Spain
E-mail: eduard.llobet@urv.cat; pierrick.clement@urv.cat
S. Korom, Prof. P. Ballester
Institute of Chemical Research of Catalonia (ICIQ), Av. Països Catalans 16, 43007, Tarragona, Spain
C. Struzzi, Dr. C. Bittencourt
ChIPS, Université de Mons, Place du Parc 23, 7000 Mons, Belgium

## Abstract

The unprecedented sensitivity and partial selectivity of quinoxaline-walled thioether-legged deep cavitand functionalized multiwall carbon nanotubes toward traces of benzene vapors is presented. The cavitand is grafted onto gold nanoparticle (Au-NP) decorated oxygen plasma treated multiwall carbon nanotubes (O-MWCNT) by a self-assembled monolayer process affording a product referred to as cav-Au-MWCNT. The cav-Au-MWCNT resistive gas sensor operates at room temperature with a fully reversible response and shows an outstanding performance toward traces of benzene vapors. The detection of 2.5 ppb of benzene in dry air is demonstrated with a limit of detection (LOD) near 600 ppt.

## 1. Introduction

Benzene is listed among the most harmful volatile organic compounds (VOC). According to the Directive 2008/50/EC of the European Parliament and of the Council of May 2008, the limit value for the annual average exposure to benzene is 5 μg $m^{-3}$ (1.6 ppb). Benzene is present in the petrochemical industry, land reclamation, petroleum coke oven operators, petrol stations, motor vehicle repair stations, roadside works and many other industries. Their activities may result in active exposure to benzene and would clearly benefit from affordable, portable, highly sensitive and selective detectors able to run continuous measurements. The shallow aromatic cavity present in the resorcin[4]arene parent compound modified by installing bridging groups at the upper rim, called quinoxaline-bridged resorcin[4]arene cavitands are known to bind aromatic guests (e.g. benzene, toluene, fluorobenzene), not only in the liquid, but also in the gas phase.[1] Here we describe a simple experimental procedure to prepare an unprecedented type of resistive gas sensing device that employs gold nanoparticle (Au-NP) decorated oxygen-functionalized multiwall carbon nanotubes (O-MWCNTs). The Au-NPs are functionalized after deposition on the O-MWCNTs with quinoxaline-walled thioether-legged cavitand leading to highly sensitive molecular recognition of benzene vapors. Additionally, we explored the sensitivity of the sensor towards others air pollutants such as toluene, *o*-xylene, carbon monoxide, and ethanol vapors in order to evaluate cross sensitivity.

## 2. Results and discussion

The gas sensitive, hybrid nanomaterial was prepared by employing a three-step approach. In the first step MWCNTs were treated with oxygen in plasma to create surface oxygenated defects referred to as O-MWCNT.[2] In the second step, the O-MWCNTs were decorated with Au nanoparticles by means of RF-sputtering and finally, in the third step the Au-decorated and oxygen plasma treated MWCNTs (Au-MWCNT) were functionalized with a self-assembled monolayer of cavitand to produce a desired hybrid material (cav-Au-MWCNT). The homogeneous dispersion of Au nanoparticles (average diameter ~ 2 nm) on MWCNTs shows that SAM procedure, implemented for Au-MWCNTs functionalization with the cavitand, promoted aggregation of the previously deposited Au-NPs (with cluster diameters ranging from 10 to 15 nm shown in **Fig. 1.**). The immersion of Au-MWCNTs in a chloroform solution of the cavitand (0.5 mM) under mild heating (60°C), as required by the SAM technique, favored both the cavitand assembly on the Au-NPs and their aggregation on the MWCNTs.

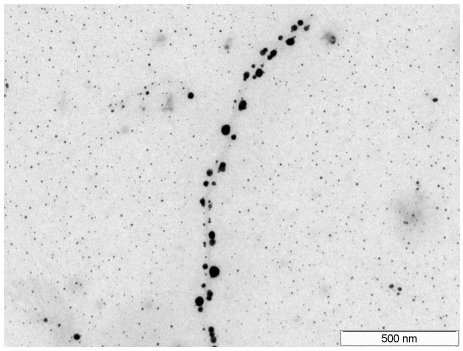


**Fig. 1:** a) typical TEM image of cav-Au-MWCNTs.

Typical response curves for the cav-Au-MWCNT sensor exposed to benzene, toluene, *o*-xylene, ethanol and carbon monoxide is shown in **Fig.2**. This sensor showed significantly higher sensitivity to benzene than to the other tested pollutants. At 100 ppb level of benzene, the sensor is seven and thirty times more responsive than to toluene or *o*-xylene, respectively. Furthermore, the slope of the calibration curve (*i.e.* sensitivity) was calculated for the two lowest tested concentrations and was found to be much higher in the case of benzene ($4.2 \times 10^{-3}$ % $ppb^{-1}$) than for toluene ($1.1 \times 10^{-4}$ % $ppb^{-1}$) and o-xylene ($3.3 \times 10^{-5}$ % $ppb^{-1}$). Therefore, the sensor should be able to detect with high sensitivity traces of benzene in the presence of toluene and/or *o*-xylene. The responses to ethanol and carbon monoxide were significantly lower. In summary, the sensor is partially selective toward benzene and a possible strategy for further enhancing selectivity (beyond the scope of this paper) would be to use an array of sensors with different sensitive layers together with a pattern recognition engine.[3, 4] Taken together, these results demonstrate an unprecedented high sensitivity of the cav-Au-MWCNT sensor for benzene.

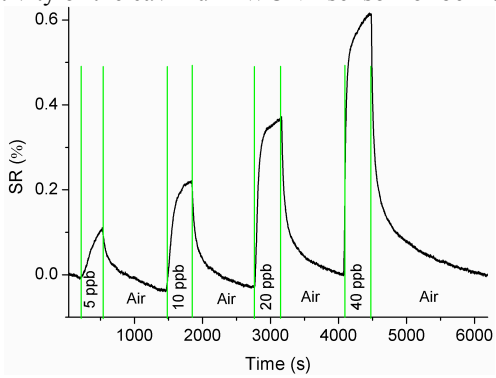


**Fig. 2:** A typical cav-Au-MWCNT sensor resistance response in function of benzene concentration in air; we employed a gas flow of 200 mL $min^{-1}$.

To the best of our knowledge, this is the first system that can detect such a low level of benzene in the gas phase by employing a CNT-based material.Even at very low benzene levels, the response of the sensor was highly reproducible. Thanks to the low levels of noise in the response signals, the theoretical LOD for the sensors was calculated to be 600 ppt, which corresponds to a sensor response three times higher than the level of the noise.[5] The responses to benzene provided by the Au-MWCNT sensor were tested for comparison. The Au-MWCNT sensor was not responsive to benzene vapor levels under 60 ppb in dry conditions. Even at this concentration (60 ppb), the response was low. This observation is in good agreement with theoretical findings that predict a very weak binding energy and the lack of charge transfer between the benzene molecule and the Au-MWCNTs system.

## 3. Conclusion

A simple technique for functionalizing multiwall carbon nanotubes, in view of designing a gas sensor with superior performance, has been introduced. A quinoxaline-walled thioether-legged cavitand **4** is attached onto oxygen plasma treated Au-NP decorated MWCNTs. The technique is suitable for the mass production of described hybrid sensing nanomaterial at low production costs, allowing cost-effective commercialization. The cavitand-functionalized MWCNT sensor shows unprecedented high sensitivity toward low levels of benzene in dry air at trace levels. The detection of 2.5 ppb is demonstrated experimentally and a theoretical LOD of 600 ppt was calculated. Furthermore, sensor response towards toluene and *o*-xylene is significantly lower, clearly showing the strong response for benzene, what is the first example of such selective carbon nanotube based material. Finally, it is worth mentioning that both the detection and the recovery of the baseline are performed at room temperature, which implies that these sensors can operate at very low power consumption. This makes the sensor suitable for being integrated in hand-held portable analyzers, wearable detectors and semi-passive radio frequency identification tags with sensing capabilities or in the nodes of wireless sensor networks with a wide range of potential applications in environmental monitoring, workplace safety or medical devices, among others.

### References

[1]M. Vincenti*, et al.*, "Host-guest complexation in the gas phase by desorption chemical ionization mass spectrometry," *Journal of the American Chemical Society,* vol. 112, pp. 445-447, 1990.

[2]I. Suarez-Martinez*, et al.*, "Probing the interaction between gold nanoparticles and oxygen functionalized carbon nanotubes," *Carbon,* vol. 47, pp. 1549-1554, 2009.

[3]B. Wang*, et al.*, "Artificial sensing intelligence with silicon nanowires for ultraselective detection in the gas phase," *Nano letters,* vol. 14, pp. 933-938, 2014.

[4]G. Konvalina*, et al.*, "Sensors for breath testing: from nanomaterials to comprehensive disease detection," *Accounts of chemical research,* vol. 47, pp. 66-76, 2013.

[5]D. MacDougall*, et al.*, "Guidelines for data acquisition and data quality evaluation in environmental chemistry," *Analytical Chemistry,* vol. 52, pp. 2242-2249, 1980.

# Development of an electronic nose to assess the VOCs profile to identify patients with seasonal allergic rhinitis

T. Saidi[1], K.Tahri[1], M. Guerbaoui[1], N. El Bari[2], R. Ionescu[3], B. Bouchikhi[1,*]

1 Sensor Electronic & Instrumentation Group, Moulay Ismaïl University, Faculty of Sciences, Physics Department, B.P. 11201, Zitoune, Meknes, Morocco, benachir.bouchikhi@gmail.com
2 Biotechnology Agroalimentary and Biomedical Analysis Group, Moulay Ismaïl University, Faculty of Sciences, Biology Department, B.P. 11201, Zitoune, Meknes, Morocco
3 Electronics, Electrical and Automatic Eng. Department, Rovira i Virgili University, Tarragona Spain

## Abstract

The purpose of this study is to demonstrate that E-nose technology has the ability to accurately discriminate between different groups of Volatile Organic Compounds (VOCs) exhaled from Seasonal Allergic Rhinitis (SAR) breath, smoker and non-smoker healthy subjects. The database generated by the Electronic nose (E-nose) was treated by multivariable analysis techniques including: Principal Component Analysis (PCA) and Support Vector Machines (SVMs). In this work, we investigate the potential use of an E-nose system as an available non-invasive tool, low cost and rapid technique for breath gas analysis.

## 1. Introduction

The study of the exhaled VOCs and their connection to normal body functions and disease is an active field of research. Analyses of volatiles from patients offers the possibility of rapid diagnosis and also potentially permits the long term monitoring of the population, for early detection of organ impairment or other illness [1]. Breath collection is very patient friendly and analysis potentially offers a non-invasive method for assessing organic compounds in the exhaled breath [2]. E-nose technology was developed in the early 1980s in an attempt to replicate the mammalian olfactory system's ability to detect VOC's [3]. E-noses are easily portable, suited to near patient testing and have the potential to give a diagnosis of infection with minutes or hours as opposed to days with conventional means. Compared to the blood or urine tests, breath analysis is a particularly beneficial diagnostic method, due to its non-invasiveness for medical screening, real-time for metabolic status monitoring and partly due to the wide applicability for all patients and rapid detection without any limitation in supply [4].

On the other hand, there is recognized to be a clinically important relationship between upper and lower airways allergic inflammation [5]. However, the concentration of Carbon monoxide (CO) and Nitric Oxide (NO) are increased in patients with allergic rhinitis [6,7] this has given us an exceptional fingerprint. The breath of a healthy person gives a different pattern compared to a sick one, which can be detected by the electronic nose, without the use of expensive techniques to extract VOCs.

## 2. Materials and methods

Breath samples were obtained from 19 volunteers students (aged 19-32 years) of the Faculty of Sciences (Meknes, Morroco) either by exhaling directly into the chamber containing the sensors array or by collecting 1 liter of exhaled breath into Tedlar gas sample bags. In the initial experiments there was a consistent discrepancy between the two methods of sampling, such that direct exhalation into the chamber resulted in 2 to 2,5-fold greather conductance value of the sensors array caused by an increasing of the value of relative humidity. The use of such sample bags, which are specifically designed for the analysis of trace gases, was necessitated, in one hand by the difficulty of subjects visiting the laboratory, and in other hand by to stabilize the value of relative humidity during the measurements. The developed electronic nose comprised an array of chemical sensors commercially available (MQ2, MQ3, MQ9, MQ135, MQ137 and MQ138), a temperature sensor (LM35DZ) and a relative humidity sensor (Honeywell HIH 4000-002) were used for constantly monitoring the inner sensor chamber temperature and relative humidity. The signals of the sensor array were collected for 5 min of exposure to exhaled breath VOCs.

## 3. Results and discussions

The experiments have been performed for the determination of three different breath profiles. However, the characterization between SAR and healthy subjects was attempted. First, a plot of the $\Delta G/G_m$ (where $G_m$ is the measured conductance of the sensor and $\Delta G$ is the baseline of the sensor in the absence of analyte-corrected steady-state conductance change upon exposure the exhaled breath) when the sensor MQ9 is exposed to the

different types of breath samples is shown in Fig. 1. It can be seen that SAR breath response is evidently different to the healthy breath responses and moreover between smokers and non-smokers healthy subjects. The radar plot, used as a method to display data, is much recommended when it is associated with statistical analysis, which can often anticipate the classification of clusters. Radar plots were used in order to see if there are pattern differences (i.e. fingerprints) between breath samples from different subjects (Fig. 2) which shows a representative case. This fact was demonstrated statically by mathematical methods, such as PCA. PCA is a powerful linear unsupervised pattern recognition method that reduces the dimensionality of a multivariate problem and helps to visualize the different categories of breath profiles by highlighting similarities and differences between sample clusters. The results showed that the total variance of the first three principal components (PC1, PC2 and PC3) was achieved 99.59 % (Fig. 3). Based on PCA, three clusters according to healthy, smoker and SAR breath, are obviously distinguished. Similarities between breath samples of healthy and treated SAR subjects were easy identified. Furthermore, the database acquired from the sensors was treated also by SVMs method which designated a success rate of 96.49 % is attained in the recognition of the different subjects.

## 4. Conclusions

The obtained results demonstrate that the electronic nose system based on six MQ gas sensors coupled to multivariable analysis techniques is expected as an available analytical tool to discriminate the breath samples according to SAR patients, smokers and non-smokers healthy subjects. This study has confirmed the usefulness of an electronic nose as rapid, non-invasive and inexpensive tool for breath gas analysis.

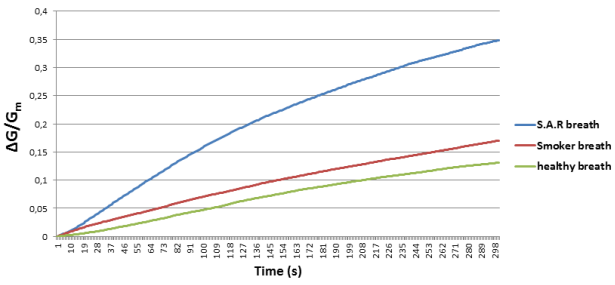


**Fig.1.** Time responses of $\Delta G/G_m$ of MQ9 gas sensor upon exposure to different human breath.

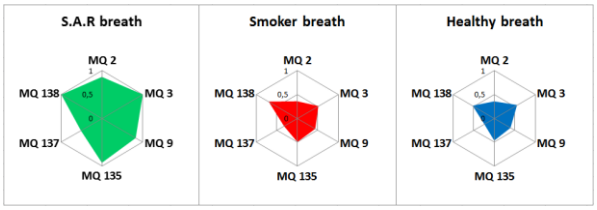


**Fig.2.** Radar plots of the gas sensor array for the breath samples of the 3 different breaths.

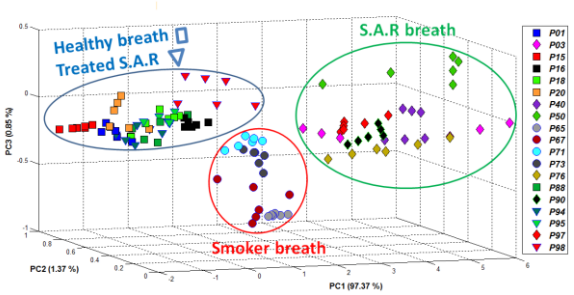


**Fig.3.** Three-dimensional PCA plot performed on Breath measurements of 19 subjects with data gathered using the electronic nose represented 99.59 % score plot.

## References


[1] W. Cao, Y. Duan, "Breath analysis: Potential for clinical diagnosis and exposure assessment", Clinical Chemistry 52:5, pp. 800–811, 2006.

[2] Z. Diamant, J.D. Boot, E. Mantzouranis, R. Flohr, P.J. Sterk, R.G.V. Wijk, "Biomarkers in asthma and allergic rhinitis", Pulmonary Pharmacology & Therapeutics 23, pp. 468-481, 2010.

[3] Persaud K, Dodd G. "Analysis of discrimination mechanisms in the mammalian olfactory system using a model nose", Nature 299, pp. 352–355, 1982.

[4] Y. Fang, J. Lahiri "Breath analysis: biomarkers, nanosensors, and mid-infrared absorption sensors", Chemical Sensors, pp. 3-9, 2013.

[5] A.M. Wilson, O.J Dempsey, E.J Sims, B.J Lipworth, "Subjective and objective markers of treatment response in patients with seasonal allergic rhinitis", Annals of Allergy, Asthma and Immunology, vol 85,pp. 111-114, Aug, 2000.

[6] M. Monma, M. Yamaya, K. Sekizawa, K. Ikeda, N. Suzuki, T. Kikuchi, T. Takasaka, H. Sasaki, "Increased carbon monoxide in exhaled air of patients with seasonal allergic rhinitis", Clinical and Experimental Allergy, Vol 29, pp. 1537–1541, 1999.

[7] J.F. Arnal, A. Didier, J. Rami, C. M'rini, J.P. Charlet, E. Serrano, J.P. Besombes, "Nasal nitric oxide is increased in allergic rhinitis", Clinical and Experimental Allergy, Vol 27, pp. 358-362, 1997.

# Enhancing the Quantification of Amino Acids by 1H-NMR Spectroscopy, Considering their Interaction with Human Serum Albumin

R. Barrilero[1,2,3*] and X. Correig[1,2,3]

1. Dept. d'Enginyeria Electrònica, Elèctrica i Automàtica, Metabolomics Platform, URV, Tarragona, Spain
2. Institut d'Investigació Sanitària Pere Virgili (IISPV), Reus, Spain
3. Centro de Investigación Biomédica en Red de Diabetes y Enfermedades Metabólicas Asociadas (CIBERDEM), Madrid, Spain

*Corresponding to: ruben.barrilero@urv.cat

## Abstract

High-throughput 1H-NMR of serum is extensively used in large-scaled clinical trials, this method does not require sample separation, however, binding interactions between low molecular weight metabolites (LMWMs) and large macromolecules produce some LMWM signals to become partially or totally "invisible" in NMR spectra. In this study, we present novel strategies to release the "invisible" part of these LMWMs and achieve more accurate quantifications based on competitive binding and multivariate curve resolution methods. The study is focused mainly in five amino acids of clinical relevance.

## 1. Introduction

Amino acids (AAs) and other low molecular weight metabolites (LMWMs) in blood have been found to play an important role in the early stages of several metabolic-related diseases such as type 2 diabetes and cardiovascular events [1,2]. High-throughput 1H-NMR of serum has been established as the main method for the profiling and quantification of LMWMs in large population studies, as it requires only minimal sample handling and the inherent reproducibility of NMR. However, because no separation step is applied in high-throughput NMR, some LMWMs bind to macromolecules, especially to the most abundant protein human serum albumin (HSA), and the motional properties of LMWMs are severely affected. Consequently, their signals in 1H-NMR spectra are broadened and sometimes impossible to discern from background signals, making them "invisible" [3,4]. Since the degree of interaction depends on the presence of other competitors in HSA, especially endogenous free fatty acids (FFAs) [5], and their amount varies between individuals and clinical conditions [6], a reliable quantification of LMWMs could be hampered by such variability, masking biological variability. Moreover, the background reduction technique based on "T2-filtered" one-dimensional CPMG sequence could introduce further variability in the quantification, as it suppresses part of the signal regardless of the sample-dependent relaxation properties. The purpose of this study is to offer strategies to avoid such variability and improve the quantification of LMWMs interacting with HSA. The experimental work is mainly focused on five AAs (with a priori different binding affinity with HSA) as they are known to be clinically-relevant in metabolic diseases.

## 2. Materials and methods

In order to characterize the binding response of the AAs of clinical interest (L-Phenylalanine, L-Valine, L-Isoleucine, L-Leucine, L-Tyrosine) to HSA, a series of standard additions of these AAs into non-fatted HSA solution were prepared fixing HSA (0.3 mM) and concentration ratios of AAs-HSA ranging from 0.25 to 500. The response was plot as the measured quantity versus the added quantity. The analysis of the release of binding LMWMs was performed in two steps. In the first step, we prepared a serum mimic which consists in a mixture between a set of LMWMs (those mostly found in common 1H-NMR spectra of serum) and non-fatted HSA. We used concentrations reported in serum of healthy people. We promoted the complete release of these LMWMs from HSA using the addition of an exogenous compound (not found in serum) that competes with them for binding to HSA, whilst having no interfering signals in a 1H-NMR spectrum. We performed a standard addition of TMSP-d4 (which was previously reported to bind to HSA) ranging from 0.3 mM to 12 mM and evaluate the amount needed for the maximum release. In the second step, we measured the effect of adding the previously calibrated amount of TMSP-d4 in real serum from one healthy volunteer. We used the calibration curves based on standard additions as a method to obtain the real (total in serum) and the measurable (not bound fraction) concentration of the five aforementioned AAs. We used additions ranging from 0.5 times the normal concentration reported in the HMDB to 4 times in four steps, plus one point without AAs addition. The capacity of TMSP-d4 to release was tested comparing calibration curves with and without TMSP-d4. In order to evaluate the error in the

calculation of the curves and test statistical results, we replicate three times the minimum (no addition) and the maximum point (4x).

All the samples were measured in a Bruker Avance III 500 spectrometer using CPMG-presat experiment with T2-filters ranging from 0 to 2.5 s in 10 steps. Multivariate Curve Resolution-Alternating Least Squared (MCR-ALS) was used as a method to extract individual spectral and decay components (transversal relaxation T2) in overlapped regions. This technique allows the calculation of measurable concentrations of LMWMs corrected by their sample-dependent T2.

## 3. Results

The binding response of the five AAs showed a sigmoidal curve with saturation of the complex AA-HSA for larger quantities than those typically found in serum (>10 times). All the metabolites showed a free-bound equilibrium state in a large margin containing serum concentrations. The five AAs presented different levels of binding interactions, with bound and therefore not measurable fractions ranging from nearly 70% (phenylalanine) to less than 10% (valine) of the total added.

Serum mimic was used to explore binding relationships in a more real, but still controllable, situation. LMWMs were further classified by their degree of binding interaction with HSA. When no TMSP-d4 was added, some metabolites were strongly bound (citrate, tryptophan, lactate, 3-hydroxybutyrate, phenylalanine, tyrosine). For these LMWMs, less than 60% of the original concentration could be measured. Other LMWMs showed not binding properties (glucose, valine) and approximately 100% of the original concentration was measured. The complete release of most of the partly bound LMWMs in the mimic was fulfilled after the addition of 5 mM of TMSP-d4. Nevertheless, citrate and tryptophan were not further release after adding TMSP-d4 at any point, revealing different mechanisms of these LMWMs-HSA complexes not shared with TMSP-d4 and the rest of the released metabolites. Transversal relaxations (T2) given as MCR decay components were also monitored in the addition of TMSP-d4. Even though the complete release of LMWMs was achieved, the T2 were still increasing towards T2 values found in aqueous solution. Whereas the "invisible" part may be explained by slow-exchange interactions, this change is explained as the modification in the fast-exchange equilibrium in the LMWMs-HSA complex. This remaining variability in fast-exchange could introduce some errors in a standard 1D CPMG, which is solved with 2D CPMG and MCR approaches.

The calibrated amount of TMSP-d4 in mimic sample was proof in a real serum sample. In order to test its capacity to release the bound LMWMs, we compared the ratio of free metabolite of LMWMs with and without 5 mM of TMSP-d4. Unlike the previous experiments, in real sample we did not know the "prior" concentration, i.e. the real concentration. In calibration curves based on standard additions it is where the curve crosses the x-axis, whereas the ratio of free metabolite is the slope of the curve. At first glance, comparison between spectra with and without TMSP-d4 shows a qualitative improvement of the resolution of metabolites found to bind to HSA in the mimic sample (phenylalanine, lactate, leucine and 3-hydroxybutyrate). Calibration curves revealed an increment in the free leucine (86% to 97%) and phenylalanine (35% to 75%) for $p<0.05$. Isoleucine and valine showed no change as they are mostly free. Surprisingly, tyrosine (completely released in the serum mimic) was not further release in serum by TMSP-d4 and the free fraction was calculated as 58%. This fact may be explained by the effect of other proteins or peptides present in serum having different binding properties than HSA.

## 4. Conclusions

In this study, we demonstrate the problems in serum quantification of LMWMs due to their interaction with large macromolecules. We present two novel strategies to solve them. The first one is based on chemical interactions and uses a binding competitor that promotes the release of the bound part of LMWMs, which is spectrally "invisible" due to slow-exchange interactions. The second one is based in curve resolution and consists in using 2D CPMG (instead of traditional 1D CPMG) and MCR-ALS in order to correct by T2 variability of fast-exchange interactions. They have found to improve the resolution and uncover up to 40% of some clinically-relevant AAs. However, the total bound of some metabolites was not released, suggesting more complex binding mechanisms, other proteins than HSA affecting LMWMs visibility or the need of other competitors with complementary binding properties. Moreover, further studies are needed in order to evaluate the clinical impact of applying these strategies in High-throughput 1H-NMR.

**References**


[1] Wurtz, P., A. S. Havulinna, P. Soininen, et al., "Metabolite profiling and cardiovascular event risk: a prospective study of 3 population-based cohorts", *Circulation*, 131, 774-85 (2015)

[2] Wang, T. J., M. G. Larson, R. S. Vasan, et al., "Metabolite profiles and the risk of developing diabetes", *Nature Medicine*, 17, 448-453 (2011)

[3] Nicholson, J. K., K. P. Gartland, "1H NMR studies on protein binding of histidine, tyrosine and phenylalanine in blood plasma", *NMR in Biomedicine*, 2, 77-82 (1989)

[4] Bell JD, Brown JC, Kubal G, et al, "NMR-invisible lactate in blood plasma", *FEBS Lett, 235 1-2, 81-86 (1988)*

[5] Jupin, M., P. J. Michiels, F. C. Girard, M. Spraul, S. S. Wijmenga, "NMR metabolomics profiling of blood plasma mimics shows that medium- and long-chain fatty acids differently release metabolites from human serum albumin", *J Magn Reson* 239, 34-43 (2014)

[6] Cistola, D. P., D. M. Small, "Fatty acid distribution in systems modeling the normal and diabetic human circulation. A 13C nuclear magnetic resonance study", *The Journal of Clinical Investigation*, 87, 1431-1441 (1991)

# Title: AuNP/Casein conjugates for application in the design of an electrochemical biosensor for pathogen leishmania detection and canine leishmaniasis diagnostics

Mohamed fethi Diouani*, Kamel Belgacem, Sabra Chargui, Maher Sayhi, Oussama Ouerguhi, Chaker Tlili, Radu Ionescu, Dhafer Laouini

*Laboratory of Epidemiology and Veterinary Microbiology, Pasteur Institute of Tunis, Tunis, Tunisia

Tel:+216 71783022 poste 551/550 Fax: +216 71791833 Email: fethi.diouani@gmail.com

## Abstract

Leishmaniasis is globally important zoonotic infection, affects animals and human beings, unfortunately a neglected disease. Recent developments in new diagnostic tools have opened new avenues for a vast improvement in parasite and *Leishmania* detection. Gold nanoparticles (AuNPs) due to their good biocompatibility with peptides and proteins and their electro-catalytic propriety can be easily loaded with casein micelles, driven toward *Leishmania* surface and electrochemically detected by chrono-amperometric method. AuNPs/casein complex leishmania interaction can be inhibited by leishmaniasis seropositives dogs serum with a good correlation between chronoamperometric response and Immunofluorescence Test response Titer.

## 1. Introduction

Leishmaniasis, a complex vector-borne disease caused by obligate intra-macrophage protozoa, affects animals and human beings. The disease is endemic in 88 countries of 5 continents with a total of 350 million people at risk and 12 million cases. A total of about 21 *Leishmania* (*L.*) species have been identified to be pathogenic to human and cause mainly three clinical forms of leishmaniases. The visceral leishmaniasis (VL) is caused mainly by species of *L. donovani* complex, the Mucocutaneous leishmaniasis (MCL) is caused mainly by *L.* (*viannia*) *braziliensis* and *L.* (*viannia*) *guyanensis* and cutaneous leishmaniasis (CL) where causative species are *L. major*, *L. tropica*, *L. mexicana* and *L. amazonensis* [6]. The *Leishmania* parasites are digenetic trypanosomatids that cycle between the gut of the sand fly vector (promastigote forms) and the phagolysosome of a mammalian host macrophage (amastigote forms).

Several *Leishmania* surface molecules facilitate survival in these diverse host environments. Both amastigote and promastigote forms of Leishmania spp. express a major glycosyl-phosphatidylinositol (GPI)-anchored glycoprotein of 63 kDa named gp63 or leishmanolysin. It is a $Zn^{2+}$ dependent HEXXH metallopeptidase, with a broad range of substrate specificity and an optimum pH activity [2]. It is an enzyme capable of degrading many protein substrates including casein, azocasein, gelatin, albumin, hemoglobin, and fibrinogen [5]. This glycoprotein is one of the molecules involved in the infectivity of *Leishmania* and in parasite uptake by macrophage receptors in mammalian cells [1].

Leishmaniasis still remains a parasitic disease of major importance that no vaccine is available against it. Currently, the detection and diagnosis of *Leishmania* infections rely on mostly laboratory methods in addition to clinical symptoms, clinical history, travel history, and geographic location of the patient.

Recent developments in new diagnostic tools have opened new avenues for a vast improvement in parasite and *Leishmania* detection [4]. Nano materials particularly Gold nanoparticles (AuNPs) due to their good biocompatibility with peptides and proteins and their electro-catalytic propriety, play an important role in current sensing and bio-sensing technologies. Their use as carriers of biomolecules and their application in biomedical and nutritional technologies, between others, is an emerging research field.

## 2. Objectives

Design and optimization of a chronoamperometric biosensor, using AuNPs/casein complex, for Leishmania parasite detection and canine leishmaniasis sero-diagnostic**.**

## 3. Methodology

In this work, AuNps and AuNPs/casein conjugates were first synthesized as described by Espinoza-Castañeda and col [3] then characterized by Scanning Electron Microscope (SEM) and Ultraviolet–visible spectroscopy (Fig.1) and used for the design of an electrochemical biosensor for *Leishmania* parasite detection and canine leishmaniasis sero-diagnostic. This, using a simple and rapid way through the chronoamperometric monitoring, at a fixed potential (-1V), of the hydrogen evolution reaction on screen-printed carbon electrodes [3].

## 4. Results

Obtained results show that synthetized gold nanoparticles have a size of 13.55 +/- 1.1 nm and can be easily loaded with casein micelles, driven toward *Leishmania* surface and electrochemically detected by chrono-amperometric method (Fig.2). The results indicate that *Leishmania* parasites can be quantitatively detected with a limit less than 1 parasite/ml. Results also show that *Leishmania* casein interaction is inhibited by a leishmaniasis seropositive canine serum with a good correlation between the chronoamperometric response and immune-fluorescence serum titer (Fig.3).

## 5. Figures

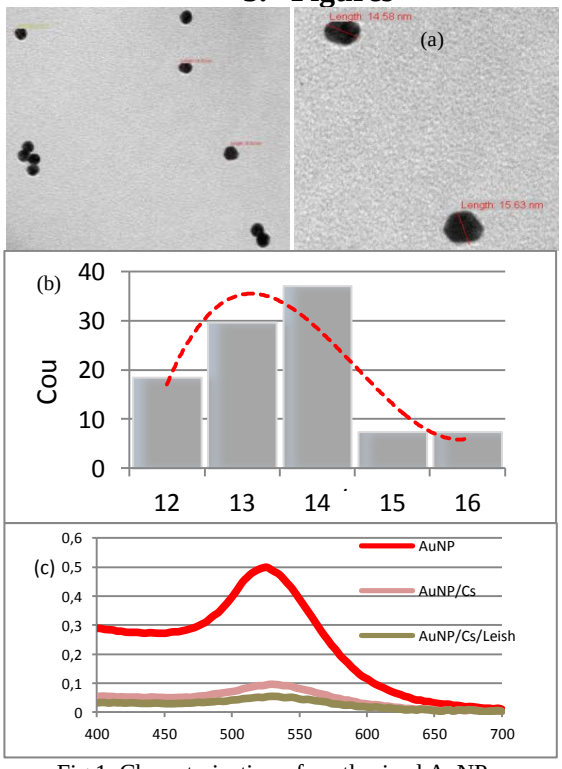


Fig.1. Characterization of synthesized AuNPs: (a)SEM images (b) size distribution, (c) UV Vis curves for AuNPs, AuNPs/Casein conjugate and AuNPs/Cs/ *Leishmania*.

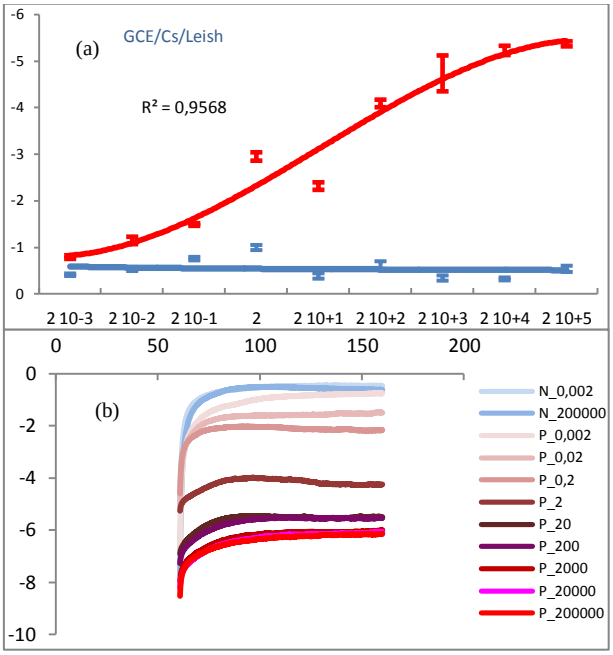


Fig.2. (a) Calibration curve, selectivity and the detection limit of the developed biosensor. (b)Electrochemical detection of Leishmania based on the electrocatalytic detection of AuNP labeled casein performed in 1M HCl by chronoamperometry.

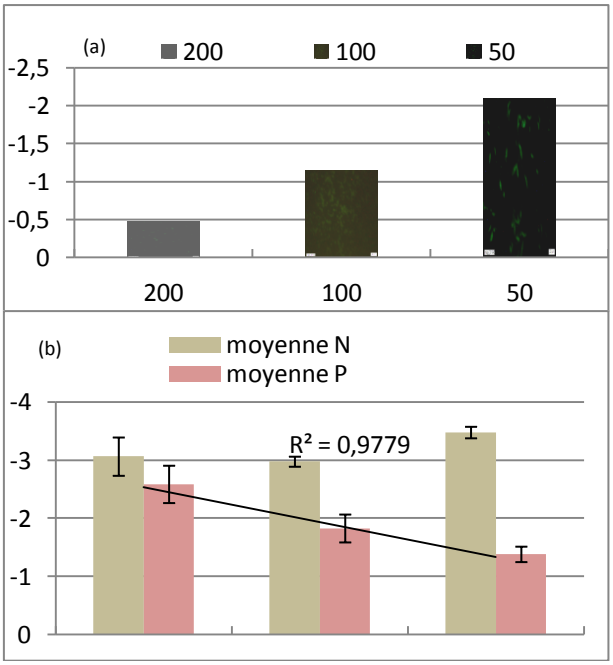


Fig.3 Inhibition with different serum dilutions according to the results obtained by the IFI test. (a)-inhibition with different antibody dilution.(b) Chronoamperometic response difference recorded for seronegative and seropositive serums for each dilution.

## 6. Conclusion

Obtained results show that gold nanoparticles can be easily loaded with casein micelles, driven toward *Leishmania* surface and electrochemically detected by chrono-amperometric method. The results indicate that *Leishmania* parasites can be quantitatively detected with a limit less than 1 parasite/ml. The *Leishmania* casein interaction is inhibited by a leishmaniasis seropositive canine serum with a good correlation between the chronoamperometric response and immune-fluorescence serum titer**.**

## References


[1] Ali Akbar Shaebani, Robert W. McMaster, Delavar Shahbazzadeh, Mohsen Karimi and Fereidoun Mahboudi. Expression of Gp63 Gene from NIH Strain of Leishmania major in Pichia pastoris. Iranian Biomedical Journal, 2001, 5, 39-45.

[2] Elias CG, Pereira FM, Silva BA, Alviano CS, Soares RM, Santos A L. Leishmanolysin (gp63 metallopeptidase)like activity ext racellularly released by Herpetomonas samuelpessoai. Parasitology, 2006, 132, 37-47.

[3] Espinoza-Castañeda M, de la Escosura-Muñiz A, González-Ortiz G, Martín-Orúe SM, Pérez JF, Merkoçi A. Casein modified gold nanoparticles for future theranosti c applications. Biosens Bioelectron, 2013, 40, 271-6.

[4] Ndao M. Diagnosis of parasitic diseases: old and new approaches. Interdiscip Perspect Infect Dis. 2009, 2009, 278246.

[5] Yao C, Donelson JE, Wilson ME. The major surface protease (MSP or GP63) of Leishmania sp. Biosynthesis, regulation ofexpression, and function. Mol Biochem Parasitol. 2003, 132, 1-16

[6] Singh S. New developments in diagnosis of leishmaniasis. Indian J Med Res. 2006, 123, 311-30.

# Characterizing geometries of nanoporous alumina membranes and sensing by means of laser refractometric interference spectroscopy

Chris Eckstein, Josep Ferré-Borrull, Lluis F. Marsal

Departament d'Enginyeria Electrònica, Elèctrica i Automàtica, Universitat, Rovira i Virgili, Avda. Països Catalans 26, Tarragona 43007, Spain. Contact via chris.eckstein@urv.cat or +34601625951

## Abstract

The functionalization of nanoporous structures is common practice and found in various sensing devices. Monitoring the rate of capillary driven fluid imbibition, laser refractometric interference spectroscopy (laser-RIfS) can be applied as a novel nano-characterization and sensing technique. In this study nanoporous anodic alumina membranes (NAA) with pore diameters ranging from 30-56nm were functionalized with layer by layer deposition (LbL) of poly(allylamine hydrochloride) (PAH) and poly(sodium 4-styrenesulfonate) (PSS) to study the sensitivity of laser-RIfS. Minor reductions in pore diameters down to 1-1.5nm were detected. In a second experiment imbibition rate reductions due to immobilized BSA and specific immunoglobulin binding were detect. Our results experimentally demonstrate the sensitivity and applicability of laser-RIfS as a sensing device.

## Introduction

The inner walls of nanoporous structures are frequently functionalized to detect and characterize biomolecules [1],to monitor enzyme kinetics in real-time [2] and to develop tunable and stimuli responsive nano-systems [3], to name but a few examples.

Laser-RIfS employs a single wavelength to monitor light intensity fluctuations upon capillary driven fluid imbibition in nanoporous membranes in real-time [4]. By changing the optical path, the moving liquid interface produces distinct light intensity oscillations due to phase shift overlays or cancellations which give rise about the internal geometry of nano-capillaries.

In this study we experimentally determined the sensitivity and applicability of laser-RIfS as a novel optofluidic sensing device. We were able to detect differences in pore radii of non-functionalized and functionalized nanoporous anodized alumina membranes (NAA). Layer by layer deposition of polyelectrolytes was used to assess the sensitivity of the method by gradually reducing the pore diameters. The detection of bovine serum albumin (BSA) and anti-BSA immunoglobulins validated laser-RIfS as a potential sensing device.

## Materials & Methods

### *Sample fabrication (in brief)*

A two-step anodization protocol in 0.3M oxalic acid, at 40V and 3-5°C was used until pore lengths of about 65-90µm were reached. Remainder aluminum was removed by a mixture of $CuCl_2$-HCl (saturated) and 68% $HNO_3$. Pores were opened with 5% $H_3PO_4$ or reactive ion etching. NAA were functionalized by dipping in BSA, anti-BSA, PAH, PSS solutions for 30min. Pore diameters were extracted by ESEM image analysis.

### *Laser-RIfS*

Light intensities of a laser beam reflected off of the open bottom side of an NAA are measured. A solvent dropped onto the top side of an NAA is readily drawn into the pores by capillary forces.

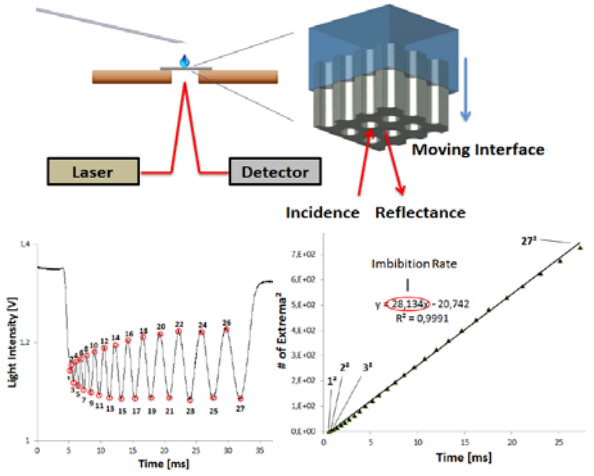


**Figure 1:** Data acquisition and extraction flow chart: Drop released on NAA, oscillations recorded in real-time, squared peak numbers plotted against time, slopes of linear regression used for comparison.

The solvent's moving interface causes oscillating light interferences which are detected in real-time with sub-millisecond resolution. The oscillations are numbered with integers and plotted as the squared peak number against time of occurrence. The slopes of the linear regression represent imbibition rates and provide the basis for comparison of solvents and pore geometries.

## Results and Discussion

Parameters such as volume, release height and impinging location of the solvent and the NAA pore length do not affect fluid imbibition rates (data not shown). However, variations in pore diameters significantly affect the rate at which the solvents travel through the membrane (figure 2). The up to 10 fold increase in imbibition rates, due to increasing pore diameters, and the differences between solvents, due to their differences in surface tensions, are in line with the classical Lucas-Washburn equation.

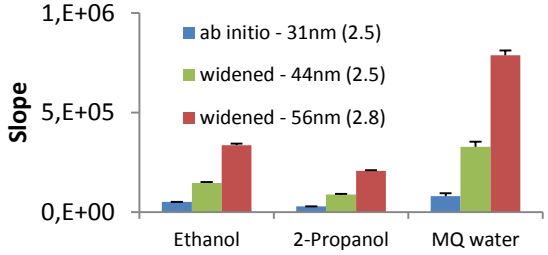


**Figure 2**: Fluid imbibition rates represented by slopes for three different solvents and pore diameters. Whiskers and parentheses depict standard deviations of 5 replicates.

Reduction in pore diameters due to LbL deposition of polyelectrolytes (figure 3) are reasonably approximated to 1-1.4nm for every added layer [5]. The three solvents decelerate with every additional layer, in 30 and 56nm pores. However, imbibition rate reductions are more prominent in larger pores.

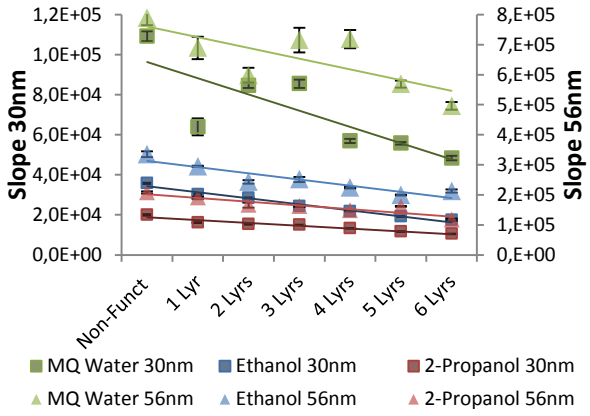


**Figure 3:** LbL deposition of polyelectrolytes in NAA. Slopes and standard deviations of 5 replicates are presented.

Fluorescence confocal microscopy validated the homogenous immobilization of BSA in NAA throughout the membrane (data not shown). The pore radius reduction due to BSA immobilization and subsequent antibody labelling was detected by laser-RIfS for four solvents (figure 4).

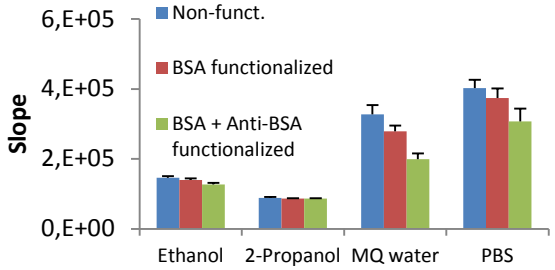


**Figure 4**: Effects of BSA immobilization and antibody binding in 44nm NAA on the imbibition rates of 4 solvents. Standard deviations of 5 replicates are presented.

The reductions in imbibition rate of 2-propanol is somewhat low, considering an estimated total diameter reduction due to BSA and antibody immobilization of about 6-12nm (Sigma Aldrich production information CAS number: 9048-46-8). Electrostatic interactions of charged protein moieties with the solvents are likely to affect the liquid-solid contact angle inside the pores thereby changing the solvents' menisci, in turn affecting the movement of the liquid interfaces.

## Conclusion

This study presents an empirical approach to exploit effects of surface modifications in NAA on capillary filling dynamics and provides cohesive evidence for the applicability of laser-RIfS monitored capillary filling as a sensitive and reproducible characterization and sensing device. Minor changes in pore radii down to the single nanometer range were successfully monitored and specific antibody – antigen binding could be detected.

### References


[1] M. Baranowska, A. J. Slota, P. J. Eravuchira, G. Macias, E. Xifré-Pérez, J. Pallares, J. Ferré-Borrull, and L. F. Marsal, "Protein attachment to nanoporous anodic alumina for biotechnological applications: influence of pore size, protein size and functionalization path.," *Colloids Surf. B. Biointerfaces*, vol. 122, pp. 375–83, Oct. 2014.

[2] a Dhathathreyan, "Real-time monitoring of invertase activity immobilized in nanoporous aluminum oxide.," *J. Phys. Chem. B*, vol. 115, no. 20, pp. 6678–82, May 2011.

[3] W. Guo, H. Xia, F. Xia, X. Hou, L. Cao, L. Wang, J. Xue, G. Zhang, Y. Song, D. Zhu, Y. Wang, and L. Jiang, "Current rectification in temperature-responsive single nanopores," *ChemPhysChem*, vol. 11, no. 4, pp. 859–864, 2010.

[4] L. N. Acquaroli, R. Urteaga, C. L. a Berli, and R. R. Koropecki, "Capillary filling in nanostructured porous silicon.," *Langmuir*, vol. 27, no. 5, pp. 2067–72, Mar. 2011.

[5] M. Elzbieciak, M. Kolasinska, and P. Warszynski, "Characteristics of polyelectrolyte multilayers: The effect of polyion charge on thickness and wetting properties," *Colloids Surfaces A Physicochem. Eng. Asp.*, vol. 321, no. 1–3, pp. 258–261, 2008.

# Combining Perovskite Based Photovoltaic Devices with Lead Sulfide Quantum Dots

Ilario Gelmetti*, Emilio Palomares

Institute of Chemical Research of Catalonia (ICIQ)
* igelmetti@iciq.es

## Abstract

In these few months since the beginning of my PhD I prepared perovskite ($CH_3NH_3PbI_3$) based photovoltaic devices and lead sulfide (PbS) quantum dots, then I started making photovoltaic devices which contains both materials.

## 1. Introduction

Research in solar cells was perturbed in 2009 by the appearance of a promising-yet-strange material: a hybrid organic-inorganic lead halide-based compound called hybrid perovskite from its structure perovskite-like. This material shows a whole bunch of features that are unusual for the photovoltaic materials we are used to, the understanding of these behaviors is challenging and thrilling the research community. The easiness of preparation, cheapness and the high reached efficiency indicate this material as promising for wide-scale application.

The problems to be solved are various, not only regarding the perovskite material itself, for example the cost of the cell is heavily influenced by the cost of the organic molecule used as hole transporting material (usually spiro-MeOTAD). Replacing this organic layer with a cheaper option is highly desiderable.

Lead sulfide quantum dots is a very versatile semiconductor with tunable electronic levels depending on the diameter. Moreover it shows some absorption in the infrared sunlight region, where the perovskite material doesn't absorb.

## 2. Perovskite Based Solar Cells

I produced various sets of perovskite based solar cells bearing spiro-MeOTAD as hole transporting material following the procedure optimized in our group[1]. An optimization of annealing process was also performed. The structure of these cells is schematized in fig. 1a.

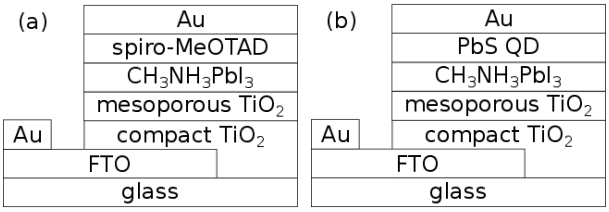


**Fig.1.** perovskite cell structure (a) with spiro-MeOTAD, (b) with PbS quantum dots.

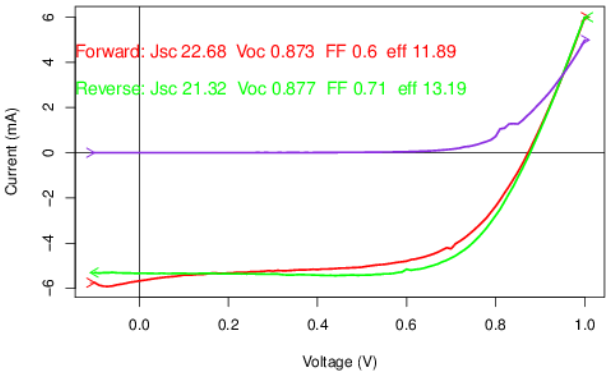


**Fig.2.** The IV curve characterization of a perovskite-spiroMeOTAD cell with an active surface of 0.25 $cm^2$.

Two similar types of substrate were used: 15x15 mm and 25x25 mm implying slightly different substrate preparation, solutions quantities and holders for measurements. In fig. 2 an example of IV curve characterization under 1 sun illumination is reported. In fig. 3 an example of external quantum efficiency spectrum for a perovskite cell is reported, as can be seen this material can collect charges absorbing light from a huge part of the solar spectra region but there are some problems in the near infrared region, this could be due to poor absorption but also to recombination processes. An option for mitigating this problem is to add another photoactive layer which can work also in near infrared region of solar spectra. That's why we thought at the lead sulfide quantum dots.

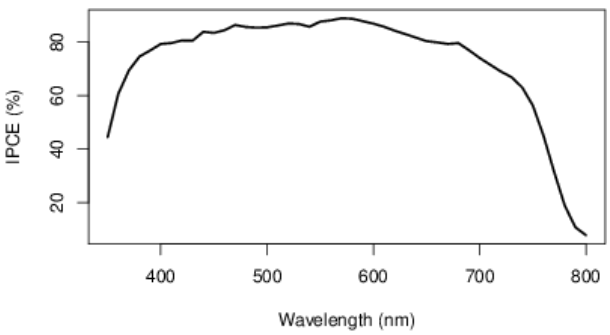


**Fig.3.** The extrernal quantum efficiency characterization of a perovskite-spiroMeOTAD cell with an active surface of 0.25 $cm^2$.

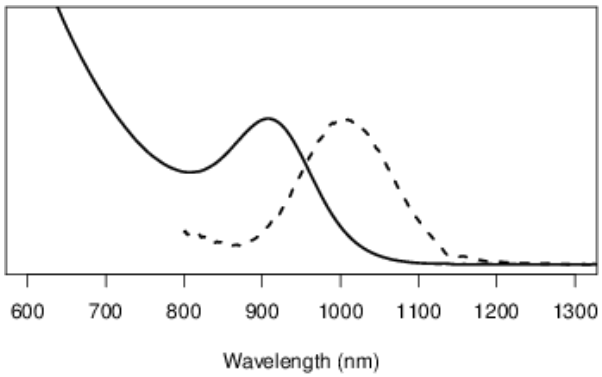


**Fig.4.** Normalized absorbance (continuous line) and photoluminescence (dashed line) of PbS QD in toluene.

## 3. Use of PbS Quantum Dots

The PbS quantum dots were synthesized via a hot injection route[2] resulting with a diameter of 3 nm (estimated by absorbance peak[3] and confirmed by TEM, crystallographic structure confirmed by XRD). Absorbance and photoluminescence of QD solutions are reported in fig. 4.

The quantum dots were successfully absorbed on a mesoporous titania layer and a layer of perovskite was deposited on top of that. The resulting device has also spiro-MeOTAD on the other side. The performance of such a cell was very bad, likely because the electronic levels of PbS QD are not adapt to take electrons from perovskite.

Then I tried to use PbS as a hole transporting material, spin coating a layer of quantum dots on top of annealed perovskite. This study is in progress in these days.

**References**

[1] J. M. Marin-Beloqui, J. P. Hernandez, and E. Palomares, “Photo-induced charge recombination kinetics in MAPbI3-xClx perovskite-like solar cells using low band-gap polymers as hole conductors.,” *Chem. Commun. (Cambridge, United Kingdom)*, vol. 50, no. 93, pp. 14566–14569, 2014.

[2] J. W. Ryan, J. M. Marin-Beloqui, J. Albero, and E. Palomares, “Nongeminate recombination dynamics-device voltage relationship in hybrid PbS quantum dot/C60 solar cells.,” *J. Phys. Chem. C*, vol. 117, no. 34, pp. 17470–17476, 2013.

[3] J. Zhang, J. Gao, E. M. Miller, J. M. Luther, and M. C. Beard, “Diffusion-controlled synthesis of PbS and PbSe quantum dots with in situ halide passivation for quantum dot solar cells.,” *ACS Nano*, vol. 8, no. 1, pp. 614–22, Jan. 2014.

# Wavelet-Based Calculation of the Transmission Coefficient for Tunneling Events in Tunnel-FETs

Atieh Farokhnejad[1], Michael Graef[1 2] * and Alexander Kloes[1]
[1] Competence Centre for Nanotechnology and Photonics, Technische Hochschule Mittelhessen, Giessen, Germany
[2] DEEEA, University Rovira i Virgili, Tarragona, Spain
*michael.graef@ei.thm.de

In the last few years, the Tunnel-FET has become one of the most promising candidates to be the successor of the standard MOSFET, due to the advantages of its alternative current transport mechanism, the B2B tunneling. It allows the Tunnel-FET to fall below the 60 mV/dec subthreshold slope (S) limitation of the thermionic-emission-based current transport mechanism of the MOSFET, although these small slopes are quickly degrading for an increasing ON-state current. The reasons of this degradation are fabrication-related negative effects i.e. doping profiles, trap-assisted-tunneling (TAT) and gate leakage currents. There are three different tunneling events happening simultaneously in the Tunnel-FET: The desired band-to-band (B2B) tunneling and the unwanted TAT and gate leakage effects, whereby for every different tunneling event the barrier shape, tunneling distances and relevant energy levels are changing. This clearly shows the need for a flexible tunneling model in order to calculate these probabilities accurately.

The wavelet method has been applied before to determine the tunneling coefficient for triangular barriers in MIM junctions. In the paper an overview to this wavelet-based calculation of the transmission coefficient is explained and verified. A comparison of the wavelet solution with the solution of the Schrödinger equation for rectangular barriers and the WKB approximation for triangular shaped barriers is achieved. Furthermore, this method is used to calculate the transmission coefficient for TAT in Tunnel-FETs.

### *Tunnel-FET Barriers Shapes*

Within the n-Tunnel-FET different types of tunneling events occur, depending on the actual state of the Tunnel-FET. Therefore, in the ON-state of the device a B2B tunneling prevails, whereby in the OFF-state the TAT overwhelms. Depending on the tunneling type, different shapes of barriers have to be considered. Figure 1 schematically illustrates the different barrier shapes for the TAT and B2B tunneling events. TAT is considered to always start directly at the junction of the device, where the traps are localized. The B2B tunneling happens from the valence band of the source region to the conduction band of the channel region. The quasi 2D WKB approach is used to calculate the reference data, whereby the transmission coefficient is overestimated, due to the smaller barrier height.

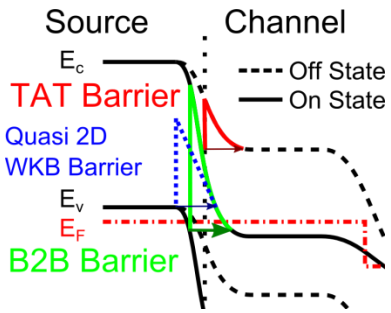


Figure 1. Band structure of a n-Tunnel-FET in ON- and OFF-state, illustrating the barrier shapes used for the wavelet solution. The reference transmission coefficients are calculated using quasi 2D WKB barriers.

### *Wavelet Solution for Trap-Assisted-Tunneling*

The TAT probability is compared to a quasi 2D WKB approach. The starting point is located the source/channel junction of the device. The results illustrated in figure 2 show the TAT probability to the conduction band of the channel region of a n-Tunnel-FET in OFF-state (see Fig. 1)

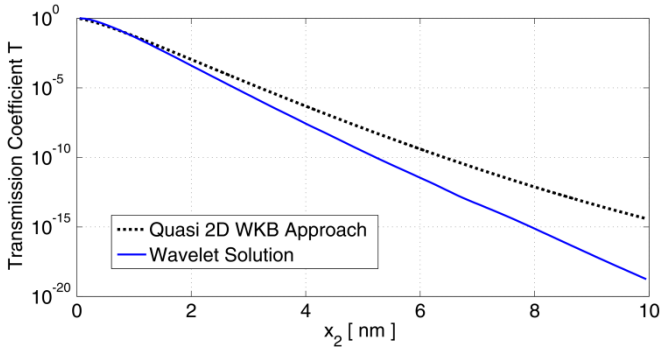


Figure 2. Wavelet-based calculation of the transmission coefficient for TAT in the OFF-state of a n-Tunnel-FET in comparison to a quasi 2D WKB solution.

The overestimation of the quasi 2D WKB approach is clearly seen for an increasing tunneling distance. Therefore, the wavelet solution is an improved method regarding the tunneling probability calculation for different shaped barriers.

# Continuous Charge-Based Current Model for Organic TFT Derived From Gaussian DOS

F. Hain[1,2], C. Lammers[1], F. Horst[1], F. Hosenfeld[1,2], B. Iniguez[2], A. Kloes[1]
[1]TH Mittelhessen, Germany, [2]URV, Spain
franziska.hain@ei.thm.de

Most modeling approaches for organic field-effect transistors (OFETs) are based on the threshold voltage as fitting parameter without relation to physical parameters. In this paper the presented current model is charge based with a continuous equation valid in all regions of operation. For solving Poisson's equation the model takes into account a Gaussian density of states (DOS) Γ(E) for charge $Q'_m$ in shallow traps (Fig. 1) contributing to the device current by hopping transport, and charges $Q'_t$ in deep bulk and interface states with density $N'_t$ independent from energy [1]:

$$V_{gs} = V_{fb} + \phi_c + \frac{1}{C'_{ox}}\left(Q'_m + Q'_t\right) \qquad Q'_m = qd_m\int_{E_\mu}^{\infty}\Gamma(E)\,f(E)\,dE \qquad Q'_t = q(N'_t q\phi_c + N'_{t0})$$

with Fermi function f(E), channel thickness $d_m$ and channel potential $\Phi_c$. We derive the differential:

$$\frac{\partial V_{gs}}{\partial \phi_c} = 1 + \frac{1}{C'_{ox}}\left[\frac{\partial Q'_m}{\partial \phi_c} + \frac{\partial Q'_t}{\partial \phi_c}\right] = 1 + \frac{Q'_m}{C'_{ox}kT/q} + \frac{q^2 N'_t}{C'_{ox}} = \alpha + \frac{Q'_m}{C'_{ox}kT/q}.$$

In subthreshold operation the bias dependent filling of $N'_t$ influences the electrostatics, and hence limits the accumulated charge. The degradation of the subthreshold slope depends on parameter α (ideal slope for α = 1). From the differential the accumulated charges $Q'_{ms/d}$ at the source and drain end of the channel have been deduced by integration in an analytical closed form similarly to [2]:

$$\frac{\partial Q'_m}{\partial V_{gs}} = \left[\frac{\alpha kT}{qQ'_m} + \frac{1}{C'_{ox}}\right]^{-1} \Rightarrow Q'_{ms/d} = \frac{\alpha kT}{q}C'_{ox}\,LambertW\left\{\frac{Q'_{m0}}{C'_{ox}\alpha kT/q}\exp\left(\frac{C'_{ox}(V_g - V_{s/d} - V_0) + Q'_{m0}}{C'_{ox}\alpha kT/q}\right)\right\}.$$

Parameter $Q'_{m0}$ is the charge in shallow traps at gate voltage $V_0$. The effect of hopping transport can be described by a proper mobility model [3], which allows formulating the current equation in terms of drift-diffusion transport of quasi-free carriers:

$$I_{ds} = \mu W\left[\frac{kT}{q}\cdot\frac{Q'_{ms} - Q'_{md}}{L} + \frac{Q'^{\,2}_{ms} - Q'^{\,2}_{md}}{2LC'_{ox}}\right].$$

The model has been successfully implemented in Verilog-A by adding parasitic contact resistances in a macro model. The results are in good agreement to measurements on OFETs [4] (Fig. 2).

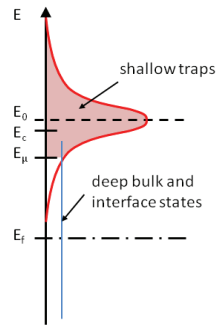


Fig. 1: Gaussian DOS, deep bulk and interface states.

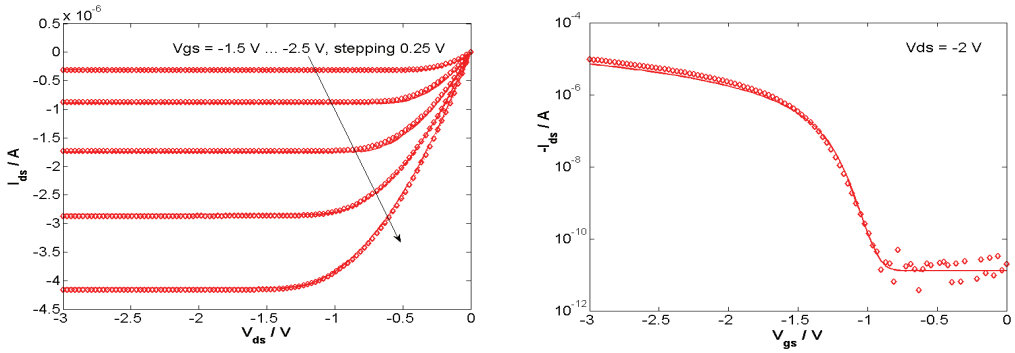


Fig. 2: Model (lines) compared to measurements (symbols): output characteristics (left) and transfer characteristics (right). We acknowledge the provision of measurements from Max Planck Institute (Stuttgart) and the IC-CAP software donation from Agilent.

## References

[1] K. N. Narayanan Unni, S. Dabos-Seignon, J.-M. Nunzi, Influence of the polymer dielectric characteristics on the performance of a quaterthiophene organic field-effect transistor, J. Materials Science, 41(2), 2006
[2] F. Hain, C. Lammers, M. Graef, A. Kloes, B. Iñiguez, Charge based, continuous current model for organic field effect transistors, ICOE 2014, Modena
[3] M. Estrada, I. Mejia, A. Cerdeira, et al., Mobility model for compact device modeling of OTFTs made with different materials. Solid-State Electronics, 52(5), 2008
[4] U. Zschieschang, F. Ante, D. Kälblein, et al., Dinaphtho [2, 3-b: 2, 3-f] thieno [3, 2-b] thiophene (dntt) thin-film transistors with improved performance and stability, Organic Electronics, vol. 12, no. 8, 2011

# Approaches for Multiscale Simulation of Nanoscale Transistors

Fabian Hosenfeld

Competence Center for Nanotechnology and Photonics, Technische Hochschule Mittelhessen, Giessen, Germany; DEEEA, Universitat Rovira I Virgili, Tarragona, Spain; Mail: Fabian.Hosenfeld@ei.thm.de; Phone: +49 641 309 1971; Fax:+49 641 309 2916

## Abstract

Multiscale simulation deals with the problem of device simulation, its effects in the atomic scale and the calculation of the device terminal voltages [1]. Shown are approaches to a solution which deals with both scales. In this paper a dynamic Look up table is introduced, which increases the numeric efficiency of analytical models. Additionally, an approach for a combination of an analytical potential calculation and the NEGF for multiple-gate FETs (MuGFET) is shown. Both methods are investigated for a DG MOSFET.

## 1. Introduction

Compact models are the common way to simulate circuits in circuit simulators. They provide a fast and efficient way of simulation. The models need to be numerically efficient i.e. numerically closed equations, to limit the simulation time. Iterative solutions like the finite element method (FEM) result in a higher accuracy but can only be used for one or a few devices. In nanoscale transistors quantum effects have to be considered increasingly. To consider the special effects of nanostructures, the Non-Equilibrium Green's Functions (NEGF) was established [2]. This iterative solution needs plenty of iterations and calculation time as well as much storage to record the state variables of the 2D or 3D simulation. To merge these two methods, in this work simple elements like contact resistance of a transistor are described analytically. In such regions, that need a description of the local state variables, the NEGF without iteration is used.

## 2. Dynamic Look Up Tables

The dynamic look up table is a mixture of a conventional LUT and an analytical model and merges the advantages of both. The dynamic LUT does not need a precalcultation to fill up the table and works only while the simulation is running [3]. To calculate a value of a model during the simulation, it first must be checked if the needed value can be interpolated by using the existing grid points of the table. Otherwise, the grid points have to be calculated using the analytic model and to be stored in the table. With the usage of a dynamic LUT, the numeric efficiency of analytic models should be increased. The dynamic LUT consists of an interpolation method and a data structure. The dynamic LUT saves the results, depending on the input variables, in the data structure. Additionally, the dynamic LUT can save the interpolation parameters of each cluster in the same structure. This method gains an time profit to the cost of an extra data memory.

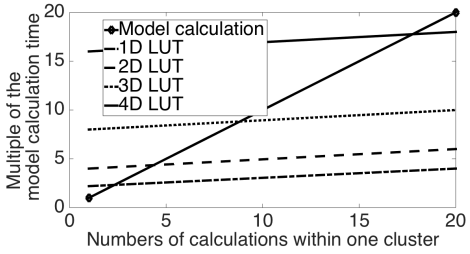


**Fig. 1.** Calculation time for an dynamic LUT which is ten times faster than a model calculation [3].

Fig. 1 shows the time profit of a dynamic LUT. For this example the interpolation time is assumed to be 10 times faster than a model calculation. The calculation of one value starts with a delay, because the cluster values have to be calculated. Further values can be interpolated much faster.

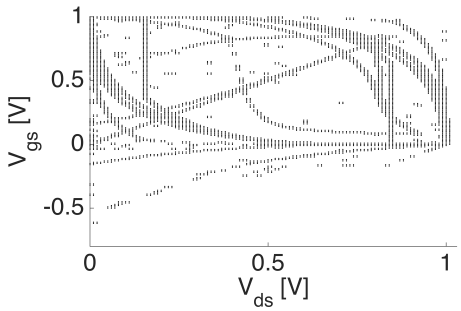


**Fig. 2**. State space of the dynamic LUT for a simulated ring oscillator [3].

The dynamic LUT was tested for the simulation of a ring oscillator. Each four dots mark one cluster. During 100,000 model calls the dynamic LUT made 3,860 model calculations to to fill the table. This gains an effort of 96%. Fig. 2 depicts the filled state space [3].

## 3. Potential Solution

The goal of the enhanced potential model is to provide a precise potential solution in all areas of the device. The first step to fulfill this goal is capturing and decomposing the given boundary conditions of the device to simplify the calculation of one complex problem to many separate much simpler tasks. The next step is the calculation of the effective built-in potential at the channel junctions by applying a model for standard inversion mode DG MOSFETs from [4]. The electrostatic potential in the channel region is based on two separately calculated solutions. The first one is a 2D closed-form solution of the Poisson equation with the conformal mapping technique [5]. The second one is the 2D closed-form parabolic solution, which has to be calculated to incorporate the parabolically shaped potential at the source- and drain-to-channel junctions [6].

## 4. Non-Equilibrium Green's Function

NEGF provides a fundamental basis for the development of atomic-level quantum mechanical simulators. The input parameters are the channel Hamiltonian and the in-scattering and broadening functions of the two contacts. The self-energy matrix describes the effects of the contacts on the channel. These inputs are used to calculate the correlation function $G^n$ that is needed to calculate the density matrix ρ. The electron density is build out of the diagonal elements of the density matrix. For an analysis of small devices, the NEGF equation is often used without the scattering process [7,8].

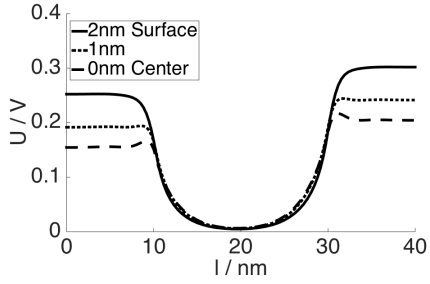


**Fig. 3.** Potential for the DGMOSFET at 3 different slices.

## 5. Fusion of Potential Solution and NEGF

The potential solution computes analytically the 2D potential for the given device at source, drain and channel. Each separate slice from the first gate to the second gate with the potential from source to drain is pushed successively to the NEGF. NEGF calculates for each energy state the electron density. The summed electron density is responsible for the current in one slice. Adding up the currents of each slice lead to the 2D device current.

## 6. Results

Simulated was a DGMOSFET using NanoTCAD ViDES [9] with a geometry of: $l_{sd}$=10nm; $l_{ch}$=20nm; $N_S=N_D=10^{20}cm^{-3}$; intrinsic channel; $t_{ox}$=1nm; $t_{ch}$=4nm and $V_{ds}$=0.05V;. Fig. 2 depicts the resulting potential at 3 different slices. Fig. 3 shows the potential at the channel surface for different gate voltages.

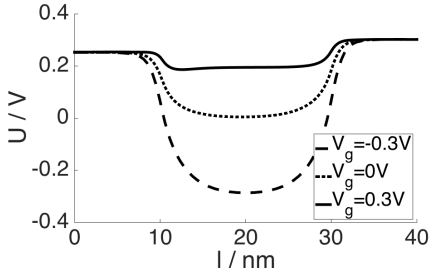


**Fig. 4.** Potential for the DGMOSFET at the surface for 3 different Gate voltajes.

## 7. Conclusions

In this abstract an approach for multi scale simulations of nano scale MuGFETs has been elaborated. It has been shown that a dynamic LUT could increase the efficiency of analytical models. An first step to integrate the NEGF in an analytical model was introduced.

**References**

[1] F.Ortmann, S. Roche, et al.,"*Multi-°-Scale Modeling for Devices and Circuits,*" E-Nano Newsletter Special Issue April 2012, Phantoms Foundation, Madrid, 2012.

[2] M. P. Anantram, M. S. Lundstrom et al., "*Modeling of Nanoscale Devices,*" Condensed Matter: Mesoscale andanoscale Physics, 2007.

[3] F. Hosenfeld," *Dynamic Lookup Table for Compact Models in Circuit Simulators,* " Master Thesis, 2014.

[4] T. Dutta, Q. Rafhay, G. Pananakakis, and G. Ghibaudo, "*Modeling of the Impact of Source/Drain Regions on Short Channel Effects in MOSFETs*," in Ultimate Integration on Silicon (ULIS), 2013 14th International Conference on, pp. 69–72, March 2013.

[5] E. Weber, Electromagnetic fields, Vol.I*., Mapping of fields.* John Wiley, New York, 1950.

[6] M. Graef et al. "*Improved analytical potential modeling in double-gate tunnel-FETs*," Mixed Design of Integrated Circuits & Systems (MIXDES), 2014 Proceedings of the 21st International Conference , vol., no., pp.49,53, 19-21 June 2014.

[7] S. Datta, "*Electrical Resistance: an AtomisticView*," in Nanotechnology 15, S433, 2004.

[8] S. Datta, "*Nanoscale Device Modeling: the Green's Function Method*," in Superlattices and Microstructures, vol. 28, no. 4, 2000.

[9] NanoTCAD ViDES, http://www.gianlucafiori.org/.

# Minimum DC-link Capacitor for Single-phase Power Factor Correction Applications

A. Marcos-Pastor, E. Vidal-Idiarte, A. Cid-Pastor and L. Martínez-Salamero
*Industrial Electronics and Automatic Control Research Group.*
*Electrical, Electronics and Automatic Control Engineering Department.*
*Universitat Rovira i Virgili. Tarragona, Spain.*
e-mails: {adria.marcos, enric.vidal, angel.cid, luis.martinez}@urv.cat

***Abstract* — In this paper, the calculation of the minimum DC-link capacitor for single-phase boost-converter-based Power Factor Correction (PFC) circuits is presented. The minimum necessary DC-link capacitor is obtained as a function of the mains characteristics, the maximum power operation of the system and the desired *rms* value of the DC-link voltage at this power operation point. Since any reduction of the DC-link capacitance results in an increase of the voltage capacitor ripple, it results in a high deformation of the inductor current ripple if a constant switching frequency controller is employed on PFC stage. Hence, the use of use variable switching frequency control techniques such as hysteretic controllers becomes more recommendable.**

## I. INTRODUCTION

MANY single-phase power conversion systems are based on two consecutive stages, a front-end switched-mode power converter for Power Factor Correction (PFC) followed by a second converter. Both stages are connected by the DC-link capacitor which is designed traditionally according two specifications: the hold-up time and the maximum DC-link voltage ripple. In particular, the last one is usually set very low (less than a 10% of the *rms* value of the DC-link voltage), this resulting in a capacitance sufficiently large in order to decouple both stages [1].

Electrolytic capacitors have been preferred in high voltage applications as DC-link capacitors since they offer a smaller size according their capacity. However, their short lifetime has promoted their replacement for film capacitors in some applications, e.g. LED-based lightning or battery chargers for Electric Vehicles (EV) [2]. The bigger size of film capacitors has leaded the research to focus on the reduction of the DC-link capacitance to develop high-density power converters. The problem is that this reduction should not compromise the achievable Power Factor (PF) or the Total Harmonic Distortion (THD) of the PFC stage.

In this work, the reduction of the DC-link capacitor is studied not only to find its minimum value but also in terms of the consequences that this reduction can generate on the performance of the PFC stage depending on the applied control technique. It is important to remark that the selected PFC topology for this study consists in a boost converter preceded by a diode bridge since it is the most popular front-end PFC circuit.

## II. DC-LINK CAPACITOR CONVENTIONAL DESIGN

The conventional design of the DC-link capacitor starts by modeling the front-end PFC stage as an ideal Loss-Free Resistor (LFR) and the second stage as a constant power sink as illustrated in Fig. 1. Grid current $i_{AC}(t)$ and grid voltage $v_{AC}(t)$ are defined as

$$v_{AC}(t) = V_M \sin(wt) \tag{1}$$

$$i_{AC}(t) = \frac{v_{AC}(t)}{r} \tag{2}$$

where $V_M$ and $w$ are the line's maximum voltage and angular frequency respectively. From the power balance conditions, it can be demonstrated that

$$v_C(t) = V_{C,rms}\sqrt{1 - \frac{P_{out}}{CwV_{C,rms}^2}\sin(2wt)} \tag{3}$$

where $V_{c,rms}$ is the *rms* value of $v_C(t)$, $C$ is the DC-link capacitance and $P_{out}$ is the absorbed power by the load. The minimum mathematical value for $C$ which ensures a real solution to (3) is the following

$$C_{\text{math}} = \frac{P_{out}}{wV_{C,rms}^2} \tag{4}$$

However, this value is not admissible in practice for a boost converter because it generates waveform $v_{C=Cmath}(t)$ which is sometimes lower than the rectified input voltage as it can be seen in Fig. 2. It can be demonstrated that the following expression is derived from (3) and it corresponds to conventional design for the DC-link capacitor under the maximum load conditions

$$C_{conventional} = \frac{P_{out,\max}}{wV_{C,rms}{}^2\Delta v_{C,RF}(\%)} \tag{5}$$

where $\Delta v_{C,RF}$ is the allowed ripple factor of $v_C(t)$. However, this expression is obtained from an approximation that can just be considered correct for $\Delta v_{C,RF}(\%)<10\%$.

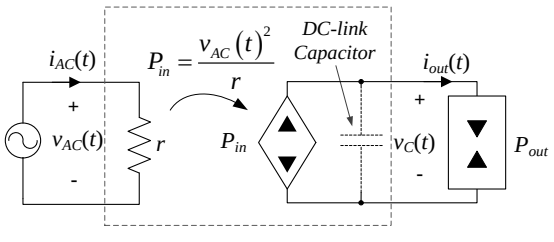


Fig. 1. Model of a single-phase two-stage-based PFC system.

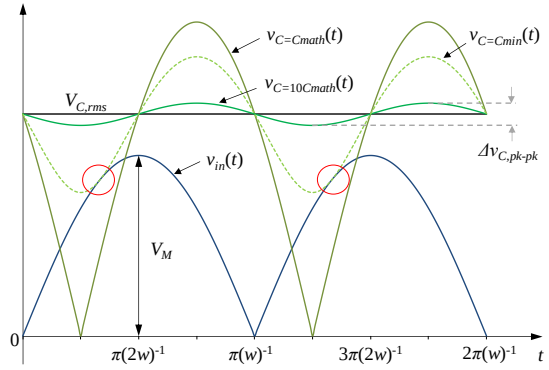


Fig. 2. Theoretic DC-link voltage waveforms for $C$=$C_{math}$, $C$=10$C_{math}$, $C$=$C_{min}$ and the rectified line voltage $v_{in}(t)$.

## III. Proposed Minimum DC-Link Capacitor Design

To obtain the minimum capacitor value, it is necessary to have as much DC-link voltage ripple as possible. Thus, considering that there is no restriction on the amplitude of the DC-link voltage ripple, the minimum value of the DC-link capacitor is the one that makes the DC-link voltage become tangent to the rectified input voltage as depicted in Fig. 2. Hence, we must start with the following equation $v_{in}(t)$= $v_C(t)$

$$\left|V_M \sin\left(wt\right)\right| = V_{C,rms}\sqrt{1-\frac{P_{out}}{CwV_{C,rms}^2}\sin\left(2wt\right)} \tag{6}$$

The minimum DC-link capacitor is obtained by isolating $C$ from (6)

$$C_{\min} = \frac{P_{out,\max}}{wV_{C,rms}}\sqrt{\frac{1}{V_{C,rms}^2 - V_M^2}} \tag{7}$$

Moreover, the final selected capacitor ($C_{sel}$) must be higher than the minimum value $C_{min}$. Fig. 3 illustrates two tri-dimensional graphs that compares the minimum DC-link capacitor as functions of parameters $P_{out,max}$ and $V_{C,rms}$ for both the conventional and the proposed method. This figure has been obtained considering the standard European line characteristics (230 $V_{rms}$ and 50 Hz) and $\Delta v_{C,RF}$=10% for the conventional design.

## IV. Simulation Results

Different simulations have been performed to compare the resulting operation of constant and variable switching frequency controllers. The selected system parameters are: $V_{AC}$=230 $V_{rms}$, $f_{AC}$=50 Hz, $P_{out}$=529 W, boost inductor 620 µH, DC-link capacitor 40 µF (designed for 1 kW) and $V_{C,rms\text{-}ref}$=347 V.

As it can be seen in Fig. 4.a the constant switching frequency is the responsible of a high distortion on the inductor current ripple $\Delta i_L(t)$ in case of having a high ripple of the DC-link voltage, while the hysteretic controller is capable to maintain it constant.

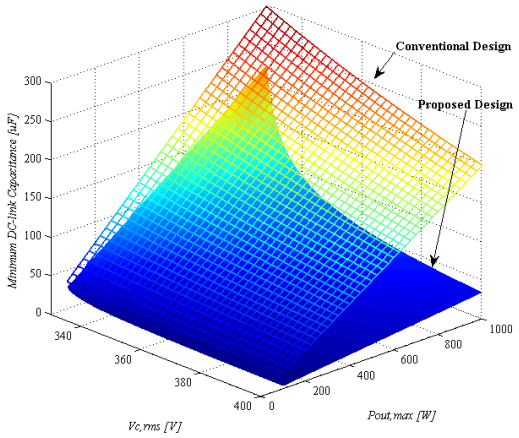


Fig. 3. Resulting DC-link capacitor value according to the conventional design ($\Delta v_{C,pk-pk}$=10%) and the proposed design as a function of voltage $V_{C,rms}$ and output power $P_{out}$ for standard European line characteristics.

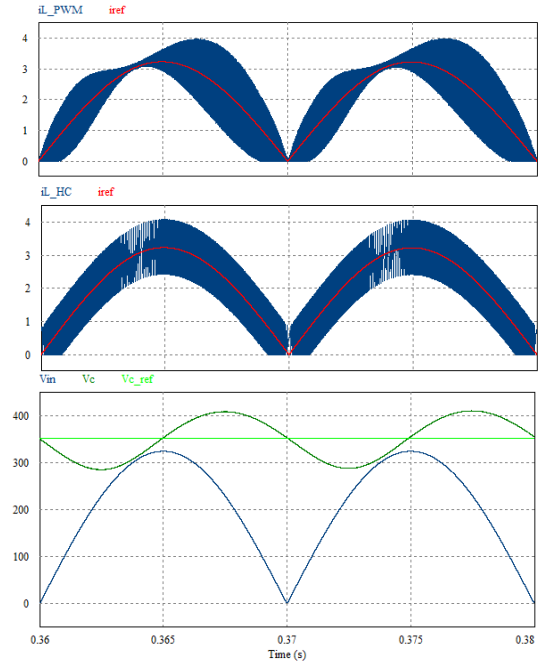


Fig. 4. Inductor current a) with constant switching frequency controller and b) with hysteretic current controller. c) Rectified input voltage $v_{in}(t)$, DC-link voltage $v_C(t)$ and DC-link voltage reference $V_{C,rms\text{-}ref}$

## V. Conclusions

In this work, the calculation of the minimum DC-link capacitance for a two-stage single-phase application with active power factor correction is presented considering that the second stage behaves as a constant power sink. The constant switching operation leads to a high deformation of the inductor current ripple which can detune the power quality.

## References


[1] W. H. Wolfle and W. G. Hurley, "Power factor correction and harmonic filtering for AC/DC converters," in *IECON 02 [Industrial Electronics Society, IEEE 2002 28th Annual Conference of the]*, 2002, pp. 3238-3243 vol.4.

[2] A. Tokumasu, H. Taki, K. Shirakawa, and K. Wada, "AC/DC converter based on instantaneous power balance control for reducing DC-link capacitance," in *Power Electronics Conference (IPEC-Hiroshima 2014 - ECCE-ASIA), 2014 International*, 2014, pp. 1379-1385.

# Decreasing Charge Recombination Losses in Perovskite Solar Cells Through the m-$TiO_2$/MAPI Interface Engineering.

Jose Manuel Marin-Beloqui[a], Luis Lanzetta[a] and Emilio Palomares[a,b]

a. Institute of Chemical Research of Catalonia ( ICIQ). Avda. Països Catalans, 16. Tarragona. E-43007. Spain
b. ICREA. Passeig Lluís Companys, 23. Barcelona. E-08010. Spain.
jmarin@iciq.es

## Abstract

Based on our experience on controlling the recombination kinetics in Dye Sensitized Solar Cells (DSSC) through the modification of the mesoporous $TiO_2$ (m-$TiO_2$) interface we have carried out the modification of the methyl ammonium lead iodide (MAPI) /m-$TiO_2$ interface with a nanoscopic layer of insulating $Al_2O_3$. The effects over the device efficiency, device reproducibility and the relationship between the observed increase in open-circuit voltage (Voc) and the presence of the $Al_2O_3$ layer is thoroughly discussed and explained. In contrast with the experimental observation in DSSC of $TiO_2$ conduction band edge shift for $Al_2O_3$ coated m-$TiO_2$ films, in MAPI perovskite solar cells the charge vs voltage measurements carried out under sun-simulated irradiation conditions results in almost identical exponential distribution. Nonetheless, an important decrease on the charge recombination lifetime is measured for the $Al_2O_3$ treated samples which lead to an improvement of the overall device efficiency and, moreover, on the device reproducibility.

## 1. Introduction

The use of methyl ammonium lead iodide (MAPI) perovskite-type semiconductor material has been the focus of increase interest for the development of efficient solar cells. In less than 5 years solar-to-electrical conversion efficiency have been increased from η=3.8%[1] efficiencies to near 20%[2], exceeding the top best efficiencies measured for other so-called third-generation solar cells such as DSSC (Dye Sensitized Solar Cells), OSC (Organic Solar Cells) and QDSC (Quantum Dot Solar Cells). The easy-to-fabricate procedures, materials low cost and past experience on the above mentioned solar cell technologies have paved the way for MAPI solar cells to become a hot spot in materials science for energy conversion devices such as solar cells and light-emitting diodes. Moreover, the recent discovery of the use of MAPI as semiconductor for solar cells, has also presented novel scientific challenges as for example, the explanation of the unusual large amount of measured charge on MAPI solar cells, the presence of hysteresis effects, the bi-exponential nature of the registered small-perturbation based Voc decays, the presence of interfacial dipoles, etc… Whilst, the increase in solar cell efficiency has been spectacular, with a learning-curve never seen for other solar cell technologies alike CdTe and CIS, among others, the knowledge, however, on the detailed mechanisms that allows the efficient conversion of sun-light into electrical current have been less explored with remarkable exceptions and, moreover, there is still the scientific challenge to approach MAPI solar cells to their maximum theoretical efficiency through the reduction of charge recombination losses, better spectral response and , moreover, increasing operational stability.

In the present work we have fabricated MAPI perovskite solar cells with the archetypal structure mentioned above as well as MAPI perovskite solar cells with an $Al_2O_3$ insulating overlayer onto the nanocrystalline $TiO_2$ particles that conform the m-$TiO_2$ layer. The former will be described along this work, as MAPI perovskite solar cells while the later will be designed as $Al_2O_3$-coated perovskite solar cells. Moreover, we have used advanced photo-induced characterisation techniques, namely photo-induced transient photo-voltage (PIT-PV), photo-induced differential charging (PIDC) and photo-induced transient photo-current (PIT-PC) to thoroughly analyse the differences in charge density (defined as the total accumulated charge in the device at a given bias), the charge recombination lifetime and the relationship between both mentioned parameters. The findings described below are key to (a) understand further the device charge recombination processes that hamper the solar-to-electrical current conversion efficiency and (b) to increase the device fabrication reproducibility through interface engineering.

## Results and Discussions

As can be seen in **Figure 1**, solar cells using $Al_2O_3$ m-$TiO_2$ coated MAPI perovskite solar cells show an increase in Voc and photocurrent leading to an average efficiency of $\eta_{Al2O3}$=12% in contrast to standard MAPI perovskite solar cell that show a standard average efficiency of η=10.2%.

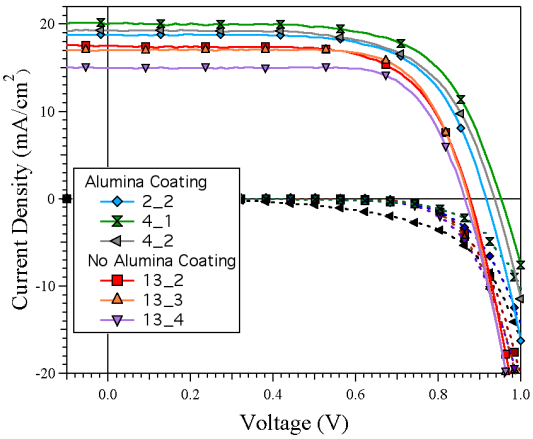


**Figure 1.** Several MAPI perovskite solar cells with and without the $Al_2O_3$ modified m-$TiO_2$/MAPI interface under 1 sun illumination and the corresponding dark curves (dashed lines).

Further measurements of solar cells fabricated in different days and conditions, as the devices depicted and listed in **Figure 1** respectively, but always keeping identical measurement and fabrication conditions within each set of samples of $Al_2O_3$ coated m-$TiO_2$ and the corresponding MAPI perovskite solar cells as control show identical trend with the $Al_2O_3$ modified m-$TiO_2$/MAPI interface having higher Voc and, in average, higher solar-to-energy conversion efficiency.

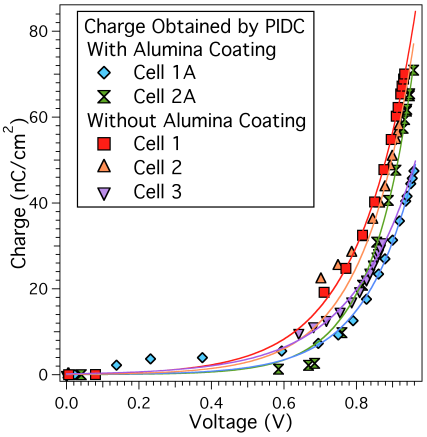


**Figure 2.** Measured charge using PIDC at different solar cell voltage from MAPI perovskite solar cells and coated perovskite solar cells.

As seen in **Figure 2,** there was no any shift in the charge distribution indicating that there was no any negligible change in the conduction band of the mp-$TiO_2$. This was different to the previous case reported in DSSC[3] where the coating induced a displacement of the conduction band of the mp-$TiO_2$.

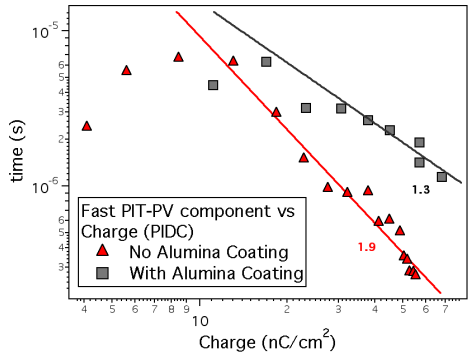


**Figure 3.** Non-radiate carrier recombination lifetime (fast component PIT-PV decay) vs solar cell electrical charge measured by PIDC. The numbers correspond to the recombination order factor (OF).

**Figure 3** shows the comparison between the recombination lifetimes of the fast component in the decay obtained by PIT-PV compared with the charge obtained by PIDC. It was seen that alumina coating leads to slower interfacial charge recombination lifetimes when compared to standard mp-$TiO_2$. This indicates that physical barrier over the mesoporous nanoparticles avoids to electrons to recombine with the holes in the OMeTAD.

Also, the slower component of the decay obtained by PIT-PV was slowed down by the alumina coating, indicating that the coating also takes part in the recombination process that correspond to this part of the decay, that still remains unclear.

## Conclusions

We have used alumina conformal coating from solution processed methods onto mesoporous $TiO_2$ electrodes used in the preparation of efficient MAPI perovskite solar cells. This coating leads to an improvement in the solar cell efficienc mainly due to a higher open circuit voltage (Voc).

Also, we have studied the interfacial charge recombination processes using photo-induced time resolver methods in complete devices under sun-simulated irradiation conditions. Using and PIDC we have not observed a clear shift on the exponential charge distribution.

The analysis of the PIT-PV decays shows two different time components, in good agreement with previous measurements with other MAPI perovskite solar cells. In fact, for $Al_2O_3$ coated solar cells both time components present at the PIT-PV decay are slower in comparison with the standard MAPI perovskite solar cell. A careful comparison of both charge recombination lifetime components at the same charge density further confirms that the recombination lifetime for $Al_2O_3$ treated solar cells is significantly slower.

## References

**[1]** A. Kojima, K. Teshima, Y. Shirai and T.Miyasaka, *J. Am. Chem. Soc.*, 2009, **131**, 6050-6051.

**[2]** W. S. Yang, J. H. Noh, N. J. Jeon, Y. C. Kim, S. Ryu, J. Seo and S. I. Seok, *Science*, 2015.

**[3]** E. Palomares, J. N. Clifford, S. A. Haque, T. lutz and J. R. Durrant, *Chemm. Comm.*, 2003, **125**, 475-482.

# Detection of Fc-y receptors in platelets via new generation fluorescent materials

**Alba Matas Adams [a], Georgiana Stoica [*,a], Emilio Palomares [a,c], and Mihaela Delcea [b]**

[a] *Institute of Chemical Research of Catalonia (ICIQ), Avinguda del Països Catalans 16, 43007 Tarragona, Spain. Fax: +34 977 920 823; Tel: +34 977 920 200; E-mail: gstoica@iciq.es*

[b] *Nanostructure Group, ZIK HIKE - Center for Innovation Competence, Humoral Immune Reactions in Cardiovascular Diseases, Ernst-Moritz-Arndt-Universität, Greifswald, 17489 Greifswald, Germany. Fax: +49 3834 86 22341; Tel: +49 3834 86 22343*

[c] *Catalan Institution for Research and Advanced Studies (ICREA), Passeig de Lluis Companys 23, 08010 Barcelona, Spain*

## Abstract

Platelets are anucleate cells; fragments of cytoplasm with a discoid shape, derived from megakaryocytes of the bone marrow of mammals, present in blood.
They play an important roll in the control of different diseases as well as blood related problems.
One of the most important receptors that control in a big percentage this roll of the platelets, is the Fcγ receptor.
Here we will tag, detect and try to track these receptor using a one to one approach with Quantum Dots (QD) and try to understand the mechanism of this interaction.

## Introduction

Plateles are the smallest elements present in blood with sizes ranging from 2-4 μm in diameter. Despite their small size and the fact they are cell fragments, they play an important role in blood clotting due to the proteins displayed on their surface, that allow them to stick to blood vessel walls and to each other.
This role is controlled by the many receptors present in their surface, including integrins, leucine-rich repeated receptors, tyrosine kinase receptors, and the object of our study, proteins belonging to the immunoglobulin superfamily with particular emphasis on the Fcγ receptors (FcγR), most importantly FcγRIIA [1]
In humans, the Fcγ system is the most complex, and it can be classified in FcγRI and FcγRII, as they present differences in the intracellular domains and cellular expression [2]. These families are categorized following the level of affinity to IgG and the signaling cascade it triggers.
The case of our study (FcγRIIA) presents low to medium affinity to IgG and the crystal structure of this receptor complexed with IgG showed that it is a 1:1 stoichiometric interaction[3,4].

For the platelet adhesion to the vessel wall, an interaction of the platelet with collagen is required, but the exact mechanism is not clearly understood [5]. But there is evidence of a complex to the FcR γ-chain dimer, and it has been proven that without these receptors the thrombus formation is reduced.[6,7]
Regarding this thrombus formation, Fc γ receptors, most importantly, FcγRIIa (CD32), are also a key factor in heparin-induced thrombocytopenia, a potentially devastating immune mediated adverse drug reaction, due to the treatment with heparin, which instead of preventing clot formation, promotes the adverse effect, producing also a low platelet count [8].

Another important role of these receptors is as regulators of the immune response [2], due to their binding to the Fc part of the antibody attached to infected cells or invading pathogens.

Until now, for the detection of single molecules or a small number of molecules in living cells (including proteins), fluorescent dyes were used, but their applicability was restricted by the photobleaching[9]. Lately, these materials have been substituted by quantum dots (QDs), that have been widely used in the past few years as labeling and imaging agents [10] due to their narrower emission spectrum, larger photostability, and higher brightness.
Besides, the emission spectrum is tunable by controlling the size during the synthesis, that ranges form 2-15 nm [11]. Moreover, the emission can be tracked for longer periods of time, as they do not present photobleaching.

These systems have been used to determine the diffusion characteristics of individual receptors and their subcellular location over time [12-14], like the diffusion dynamics of Glycine Receptors [15], GABA (γ-aminobutyric acid) receptors [16], or even the rotation of the Fc receptors[17].

There are around 5000-8000 Fc–γ receptors continuously on the platelets surface able to detect the immune complexes or the pathogens. Thus, an innovative strategy using long-fluorescence-lifetime

labels allowing high-throughput screening and multiplexed detection on commercially available equipment is necessary.
Here we report for the first time, to our knowledge, a library of bioconjugated QDs for specific detection of the FcγRIIA, using IgG and the Fc fragment of IgG.

### Bioconjugation of IgG and Fc fragment to Quantum Dots.

For the bioconjugation, 100 nM Carboxyl 605 nm QDs (605 QDs) were mixed with EDC in a 1:150 molar ratio at 4º for 30 min, then the proteins for each conjugation (IgG and Fc fragment) in different molar ratios (from 1:0 to 1:16) were added to a final volume of 250 µL with PBS in a shaker at 400 rpm, 20ºC for 2 hours (Table 1).
The sample was centrifuged and washed with PBS three times and finally the pellet was resuspended in PBS to a final volume of 250 µL.

### Incubation of bioconjugated QDs with platelets

Platelets (300.000 platelets per µL) were isolated from blood of healthy patients as described [18] .
For the incubation with the conjugates, 5 µL of platelets were diluted to a final volume of 55 µL in PBS (around 30.000 platelets).
The total volume was placed in a round Petri dish for 10 min for the platelets to settle, followed by washing with PBS to eliminate the floating platelets.
Finally, 10 µL of the sample were added over the remaining platelets.

## Results and discussion

### Conjugation mechanism of IgG and Fc to 605QDs

Activation of the carboxyl-functionalized 605QDs leads to the formation of a reactive ester by the crosslinking effect of EDC, as shown in **Scheme 1**, which can easily react with the free amino groups present in the protein[19].

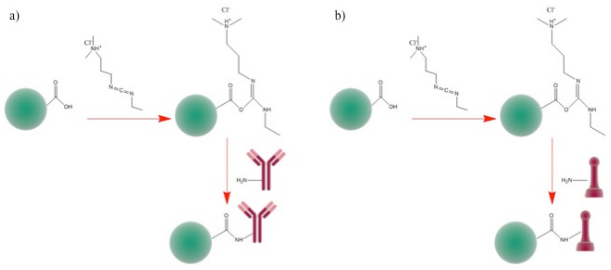


***Scheme 1***. *Conjugation of 605QD to a) IgG, b)Fc fragment.*

Once the conjugation was finished and the products were washed, an AGE electrophoresis was done. As shown in **Figure 1**, the fluorescence from the QDs was recorded, and in the case of 605QDs-IgG (**Figure 1a**) starting with the 1:0.5 molar ratio a fine band appears that gets more and more intense when the molar ratio is higher, even though the conjugation is not 100% effective (free 605QDs are seen). In the case of 605QDs-Fc something similar happens, most of the QDs are still free (as seen in the bands in the same position as the free QDs, but in this case, the bands of the conjugation are a lot lower as the molecular weight of the Fc fragment is a lot smaller than in the case of the IgG (150KDa vs. 50KDa), so the conjugated band is quite close to the free QDs.

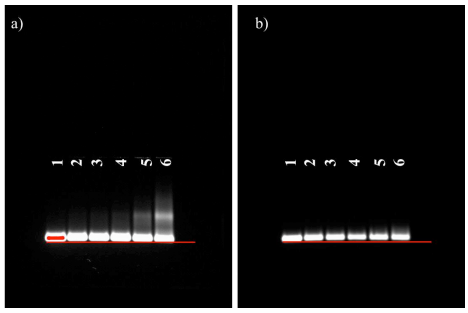


***Figure 1.*** *AGE of a) 605QDs-IgG, b) 605QDs-FcLanes: 1) Free 605 QDs, 2) 605QDs-Protein (1:0.5), 3) 605QDs-Protein (1:1), 4) 605QDs-Protein (1:2),5) 605QDs-Protein (1:2), 6) 605QDs-Protein (1:16)*

### Detection of FcgRIIa receptors by bioconjugated QDs

The fluorescent nanoprobes (final concentration of 2nM of QDs) were incubated with the platelets, as previously described but only the images obtained after washing will be displayed.

**Figure 2** shows the control experiments, that is the incubation of the platelets with free 605QDs (**Figure 2a**) and with 605QDs conjugated to BSA (**Figure 2b**). From **Figure 2a** it is clear that free 605QDs interacted with the cell marking the whole cell. It has been seen that free QDs of any type are able to penetrate different cells lines membrane, but the reason behind this is not so well known (it could be due to size, charge…).[20, 21] This same phenomenon was observed after the incubation with 605QDs conjugated to BSA (**Figure 2b**) contrary to our expectations. The signal comes from unspecific binding of BSA to the receptors in the surface[22], but if a competition assay was done with 605QDs-BSA and 605QDs-IgG it preferentially will uptake the 605QDs-IgG as shown in previous work by Neuwirth et al[23].

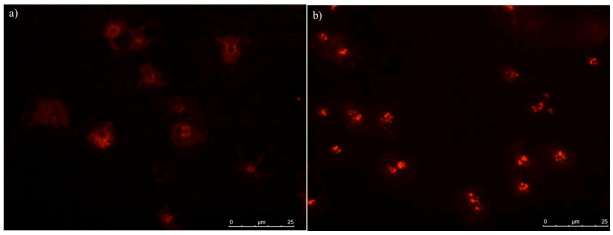


***Figure 2.*** *Incubation of platelets with a) free 605QDs+platelets b) 605QDs-BSA (1:20)+ Platelets. QDs working concentration was 2nM.*

To be able to detect this receptor, the platelets were incubated with the conjugated 605 QDs as in **Scheme 2,** which illustrates the interaction of the conjugated 605QDs with the Fc receptors after incubation. The receptor detects and binds to the IgG (**Scheme 2a**) conjugated to the 605QD, which fluorescence is used to track the receptor in the membrane over time. The same is done for the Fc fragment of IgG (**Scheme 2b**).

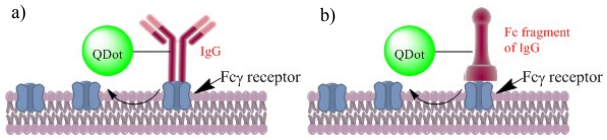


***Scheme 2.*** *Tracking of the Fc receptor with a) 605QDs-IgG, b) 605QDs-Fc fragment.*

**Figure 4** shows the result of the incubation, clearly showing that the marking is different from the marking in the controls. While in the controls the center body of the cells presented the more predominant fluorescent, after the incubation with the conjugates, in these two cases, the same patterning of fluorescence is observed, the membrane as well as the center body of the cell is marked. This is in agreement with the expected, as the Fcγ receptors are in the membrane of the cell.

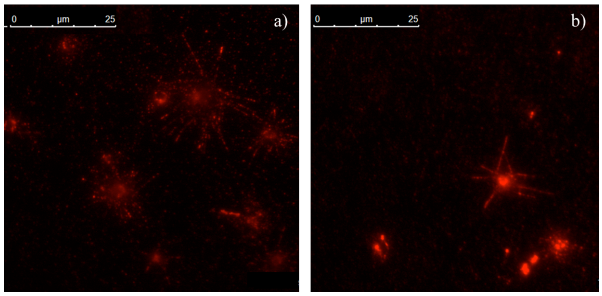


***Figure 4.*** *Incubation of platelets with a) 605QDs-IgG b) 605QDs-Fc fragment. QDs working concentration was 100pM. Molar ratio 1:1*

After the incubation and washing, the images were recorded every 100 ms to a total of 2000 frames to detect each 605QDs bonded to the Fc receptor and follow it.

**Figure 5** depicts the movement of possibly a single Fc receptor after 100 ms, marked with an arrow it is seen how the fluorescent dot moves from its original position (**Figure 5a**) after 100 ms (**Figure 5b**).

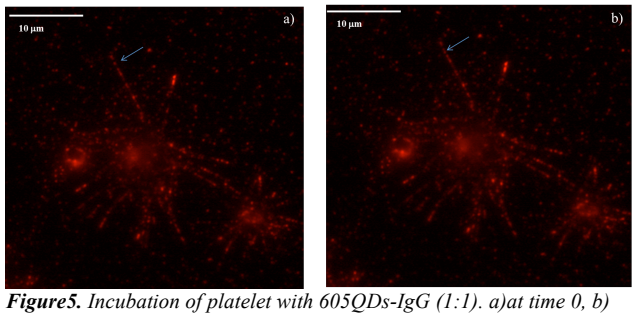


***Figure5.*** *Incubation of platelet with 605QDs-IgG (1:1). a)at time 0, b) after 100 ms.*

## Conclusion

Taking advantage of the QDs activation thanks to the effect of EDC and sulfo-NHS, a bioconjugation of these QDs to proteins such as IgG and the Fc receptor part of IgG was achieved to detect the Fcγ receptors present in platelets.

Not only the receptors were detected and visualize by fluorescence microscopy, but also they could be tracked over a period of time along the membrane, a single receptor at a time, something not done until now to our knowledge.

The only problem present in this work is that the control experiment does not give enough evidence as to how the interaction between the functionalized quantum dot and the platelet is controlled. This has to be done in further experiments.

## References

1. Rivera, J., et al., *Platelet receptors and signaling in the dynamics of thrombus formation.* Haematologica, 2009. 94(5): p. 700-711.
2. V.Ravetch, F.N.J., *Fc gamma receptors as regulators of immune responses.* Nature Reviews Immunology, 2008. 8: p. 15.
3. Kato, K., et al., *A conformational change in the Fc precludes the binding of two Fcγ receptor molecules to one IgG.* Immunology Today, 2000. 21(7): p. 310-312.
4. Zhang, Y., et al., *Crystal Structure of the Extracellular Domain of a Human FcγRIII.* Immunity. 13(3): p. 387-395.
5. Savage, B., M.H. Ginsberg, and Z.M. Ruggeri, *Influence of Fibrillar Collagen Structure on the Mechanisms of Platelet Thrombus Formation Under Flow*. Vol. 94. 1999. 2704-2715.
6. Kato, K., et al., *The contribution of glycoprotein VI to stable platelet adhesion and thrombus formation illustrated by targeted gene deletion*. Vol. 102. 2003. 1701-1707.
7. Poole, A., et al., *The Fc receptor γ-chain and the tyrosine kinase Syk are essential for activation of mouse platelets by collagen*. Vol. 16. 1997. 2333-2341.

8. Udeh CI, D.A., Udeh BL, Hata JS, *Heparin-induced thrombocytopenia: a clinical and economic review.* OA Anaesthetics, 2013. 1(1): p. 3.
9. Baba K, N.K., *Single-Molecule Tracking in Living Cells Using Single Quantum Dot Applications.* Theranostics, 2012. 2(7): p. 12.
10. Bruchez, M., et al., *Semiconductor Nanocrystals as Fluorescent Biological Labels.* Science, 1998. 281(5385): p. 2013-2016.
11. Neeleshwar, S., et al., *Size-dependent properties of CdSe quantum dots.* Physical Review B, 2005. 71(20): p. 201307.
12. Bats, C., L. Groc, and D. Choquet, *The Interaction between Stargazin and PSD-95 Regulates AMPA Receptor Surface Trafficking.* Neuron. 53(5): p. 719-734.
13. Groc, L., et al., *Differential activity-dependent regulation of the lateral mobilities of AMPA and NMDA receptors.* Nat Neurosci, 2004. 7(7): p. 695-696.
14. Groc, L., et al., *Surface Trafficking of Neurotransmitter Receptor: Comparison between Single-Molecule/Quantum Dot Strategies.* The Journal of Neuroscience, 2007. 27(46): p. 12433-12437.
15. Dahan, M., et al., *Diffusion Dynamics of Glycine Receptors Revealed by Single-Quantum Dot Tracking.* Science, 2003. 302(5644): p. 442-445.
16. Lévi, S., et al., *Homeostatic Regulation of Synaptic GlyR Numbers Driven by Lateral Diffusion.* Neuron. 59(2): p. 261-273.
17. Winter, P.W., et al., *Rotation of Single Cell-Surface Fc Receptors Examined by Quantum Dot Probes.* Biophysical Journal. 102(3): p. 653a-654a.
18. Warkentin TE, G.A., *Laboratory testing for heparin-induced thrombocytopenia.* Heparin-induced Thrombocytopenia New York, NY: Informa Healthcare, 2007: p. 227-238.
19. Wang, S., et al., *Antigen/Antibody Immunocomplex from CdTe Nanoparticle Bioconjugates.* Nano Letters, 2002. 2(8): p. 817-822.
20. Fontes, A., et al., *Quantum Dots in Biomedical Research*. Biomedical Engineering - Technical Applications in Medicine. 2012.
21. Biju, V., T. Itoh, and M. Ishikawa, *Delivering quantum dots to cells: bioconjugated quantum dots for targeted and nonspecific extracellular and intracellular imaging.* Chemical Society Reviews, 2010. 39(8): p. 3031-3056.
22. Kudolo, G.B. and M.J. Harper, *Estimation of platelet-activating factor receptors in the endometrium of the pregnant rabbit: regulation of ligand availability and catabolism by bovine serum albumin.* Biology of Reproduction, 1990. 43(3): p. 368-377.
23. Neuwirth, R., et al., *Evidence for immunoglobulin Fc receptor-mediated prostaglandin2 and platelet-activating factor formation by cultured rat mesangial cells.* The Journal of Clinical Investigation, 1988. 82(3): p. 936-944.

# Carbon quantum dots (CQDs) as hole transporting material for LED's

Sofia Paulo Mirasol*, Emilio Palomares

Institute of Chemical Research of Catalonia (ICIQ)
* spaulo@iciq.es

## Abstract

The last three months, I focused to synthetize and characterized different carbon quantum dots using different proceeded. I have tried to dope with two types of rare earth to know if our CQDs could emitted at different wavelengths. One of the challenges is used carbon quantum dots as hole transporting material for LEDs.

## 1. Introduction

Researches groups are investigated LEDs as a promising and suitable light source. Nowadays LED technology continues to identify and synthetize new emitter material to improve the power efficiency.
One of the emitters materials that I have been working were carbons quantums dots. Colloidal semiconductor nanocrystals or quantum dots are inorganic fluorescent semiconductor nanocrystals with size of a few nanometers. Quantum dots have been researched for their special optical properties, as the possibilities to control their color converting characteristic, to use in photovoltaic devices. Furthermore, CQDs have a great potential due to its unique photoluminescence and less toxic properties.

## 2. Experimental section [1,2]

I'm going to explain one of the procedures that I have done to synthetized and characterized CQDs.

Prepare 0,5ml of 30% sucrose (300mg/1mL $H_2O$) and 0,5ml of 200mg/mL of $YbCl_3 \cdot 6H_2O$. Both dissolution and 100µL of concentrated $H_2SO_4$ are added to 3mL of diethylene glycol (DEG) in a 20mL glass tube. The mixture was sonicated and then is heated in a microwave at 200 °C, 50seg. The mixture changed from colorless to dark brownish.
The suspension is centrifuged 30min to 3500 rppm. After that, didn't observe any solid so I added 10mL of $H_2O$ and centrifuged again. I removed the solid that appears, and then we divided de solution in two tubes, added 30mL and repeat the process twice. Carbon quantum dots were stored in water.

The sample was characterized by Transmission Electron Microscopy (TEM ), fluorescent spectrophotometry and absorption spectrophotometry.

In figure 1, I could observe the UV-visible absorption spectrum displayed a maximum at 350nm.
In the emission spectrum (figure 2), I could observe two different bands, one at λ= 435nm and λ=520nm. It could be because I have two types of CQDs, one doped with Ytterbium and the other not.

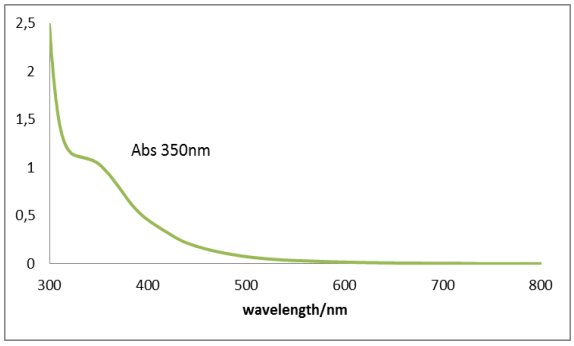


**Fig 1**. UV-vis spectrum.

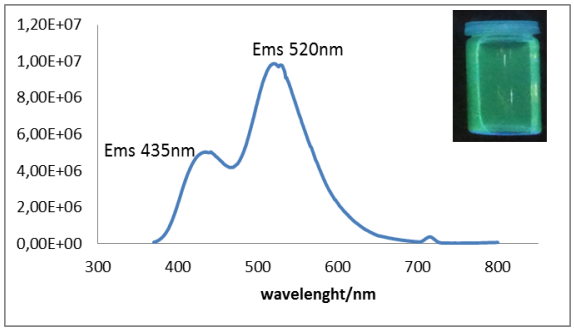


**Fig2.** Inset shows the real-color emission under UV-light (λ=365nm). Curve of the emission spectra ($\lambda_{exc}$=360nm).

The morphology and size of Yb-CQDs fabricated by the microwave-assisted method were observed by transmission electron microscopy (TEM) imaging (Figure 3). The spherical shape and the size of CQDs are between 2-4nm.

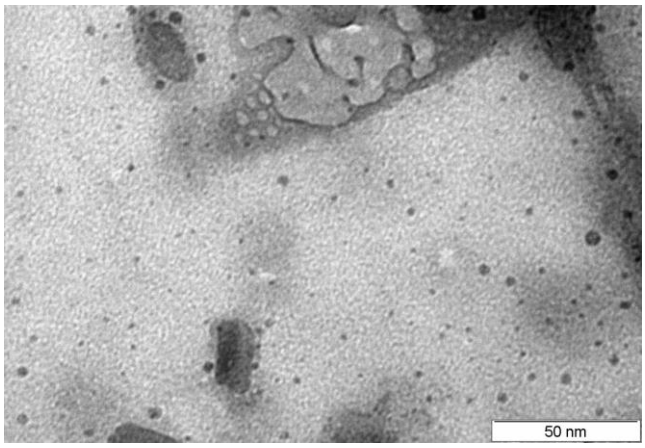


**Fig 3.** TEM image of CQDs doped with Ytterbium. The scale bar is 50nm.

R**eferences**

[1] Ningqiang Gong, Hao Wang, Shuai Li, Yunlong Deng, Xiao'ai Chen, Ling Ye, Wei Gu Microwave-Assited Polyol Sunthesis of Gadolinium-Doped Green Luminiscent Carbon Dots as a Bimodal Nanoprove. Langmuir (2014),30, 10933-10939

[2] Yang, Z.; Li, Z.; Xu, M.; Ma, Y.; Zhang, J.; Su, Y.; Gao, F.; Wei, H.; Zhang, L. Controllable Synthesis of Fluorescent Carbon Dots and Their Detection Application as Nanoprobes. Nano-Micro Letters. 2013, 5, 247-259.

# Layer by layer polyelectrolytes deposition on Nanoporous Anodic Alumina for a stimuli-responsive drug release

Maria Porta-Batalla, María Alba, Gerard Macias, Pilar Formentín, Lluís F. Marsal*

Departemant d'Enginyeria Electrònica, Elèctrica i Automática, ETSE, Universitat Rovira i Virgili, Avda. Països Catalans 26, 43007 Tarragona, Spain

*Corresponding author. Tel: 977 559 625 E-mail: lluis.marsal@urv.cat

## Abstract

Stimuli-responsive materials that could change their properties and structures in response to external stimuli have recently received much attention owing to their many potential applications in drug delivery systems. Among various preparation methods to realize these goals, layer-by-layer (LBL) assembly, based on polyelectrolytes leading to swellable multilayers, is a powerful processing method because it can be applied to substrates of any shape and size and, at the same time, the multilayer films assembled under specific conditions show a strong swelling behavior that can be modulated in response to post-treatment conditions. The aim of this study is to use polyelectrolytes multilayers onto de nanoporous anodic alumina (NAA) in order to have the maximum surface to load the drugs and have a retained drug release compared to those samples without polyelectrolytes.

## 1. Introduction

Since the human body exhibits variations in pH along the gastrointestinal tract from the stomach (pH 1.0 - 3.0), to the small intestine (pH 6.5-7.0), to the colon (pH 7.0-8.0) and also in some specific areas like tumoral tissues (pH 6.5-7.2) and subcellular compartments, such as endosomes/lysosomes (pH 5.0-5.5), one very important drug delivery system is those sensitive to the pH. With this state of the art, pH-sensitive polyelectrolytes are good candidates for drug delivery uses.

## 2. Experimental Section

**Nanoporous alumina anodization**

Ordered nanoporous anodic alumina (NAA) was prepared by the two-step anodization method.

High purity (99.999%) aluminum plates were purchased from Goodfellow (Huntingdon, UK). Perchloric acid and phosphoric acid which were used as electrolytes, for anodization (phosphoric acid) and electropolishing (perchloric acid), were purchased from Sigma-Aldrich Corporation (St Louis, USA).

Aluminum plates were degreased in acetone and ethanol to eliminate organic impurities. They were then subsequently electropolished in a mixed solvent of perchloric acid and ethanol (1 : 3) at a constant applied voltage of 20 V for 4 minutes.

To suppress breakdown effects and to enable uniform oxide film growth at high voltage (194V in phosphoric acid) a protective layer at lower voltage (174V in phosphoric acid) was performed for 180 min. After this pre-anodization a ramp of 0,05V/s was used to reach the hard voltage (194V) during 24h. Then, after this first step, the porous alumina grown on the aluminum surface was removed by a wet chemical etching in a mixture of phosphoric acid (0,4M) and chromic acid (0,2M) (1:1 volume ratio) at 70ºC.[1] The second anodization step was performed under the same experimental conditions (194V) as they were used in the first step in order to obtain ordered nanoporous alumina.

**APTES functionalization**

In order to develop a surface able to attach the polyelectrolytes NAA substrates were treated with hidrogenperoxide ($H_2O_2$) at 70ªC during 30 minutes to obtain a hydroxyl group on the surface. Then the samples were completely dried. Then the samples were maintained under nitrogen atmosphere during all the (3-Aminopropyl)-triethoxysilane (APTES) reaction. 20ml of dry toluene was added to the samples followed by 0,2 ml APTES to obtain a 1% (v/v) concentration of the silane in the mixture. Then the solution was stirred for 1hour at 50ªC. After this process, samples were washed with toluene, ethanol and water, then dried with nitrogen and incubated overnight in the oven 110ªC to crosslink the silane[2]

**Polyelectrolytes assembly**

For LBL deposition, the NAA substrates were immersed consecutively into solutions of poly(styrenesulfonate) (PSS, 1mg/ml in 20mM $CaCl_2$ in deionized water), deionized water, and poly(allyl amine) (PAH, 1mg/ml in 20mM $CaCl_2$ in deionized water). Dipping times in polyelectrolyte solutions were 30 min, the washing step in deionized water lasted for 10 min, and all the steps were repeated for 8 times.[3]

The morphologies of the NAA substrates and the polyelectrolytes layers were characterized by Environmental Scanning Electron Microscopy (ESEM). (Fig. 2) The initial porous measurements were 135 nm in diameter and 4µm in depth.

**Drug loading and release studies**

Positively charged doxorubicin hydrochloride (DOX) was selected as a model drug. 5 ml of DOX solution (1.0 mg/ml) at room temperature was adjusted to pH 2.0 with 0.1 M HCl. The suspension was stirred for 10 h in the dark with the samples immersed, followed by adjustment to pH 8.0 with 0.1 M NaOH and further stirring for 2 hours.[4]

Drug release was measured by drug photoluminescence. The photoluminescence measurements were taken on a fluorescence spectrophotometer from Photon Technology International Inc. (Birmingham, NJ, USA) with a Xe lamp used as the excitation light source at room temperature and an excitation wavelength ($\lambda ex$) of 480 nm.

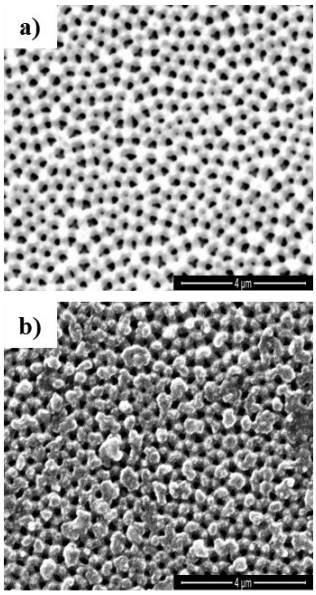


**Fig. 1. ESEM images of NAA substrates with (a)control surface without polyelectrolytes (b) NAA surface with polyelectrolytes**

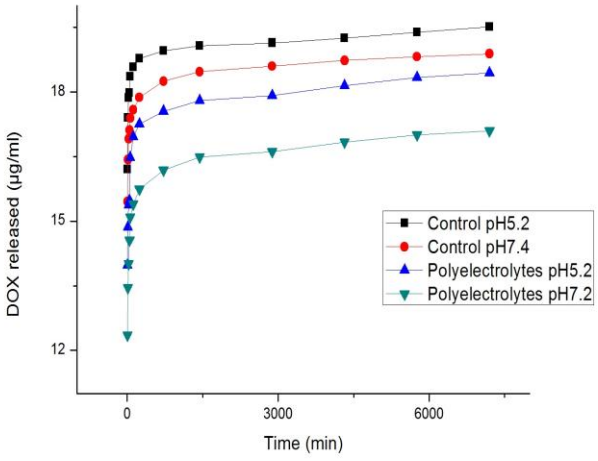


**Fig. 2. Photoluminescence release of DOX with PBS at different pH.**

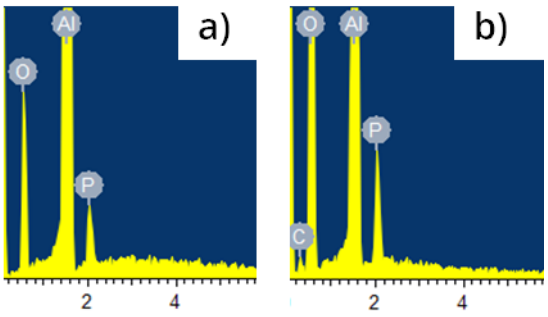


**Fig. 3 EDX measurements on the cuts of a bared sample (a) and a polyelectrolyte assembled sample (b).**

## 3. Conclusions

We achieved good polyelectrolyte deposition in NAA surfaces (Fig. 1). Retained drug releases have been observed in polyelectrolytes assembled samples at pH 5.2 (Fig. 2) We can assume that polyelectrolytes are introduced into the pores due to the EDX study (Fig. 3) in which can be appreciated the carbons in the cut of the polyelectrolytes assembled sample.


### Acknowledgements

This work was supported by the Spanish Ministry of Economy and competitiveness (MINECO) under grant number, TEC2012-34397 **by the ICREA under the ICREA Academia Award** and by Catalan authority under project AGAUR 2014 SGR 1344.


### References


[1] G. C. Schwartz and V. Platter, "An Anodic Process for Forming Planar Interconnection Metallization for Multilevel LSI," 1975.

[2] M. Baranowska, A. J. Slota, P. J. Eravuchira, G. Macias, E. Xifré-Pérez, J. Pallares, J. Ferré-Borrull, and L. F. Marsal, "Protein attachment to nanoporous anodic alumina for biotechnological applications: influence of pore size, protein size and functionalization path.," *Colloids Surf. B. Biointerfaces*, vol. 122, pp. 375–83, Oct. 2014.

[3] M. Raoufi, D. Tranchida, and H. Schönherr, "Pushing the size limits in the replication of nanopores in anodized aluminum oxide via the layer-by-layer deposition of polyelectrolytes.," *Langmuir*, vol. 28, no. 26, pp. 10091–6, Jul. 2012.

[4] Y. J. Yang, X. Tao, Q. Hou, Y. Ma, X. L. Chen, and J. F. Chen, "Mesoporous silica nanotubes coated with multilayered polyelectrolytes for pH-controlled drug release," *Acta Biomater.*, vol. 6, no. 8, pp. 3092–3100, 2010.

# Visualization of metabolic images of Langerhans islets by ultra-high resolution LDI - MS imaging using Au nanolayers

P. Ràfols[1,2], D. Vilalta[1,2] N. Ramírez[1,2], R. Calavia[3], O. Yanes[1,2], X. Correig[1,2], J. Brezmes[1,2]

[1]Metabolomics Platform, IISPV, Universitat Rovira i Virgili, Campus Sescelades, Carretera de Valls, s/n, 43007 Tarragona, Catalonia

[2]CIBERDEM, Spanish Biomedical Research Centre in Diabetes and Associated Metabolic Disorders, Bonanova 69, 6th floor, 08017 Barcelona, Catalonia

[3]MINOS-EMAS, Universitat Rovira i Virgili, Campus Sescelades, Carretera de Valls, s/n, 43007 Tarragona, Catalonia

## Abstract

Nowadays, mass spectrometry imaging (MSI) based on laser desorption/ionization have been widely used in the study of large molecules in-tissue distribution. However, classical MSI methods present some drawbacks when the low-molecular range must be studied. Moreover, the use of organic solvents in the sample preparation of classic MSI techniques limits the minimum achievable lateral resolution. To overcome these problems, we have developed a MSI method based on previous works in the field of metal nanoparticles as ionization means for MSI. We have applied our method to study the metabolite distribution in a rat pancreas tissue.

## 1. Introduction

Mass spectrometry imaging (MSI) allows the mapping of chemical compounds on a tissue section [1][2]. The most widely used ionization in MSI is Laser Desorption/Ionization (LDI), where tissue is scanned forming an image in which each pixel corresponds to a mass spectrum. Conventional LDI methods for MSI are based on spraying an organic matrix, reducing the effective lateral resolution and producing strong background noise inherent to the matrix in the low mass range [3].

Here, we obtained images from rat pancreas by means of a valuable matrix-free LDI based on the deposition of gold nanoparticles straight over the tissue. With the aim of identifying different functional parts of the tissue, multivariate analysis algorithms have been applied leading to the generation of molecular images.

## 2. Methods

Rat pancreas tissues were sliced into 10 μm sections using a cryostat and directly placed on indium tin oxide (ITO)-coated glass slides. Next, a 3 nm layer of gold nanoparticles was deposited over the tissue using a sputtering system running in RF mode. The MS spectra were acquired with a Bruker UltrafleXtreme MALDI-TOF instrument. The instrument has been adjusted with a raster step down to 10 μm, a total accumulation of 500 laser shots per pixel, a laser frequency of 2 kHz and a laser attenuation of 60%. After the acquisition, data was exported to XMASS format and converted to a custom format to perform data processing using in-house developed software, consisting in several preprocessing steps and image segmentation routines.

## 3. Preliminary Results

The method presented here, was able to acquire MS images in a wide low-mass range (< 1000 Da) exhibiting a negligible background signal from gold nanoparticles. Sputtering is a quick, flexible and easy to use deposition technique used to grow highly controlled homogeneous layers, needed for avoiding differences in ionization efficiency between pixels [4]. Further on, ultra-high lateral resolution (< 10 μm) is achieved, due to the absence of lateral compound diffusion. In order to quantify the lateral resolution, we have imaged some small regions of tissue using various raster sizes (from 10 to 100 μm) concluding that the limiting factor of resolution came from the instrumental laser focalization and not from the gold layer itself. Besides the good characteristics of our gold layer, another advantage is the reduced time of sample preparation, less than 15 minutes in contraposition of one hour long of conventional organic matrix deposition procedures.

In order to study the quality of the method, the MS image obtained from some pancreas of healthy and diabetic rats has been processed using several algorithms. First, images of some ions have been reconstructed and some spectra have been examined to evaluate the ionization efficiency (Figures 1,2 and 3). Second, an image of total ion count (TIC) was produced exhibiting an intensity variation uncorrelated with deposition method. After the application of the common preprocessing steps, several segmentation algorithms, like principal component analysis (PCA), have been used for clustering purposes, producing images where the Langerhans islets could be clearly differentiated from exocrine and adipose tissue regions as is presented in Figure 4. The ultra-high lateral resolution has been essential to study the molecular composition, as well as the density and distribution of Langerhans islets, making the Au nanolayer MSI a powerful tool for the study of diabetes.

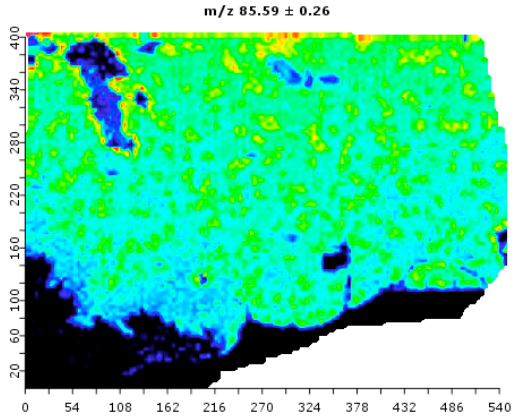


**Fig.1.** Distribution of molecules corresponding to 85.59 Da in a rat pancreas tissue section

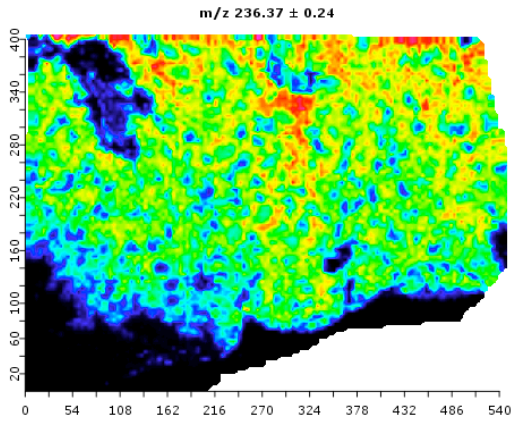


**Fig.2.** Distribution of molecules corresponding to 236.37 Da in a rat pancreas tissue section

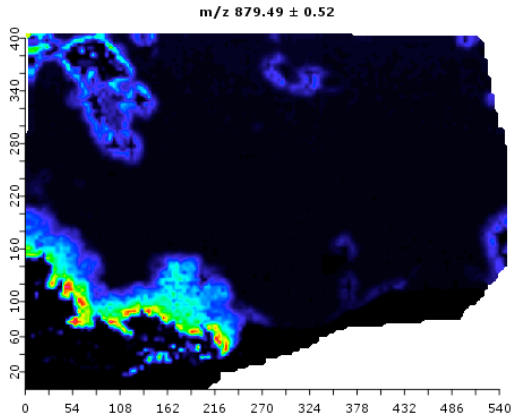


**Fig.3.** Distribution of molecules corresponding to 879.49 Da in a rat pancreas tissue section

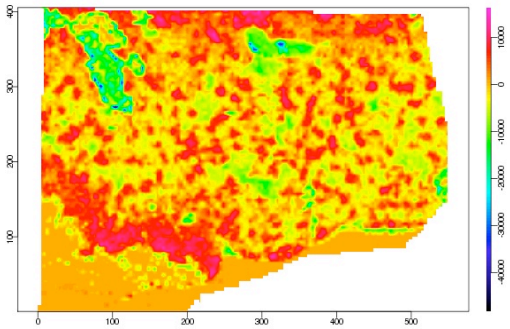


**Fig.4.** Auto image segmentation based on principal component analysis (PCA)

## 4. Conclusions

Sputtered Au based MS imaging has been demonstrated to be an ideal method for metabolite mass imaging. With our method is possible to achieve a high lateral resolution and negligible background noise. Furthermore, we obtained a new technique able to provide valuable information about the metabolite structure of Langerhans islets in pancreas tissue. We believe that such tools would result very useful in the study of diabetic diseases.

### References

[1] J. L. Norris and R. M. Caprioli, “Imaging mass spectrometry: a new tool for pathology in a molecular age.,” Proteomics. Clin. Appl., vol. 7, no. 11–12, pp. 733–8, Dec. 2013.

[2] S. Taira, Y. Sugiura, S. Moritake, S. Shimma, Y. Ichiyanagi, and M. Setou, “Nanoparticle-assisted laser desorption/ionization based mass imaging with cellular resolution.,” Anal. Chem., vol. 80, no. 12, pp. 4761–6, Jun. 2008.

[3] A. Svatos, “Mass spectrometric imaging of small molecules.,” Trends Biotechnol., vol. 28, no. 8, pp. 425–34, Aug. 2010.

[4] M. Dufresne, A. Thomas, J. Breault-Turcot, J.-F. Masson, and P. Chaurand, “Silver-assisted laser desorption ionization for high spatial resolution imaging mass spectrometry of olefins from thin tissue sections.,” Anal. Chem., vol. 85, no. 6, pp. 3318–24, Mar. 2013.

# Syntesis of new organic semiconductor as Hole Transporting Materials (HTM) in Perovskites Solar Cells

**Cristina R. Seco[a], Lydia Cabau[*,a] and Emilio Palomares[a,b].**

[a]*Institute of Chemical Research of Catalonia (ICIQ), Avinguda del Països Catalans 16, 43007 Tarragona, Spain. Fax: +34 977 920 823; Tel: +34 977 920 200; E-mail: lcabau@iciq.es*
[b]*Catalan Institution for Research and Advanced Studies (ICREA), Passeig de Lluis Companys 23, 08010 Barcelona, Spain.*

## Abstract

Lead halide perovskite solar cells (PSCs) have been attracted many interest because of its easy and low cost fabrication process, besides the fact of its high efficiency. However, the most efficient and used organic hole transporting material (HTM) is too expensive and not easy to sensitize: 2,2′7,7′-tetrakis-(N,N-di-p-methoxyphenyl-amine)-9,9′-spirobifluorene (spiro-OMeTAD). The aim of this thesis is the synthesis of new HTM with an easy synthesis and high efficiency in order to substitute the use of Spiro-OMeTAD. Here, are shown the synthesis of three new HTM for their application in PSCs (Scheme 1 and 2)


**Figure 1:** Schematic diagram of perovskite solar cell (PSC).

## 1. Introduction

Since 2012, when Henry Snaith and Michael Grätzel developed PSCs using $MAPbI_{3-x}Cl_x$ and $MAPBI_3$ as light absorber deposited onto a mesoporous $TiO_2$ layer and an HTM layer as extractor of photogenerated holes[1] (Figure 1); there has been many studies trying to increase the efficiency and trying to understand the process that happened in Them, improving the design changing the architecture, the use of different deposition techniques or with the synthesis of new HTM in order to improve the extraction of the holes to improve the efficiency of these devices.

The highest efficiency achieved up to now in PSCs is 21.0%, certified by Michael Grätzel in January of 2015[2].

## 2. HTM

The role of HTM in PSCs is to transport holes created in the perovskite and carry them to the electrode (Au). For this reason, the principal characteristics that have to present good HTM are: high hole mobility, good thermal and photochemical stability, energy levels (HOMO and LUMO) that fit with perovskite's, good photovoltaic parameters like large photocurrents, high open circuit voltage or fill factor and high solubility in common solvents among others[3]. Many HTM (organic and inorganic) have been developed for PSCs. There are three types of organic HTM: small molecules, conducting polymers and organometallic complexes. The aim of this thesis is the synthesis of new HTM for PPSCs and here is shown the synthesis of three new of them[1].

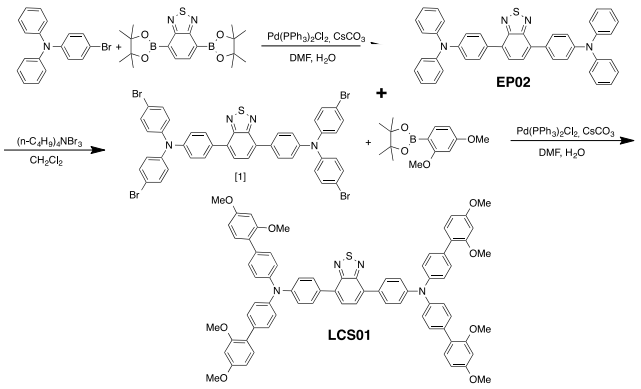


**Scheme 1:** Syntesis of EP02 and LCS01.

Nowadays, the most widely used HTM in PSCs is Spiro-OMeTAD, however its complex synthesis and low charge-carrier mobility make the development of new HTM with those qualities a priority[1].

There is a large number of HTMs published, like triphenylamine (TPA)-based, star-shape molecules, carbazole derivatives and hydrophobic oligothiophene among others[4]. Three new HTM have been done since March (when I started my PhD). All of them have a similar structure. **EP02** and **LCS01** are based on TPA with the difference of the introduction of a 1,3-dimethoxyphenyl in **LCS01**. With the synthesis of these three molecules we want to measure their efficiency in PSCs comparing with the Spiro-OMeTAD and compare between them how affect the different donor groups in the photovoltaic performance.

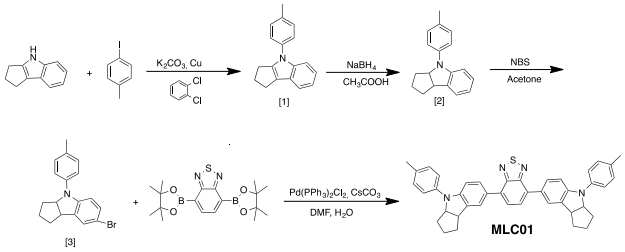


**Scheme 2:** Syntesis of **MLC01.**

## 3. Results and conclusion

In these three months, EP02, LCS01 and MLC01 have been synthetized. However, only EP02 has been characterized. In figure 2 $^{1}$H-NMR of EP02 is shown.

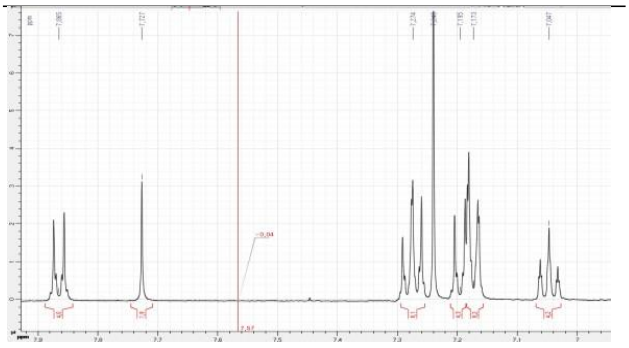

**Figure 2:** $^{1}$H-NMR of **EP02** in $CDCl_3$**.**

Before using these molecules in PSCs, it is needed to do a full charactrization doing $^{13}$C-NMR, Mass Spectroscopy Absorption, Emission, cyclic voltammetry and other measurements like, TGA and DSC.
Finally, if the energy levels fit well with perovskite's, we will perform and characterized solar cells. We expect a similar or higher efficiency comparing with Spiro-OMeTAD or, at least, like other molecules we have seen in the biography (10-15%).

## 4. References

[1] Ze Yu, Licheng Sun, "Recent Porgress on Hole-Transporting Materials for Emerging Organometal halide Perovskite Solar Cells", Adv. Energy Mater., 2015, 1500213.
[2] T.Swetha, S. P. Singh, "Perovskites solar cells based on small molecules hole transporting materials", J. Mater. Chem. A. DOI: 10.1039/C5TA02507A.
[3] Adv. Mater. 2008, 20, 1357-1362.
[4] O Miyata, N. Takeda et al., Tetrahedron, 2006, 62, 3629-3647.

# Synthesis of single crystalline $In_2O_3$ octahedra for detecting oxidizing and reducing gases at trace levels

Sergio Roso[1, 2], Atsushi Urakawa[2] and Eduard Llobet[1].

[1] Minos-Emas, universitat Rovira I Virgili, Av. Països Catalans 26, 43007, Tarragona, Spain
[2] Institute of Chemical Research of Catalonia (ICIQ), Av. Països Catalans 16, 43007, Tarragona, Spain

## Abstract

In the present work, single crystalline indium oxide octahedral ($In_2O_3$) with dimensions ranging from 300 to 500 nm have been synthesized via a vapor phase transport technique at high temperatures over $SiO_2$ substrates. Their composition, crystalline phase, morphology and gas sensing propertires are characterized. High responsiveness at low operating temperatures (e.g. at 100ºC) is reported.

## 1. Introduction

Semiconductor metal oxides have become a major technological drive in the field of gas sensors because of their low cost, high sensitivity, fast response and their relative simplicity. Among others, indium oxide ($In_2O_3$) is nowadays an interesting material for its unique optical and optoelectronic properties that make it suitable not only for gas sensors but also for solar cells and liquid-crystal displays. In this work, we develop a method to synthesize $In_2O_3$ octahedra and its sensing properties were examined, exhibiting great sensitivity great sensitivity towards low concentration of oxidizing and reducing gases.

## 2. Experimental

$In_2O_3$ octahedra are synthesized by a vapor phase transport method in a chemical vapor deposition (CVD) furnace. The precursor used was a powder of metallic In (99.99%), and Ar gas used as a carrier gas. Both, the precursor and the $Si/SiO_2$ substrates were placed onto a quartz boat into the horizontal CVD. Then, the temperature was raised to 900ºC and kept constant during 2 hours. All the process was carried out under atmospheric pressure. The deposited material was removed by scratching the material from the substrate. Then a printable ink was prepared by mixing it with appropriate solvents and the material was deposited by screen printing technique on top of a ceramic hotplate substrate with Pt electrodes on one side, and a heater on the other side. Gas mixing and delivery was performed employing a computer controlled mass flow system. The composition, crystalline phase and morphology of the octahedral were studied by X-ray diffraction, scanning electron microscopy and high resolution transmission electron microscopy. The gas sensing properties of this material at different operating temperatures were studied.

## 3. Results and Discussion

ESEM images of $In_2O_3$ octahedra synthesized over Si substrates are shown in Fig 1. Well defined octahedral with sharp edges were observed. These octahedral are very regular and almost perfect in shape with the size ranging from 300 to 500 nm. As we can see from Fig.1, every face of a single octahedron consists of an equilateral triangle. Furthermore, the surfaces are perfectly flat.

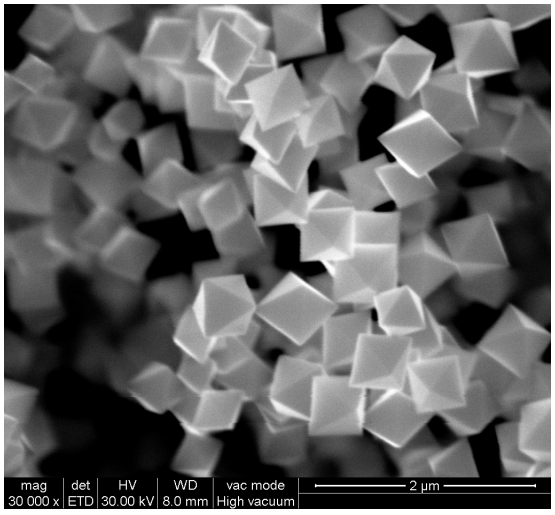


Fig 1. Image of the octahedral grown directly over Si/SiO2 substrates.

XRD studies of the samples show the presence if cubic $In_2O_3$. The strong emission from XRD measurements indicates a preferential orientation in the (111) direction. Moreover, these octahedral were subject to gas sensing tests using oxidizing ($NO_2$) and reducing ($H_2$) gases by means of DC resistance measurements at different operating temperatures (100-250ºC). The senots were

exposed to 15 minutes of a given concentration of a species, followed by 30 minutes of cleaning in dry air. All sensors experienced an increase or decrease in resistance under exposure to oxidizing gases, respectively. This implies that $In_2O_3$ behaves as an n-type of semiconductor.

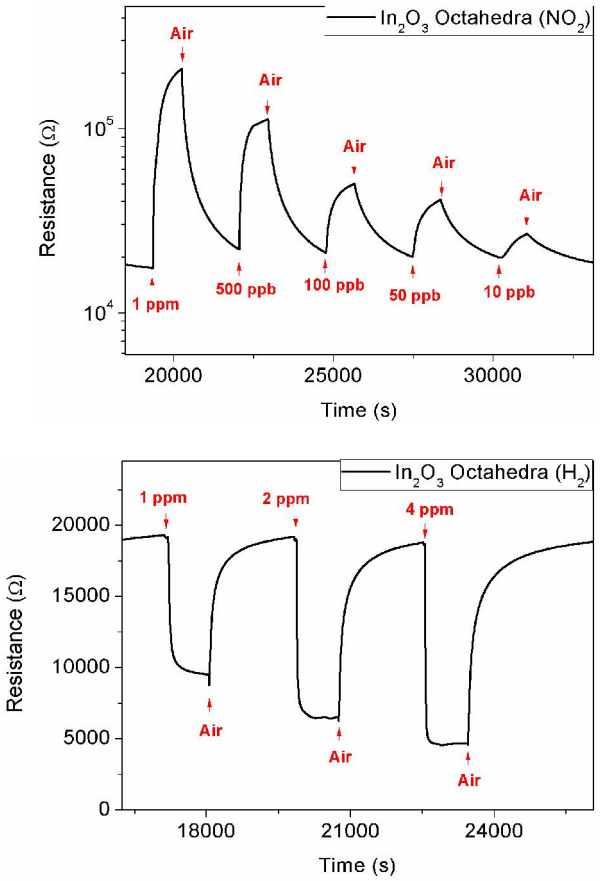


Fig 2. $In_2O_3$ octahedra exposed to: different concentrations of $NO_2$ at 100ºC (up) and different concentrations of $H_2$ at 250ºC (down).

The sensor using $In_2O_3$ octahedra showed an excellent response as well as very high sensitivity for both gases at very low concentrations and different temperatures. Fig 2 (up) shows the dependence of the sensor to different concentrations of $NO_2$ when operated at 100ºC. Fig 2 (down) shows the dependence of the sensor to different concentrations of $H_2$ when operated at 250ºC.

The optimum working conditions found for the $In_2O_3$ octahedra sensor to $NO_2$ were 130ºC whereas for $H_2$ sensing were 250ºC. This shows a clear change in the behaviour of the sensor. This could be due to two reasons: on the one hand, the morphology of the structures. These octahedra have very sharp edges, truncated tips and really smooth faces that might provide more active sites to interact with the $NO_2$ molecules more than to $H_2$ molecules. On the other hand, the octahedral posses unique (111) crystal facets exposed to the gas. These family of planes might favour the reaction with $NO_2$ molecules rather than with $H_2$ molecules.

## 4. Conclusions

To sum up, we have synthesized $In_2O_3$ octahedra via a vapor phase transport method at high temperatures. We have studied the morphology of these octahedral by means of ESEM and TEM and we have found out that the structures are single crystal. Finally we have tested the $In_2O_3$ octahedra against two kinds of gases such as an oxidizing gas ($NO_2$) and a reducing gas ($H_2$). The responses for each gas were excellent achieving the detection of very low concentrations of each gas at low operating temperatures. Finally, we have observed a change in the behavior of the sensor for each gas.

# Inverted Bulk Heterojunction Organic Solar Cell Based on PTB7:$PC_{70}BM$ with a Titanium Oxide as Electron Transport Layer

J.G. Sánchez[a], V.S. Balderrama[a,b], M. Estrada[b], J. Ferré-Borrull[a], L.F. Marsal[a] and J. Pallarès[a]*

[a]Departament d'Enginyeria Electrònica, Elèctrica i Automàtica, Universitat Rovira i Virgili, Avda. Països Catalans 26, 43007 Tarragona, Spain.
[b]Sección de Electrónica del Estado Sólido, Depto. Ingeniería Eléctrica, CINVESTAV-IPN, Av. IPN No 2508, C.P. 07360, D.F., México
*Corresponding author e-mail: josep.pallares@urv.cat, Phone. +34 977 559 625, Fax: +34 977 559 605.

## Abstract

For the first time in our lab, inverted bulk-heterojunction organic solar cell (*OSC*) was fabricated with Titanium oxide ($TiO_x$) as electron transport layer in order to analyze its effects on the power conversion efficiency. $TiO_x$ layer was deposited by spin coating from a solution of titanium oxide sol using titanium isopropoxide as precursor. The blend of thieno[3,4-b]-thiophene/benzodithiophene (*PTB7*) and [6,6]-phenyl-C70-butyric acid methyl ester ($PC_{70}BM$) was used as the photoactive layer. The inverted OSC structure was ITO (120 nm) / $TiO_x$ (~58 nm) / PTB7:$PC_{71}BM$ (~200 nm) / $V_2O_5$ (5 nm) / Ag (100 nm). Furthermore, in order to compare the performance parameters, we fabricated a standard OSC with the structure ITO(120 nm)/PEDOT:PSS(40 nm)/PTB7:$PC_{70}BM$(~200 nm)/ Ca(25 nm)/Ag (100 nm). The performances parameters for standard and inverted OSC were $V_{OC}$= 710 and 670 mV; $J_{SC}$= 14.7 and 14.9 mA/cm$^2$; FF= 0.71 and 0.63 and PCE= 7.3 and 6.3 % respectively.

## 1. Introduction

In standard OSC, calcium (*Ca*) and poly(3,4-ethylene dioxythiophene):poly-(styrenesulfonate) (*PEDOT:PSS*) are commonly used as a low-work function metal electrode and hole transport layers, respectively. However, it is well known that the highly reactivity of calcium with the water and oxygen as well as the hygroscopicity and acidic nature of PEDOT:PSS in ambient conditions can lead degradation of the active layer and the indium tin oxide (*ITO*) electrode [1]. In order to reduce these problems, inverted OSC have been developed replacing Ca by transition metal oxides (*TMOs*) because they confer low-resistance ohmic contacts. Among them, molybdenum oxide ($MoO_3$), vanadium oxide ($V_2O_5$) or tungsten oxide ($WO_3$) [2]. On the other hand, PEDOT:PSS is replaced for $TiO_x$ or Zinc oxide (ZnO) as ETL because of their good transparency as thin films and the possibility to be deposited by low temperature solution where power conversion efficiency (*PCE*) has been reported of 6.7% [3-4].

## 2. Experimental and Discussion

Figure 1 shows the standard and inverted OSC structures that were made in this work. We use the sol-gel method for preparing the sol of titanium oxide [5]. The starting materials were IV titanium isopropoxide (2 mL), 2-methoxyethanol (10 mL), ethanolamine (1 mL). Materials were mixed in a hermetically sealed recipient under inert ambient (nitrogen). The mixture was stirred during 3 h at 120 ºC. Afterwards, a dilution of the $TiO_x$ sol in anhydrous methanol with the ratio 1:5 (v/v) was prepared, and deposited to get a layer lower than 58 nm of thickness [6]. The active blend of PTB7 and $PC_{70}BM$ at ratio 1:1.5 (w/w) was prepared under $N_2$ atmosphere and mixed in a bottle using the chlorobenzene as solvent to obtain a final concentration of 25 mg mL$^{-1}$. The blend solution was left stirring for 18 h and after it was left for 48 h to age. For standard OSC PEDOT:PSS was deposited on top of the cleaned ITO by spin-coating at 4500 rpm and was applied the annealing of 120 °C during 20 min. Afterwards, the PTB7:$PC_{70}BM$ solution was deposited on the previous PEDOT:PSS layer by spin-coating at 800 rpm for 30 s. Finally, the samples were transferred to a vacuum chamber, where 25 nm of Ca and 100 nm of Ag were thermally evaporated on the photoactive. In the inverted OSC, the $TiO_x$ was deposited on top of the ITO by spin-coating at 5000 rpm and after the samples were left for 1 h in atmosphere air. The next step was applied the annealing from 20 °C to 400 °C with a ratio of 20 °C min$^{-1}$. The active layer was deposited under the same conditions as was described above. Finally, $V_2O_5$ (5 nm) and Ag (100 nm) were deposited by evaporation at 6 X 10$^{-7}$ mbar on the active layers. The active area in both structures was 9 mm$^2$. Figure 2 shows the *J–V* curves under illumination at 1 sun (AM 1.5G spectrum) of the two structures manufactured. Figure 3 shows the *J–V* curves under darkness for both

structures. The reverse voltage region is almost the same in both cases, while that, in the forward voltage region there are clear differences in the low and middle region (0.25-0.65 V). Table 1 shows the performance parameters for the standard and inverted OSC structures. The standard OSC has $V_{OC}$, FF and PCE higher than inverted OSC, but the $J_{SC}$ is practically the same in both structures. Series and shunt resistances in standard OSC are better than in inverted OSC.

## 3. Conclusions

For the first time inverted OSC where fabricate with the structure ITO/$TiO_x$/PTB7:$PC_{70}BM$/$V_2O_5$/Ag in our lab. Standard OSC shows better values of $V_{OC}$, PCE, series and shunt resistance than inverted OSC. The high series resistance and the low shunt resistance in inverted organic solar cells damage the fill factor and decreasing the PCE. On the other hand, the $J_{SC}$ values for both structures were similar between of them. We assume that the thickness of $TiO_x$ is not optimum and this causes the increase of the series resistance of the photovoltaic device.

## 4. Future works

The thickness of $TiO_x$ must to be thinner, therefore, the dilution of the solution have to be greater. In order to improve the electron transport layer for the $TiO_x$ one alternative is to make a doping of impurities using the transition metals during the sol preparation.

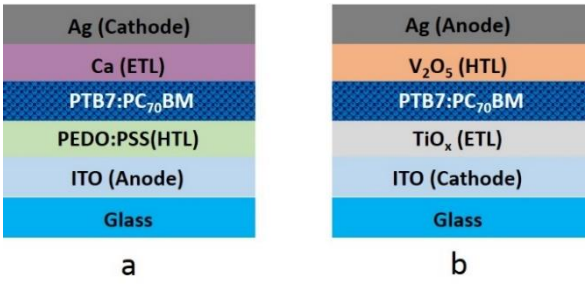


**Figure 1.** a) Standard and b) inverted organic solar cells.

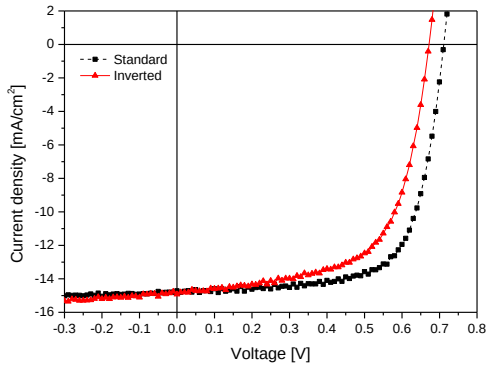


**Figure 2.** Current density – Voltage characteristic of the standard and inverted OSC structures measured at 1 sun.

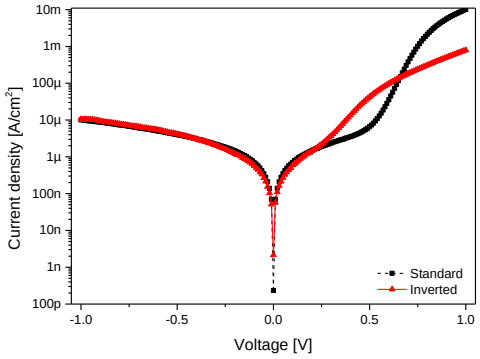


**Figure 3.** Current density – Voltage characteristics under darkness for both structures manufactured.

**Table 1.** Performance parameters for the cells.

| | $V_{OC}$ [mV] | $J_{SC}$ [mA/cm$^2$] | FF | PCE [%] | $R_{S\,LG}$ [Ω-cm$^2$] | $R_{SH\,LG}$ [Ω-cm$^2$] |
|---|---|---|---|---|---|---|
| Std | 710 | 14.7 | 0.71 | 7.35 | 1.6 | 904 |
| Inv | 670 | 14.9 | 0.63 | 6.31 | 2.04 | 588 |


## Acknowledgements

This work was supported by the Spanish Ministry of Economy and competitiveness (MINECO) under grant number, TEC2012-34397 by the ICREA under the ICREA Academia Award and by Catalan authority under project AGAUR 2014 SGR 1344 and CONACYT Project 237213 in Mexico.


**References**


[1] K Norrman, "Degradation Patterns in Water and Oxygen of an Inverted Polymer Solar Cell", *Chem. Soc*., 132, 16883, 2010

[2] Z. B. Wang, "Analysis of charge-injection characteristics at electrode-organic interfaces: Case study of transition-metal oxides", *Phys. Rev. B: Condens. Matter Mater. Phys.*, 80, 235325, 2009.

[3] M. Thambidurai, "Enhanced power conversion efficiency of inverted organic solar cells by using solution processed Sn-doped TiO2 as an electron transport layer", *J. Mater. Chem. A*, 2, 11426, 2014.

[4] B. R. Lee, "Amine-Based Polar Solvent Treatment for Highly Efficient Inverted Polymer Solar Cells", *Adv. Mater.*, 26, 494–500, 2014.

[5] S.H. Kim, "Efficiency enhancement in polymer optoelectronic devices by introducing titanium sub-oxide layer," *Current Applied Physics*, vol. 10 pp. S528–S531, 2010.

[6] J.G. Sanchez, "Preparation, Deposition and Characterization of TiOx Layers for Organic PLEDs, Solar Cells and PTFTs", *8th International Conference on Electrical Engineering Computing Science and Automatic Control (CCE)2011*, pp. 1-4, 00110.1109/ICEE.2011. 6106675, 2011.

# The effect of PDMS nano- and microstructures on preadipocytes adhesion and morphology

Agata J. Słota[a], K. Roche Rodríguez[b], Małgorzata Baranowska[a], Pinkie J. Eravuchira[a], Pilar Formentín[a], Sonia Fernández-Veledo[b], Joan J. Vendrell Ortega[b], Lluís F. Marsal[a],*

[a] Departament d'Enginyeria Electrònica, Elèctrica i Automàtica, Universitat Rovira i Virgili, Avda. Països Catalans 26, 43007 Tarragona, Spain, * lluis.marsal@urv.cat

[b] Hospital Universitari Joan XIII, Institut d'Investigació Sanitària Pere Virgili, C/ Dr. Mallafrè Guasch 4, 43005 Tarragona, Spain

## Abstract

We studied the effects of polydimethylsiloxane (PDMS) nano- and microstructures on the behavior of human preadipocytes. Double-layer patterned stamps composed of high and low elastic modulus PDMS ("hard" and "soft" PDMS) were fabricated by replica molding technique using nanoporous anodic alumina and silicon templates. PDMS nanopillars, micropillars and micro-pyramids were used as cell culture substrates to analyze cell responses to different topographies and to determine how the size and the shape of the surface patterns influences cell adhesion, morphology and spreading.

## 1. Introduction

Specific functions of cells within living tissue are modulated by their interactions with the surrounding microenvironment. Contact with other cells and with the extracellular matrix (ECM) components provides a cell with chemical and physical signals which can activate specific receptors in the cell's membrane and trigger biochemical responses inside the cell. This process leads to changes in cell behavior, including adhesion, migration, proliferation, differentiation and apoptosis [1]. Studying the interactions between cells and surfaces may be extremely valuable to understand mechanisms of various physiological and pathological processes. It can also help to develop new methods of disease diagnosis and treatment. In order to analyze cellular activity under physiological-like conditions, materials with nano- and micropatterned surfaces imitating natural tissue environment are used as cell culture substrates [2]. In recent years many research works have analyzed the influence of these engineered materials on cells behavior and their results have shown that surface topography and surface chemical composition have significant effects on cell morphology, orientation, migration, proliferation or even gene expression and differentiation [3, 4]. Cellular responses however were found to be strongly dependent on the cell type and on the patterned surface characteristics, such as feature size, shape, ordering, surface wettability or substrate stiffness [5, 6]. Although some tendencies in cell responses to substrate topography have been observed, predicting specific cellular behaviors on different surfaces can be still difficult and requires further investigation.

## 2. Experimental

The fabrication of PDMS double-layer patterned substrates was previously described in [7]. To improve surface compatibility of PDMS for cell culture, all the substrates were modified with collagen type I. Human preadipocytes were seeded on the PDMS nanopillar, micropillar and micro-pyramid surfaces. Cells on flat (non-patterned) PDMS substrate and on the glass slide were used as a control. Cells were incubated in culture medium for 5h or 72h, then fixed with paraformaldehyde, stained with Acti-stain 670 phalloidin (for F-actin) and NucGreen 488 (for nucleus) and observed in fluorescence microscope (Nikon Eclipse TE2000-E). Other set of cells was fixed with glutaraldehyde and $OsO_4$, dried with ethanol and observed in electron scanning microscope (ESEM FEI Quanta 600).

## 3. Results

Significant differences in the morphology and spreading of the cells growing on different surfaces can be found. The morphology of preadipocytes cultured on non-patterned PDMS substrates appear to be similar to that of the cells growing on a glass slide, although the initial attachment and spreading of cells on the flat PDMS is slightly better than on the glass surface. Preadipocytes incubated for 5 hours on the non-patterned PDMS substrate (Fig. 1c) look more flat and show well-developed membrane protrusions, whereas many of the cells growing on the glass surface still have a spherical shape or just begin to spread (Fig. 1a). After one day of incubation, cells are spread out well on both types of surfaces and exhibit flattened fibroblast-like morphology (Fig. 1b, d). After 72 hours of culture, a confluent monolayer of cells covers the whole area of both substrates.

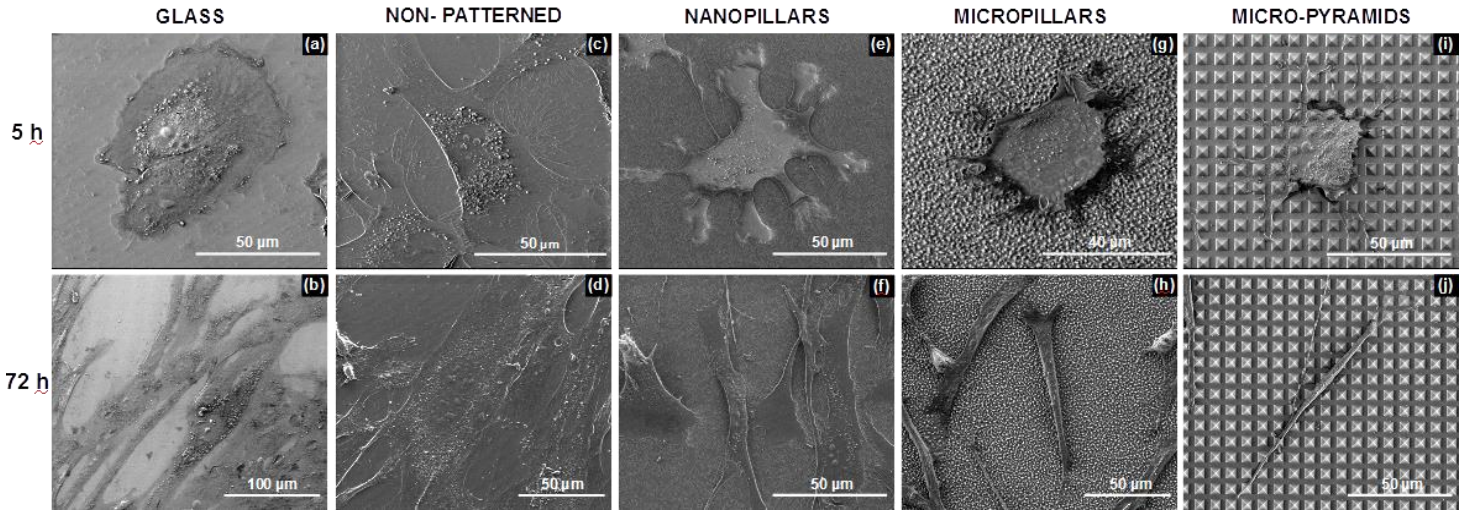


**Fig. 1** Morphology of human preadipocytes after 5 hours (upper row) and 72 hours (bottom row) of incubation on glass substrate (a, b) and PDMS non-patterned (c, d), nanopillar (e, f), micropillar (g, f) and micro-pyramid (i, j) substrates.

In the case of nanopillars (240 nm high, 310-340 nm in diameter, 450 nm of inter-pillar distance), cells incubated for 5 hours appear flattened with mostly circular shape and well-developed lamellipodial protrusions extending in all directions from the cell body (Fig. 1e). With increasing incubation time cell morphology changes into more elongated and large flattened lamellipodia can be seen at the cell's ends (Fig. 1f). Comparing to flat substrates, preadipocytes cultured for 72 h on nanopillars surface form less uniform and more branched network of cells with densely packed cell clusters located on the sample borders.

On the micropillar surface (1.5-1.8 µm high, 1-1.5 µm in diameter, disordered) small, not very well spread cells with short membrane protrusions are found after 5 hours of incubation (Fig. 1g). Over the time of culture, cells gradually elongate and become narrower. The spreading area of an individual cell appears to be more limited than in the case of the nanopillar substrate (Fig. 1h).

The most noticeable changes in cellular morphology are found in preadipocytes seeded on the micropyramid surface (lateral size of 5 µm, 3.8 µm high, inter-pyramid distance of 8 µm). Initially, the cells are small and seem to adapt their geometry to the underlying substrate pattern, which results in more orthogonal than circular shapes (Fig. 1i). Short filopodial protrusions at the cell periphery extend and adhere to the nearest micropyramids. After 72 hours of incubation, pronounced elongation and narrowing of the cell body can be seen (Fig. 1j). Cells are spindle-shaped and sit on the top of the pyramids rather than spread out over the surface. Flattened lamellipodia at the distal ends are poorly extended. Small membrane protrusions are formed along the cell body, allowing the cell to adhere to the micropyramid walls. Although the cells are distributed uniformly over the entire substrate, they do not form a confluent layer but stay separated and have very limited contact with other cells.

## 4. Conclusions

The results of our study demonstrate that human preadipocytes strongly respond to substrate topography and that the changes in their morphology and spreading depend on the size of the surface pattern. Future work is planned in order to determine whether and how those morphological changes affect cell proliferation, differentiation and other functions.

## Acknowledgements

This work was supported by the Spanish Ministry of Economy and Competitiveness (MINECO) under grant number TEC2012-34397 and by Catalan Government under project AGAUR 2014-SGR-1344.

**Supporting information**

Fluorescence images of cells and ESEM images of PDMS structures could not be included due to the lack of space. They are available on request (see contact information).

**References**

[1] B. Geiger, A. Bershadsky, R. Pankov, K.M. Yamada, Nat. Rev. Mol. Cell Biol. 2 (2001) 793-805.

[2] A.M. Ross, J. Lahann, . Polym. Sci. Part B Polym. Phys. 2013 (51) 775–794.

[3] C.Y. Tay, S.A. Irvine, F.Y.C. Boey, L.P. Tan, S. Venkatraman, Small 2011 (7) 1361–1378.

[4] H.J. Jeon, C.G. Simon Jr, G.H. Kim, J. Biomed. Mater. Res. Part B Appl. Biomater. 2014 (102) 1580–1594.

[5] X. Yao, R. Peng, J. Ding, . Mater. 2013 (25) 5257–5286.

[6] N.M. Alves, I. Pashkuleva, R.L. Reis, J.F. Mano, Small 2010 (6) 2208–2220.

[7] A. Slota, M. Baranowska, P. Jacob, P. Formentín, L.F. Marsal, Graduate Students Meeting on Electronics Engineering, Tarragona 19-20 June 2014, Book of abstracts, 65 –66.

# Fabrication and optimization of rugate filters based on Nanoporous Anodic Alumina

Alejandro Velando Crespo, Gerard Macias, Josep Ferré-Borrull, Lluís Marsal

Department of Electronic, Electric and Automatics Engenieering, Universitat Rovira I Virgili, Avda, Països Catalans 26, Tarragona 43007, Spain. (34) 977 55 86 53. alejandro.velando@urv.cat

## Abstract

A rugate filter is a kind of interference filter characterized by a continuous sinusoidal index variation in the direction perpendicular to the film plane. It shows a high reflectivity 'stop band' in a specific range of wavelength. Rugate filter based on nanoporous anodic alumina was fabricated using sinusoidal current profile with small current variation. The resulting structure consisted of highly parallel pores with modulations of the pore diameter along the pore axis. The effect of changing the period time (T), current ($I_0$) and amplitude (A) parameters was studied. From reflectance measurements, it was seen that the position of the reflection band or peak ($\lambda_0$) can be tuned by adjusting this parameters. This method allows the fabrication of complex in-depth modulated nanoporous anodic alumina structures in order to get multiple reflectivity peaks in the visible spectra range, that open up the possibility of new kinds of alumina-based optical sensing devices

## 1. Introduction

Rugate filters are one-dimensional photonic crystals based on a smooth variation of the refractive index along the depth of the structure which results in a photonic bandgap (PGB). Unlike distributed Bragg reflectors (DBR), rugate filters display a single reflectivity band without harmonic or sidelobes. Thanks to this feature, rugate filters with complex optical response and multiple PGB can be fabricated by superposing multiple refractive index profiles [1]. However, these filters are difficult to fabricate because the smooth variation of the refractive index is challenging and requires complex equipment. An interesting method for fabricating rugate filters is by means of electrochemically etched materials such as nanoporous anodic alumina (NAA) [2]. NAA is a nanostructured material obtained from the electrochemical etching of high-purity aluminum foils. NAA consist of highly uniform and parallel pores with no branching. The interpore distance can be easily tuned by adjusting the voltage applied during the electrochemical etching conditions [3], also the pore diameter can be adjusted by wet chemical etching with phosphoric acid.

One of the techniques used for pore modulation during the anodization is cyclic anodization. This method was used to fabricate DBRs by applying a periodic voltage which resulted in well-defined layers with branched pores [4].

In this work, we report a current control technique for the fabrication of NAA rugate filters, modulating several parameters, current ($I_0$), amplitude (A), period time (T). We have characterized the resulting structure and analyzed its optical response comparing the spectral reflectivity peaks in the uv-visible range of $\lambda_0$ (200-800nm), resulting from changing the parameters of the anodization conditions. Finally we show the shift of the central wavelength position as function of the changes in anodization parameters.

## 2. Materials and methods

Aluminum (Al) foil (thickness = 250µm, purity = 99,99%) was purchased from Goodfellow (Huntingdon, UK). Oxalic acid, ethanol, perchloric acid and hydrochloric acid were purchased from Sigma-Aldrich (Madrid, Spain). Double deionized (DI) water (18.6 MΩ, Purelab Option-Q, Elga, Marlow, UK) was used for used for all the solutions unless otherwise specified.

Al substances were first further cleaned with ethanol (EtOH) and DI water and dried under a stream of air. Prior to anodization, all substrates were electropolished in a mixture of EtOH and perchloric acid ($HClO_4$) 4:1 (v/v) at 20 V and $5^0$C for 6 min. During the electropoolishing procedure, the stirring direction was alternated every 60 seconds. Subsequently, the anodization of the aluminum in $H_2C_2O_4$ 0.3M at $5^0$C was carried out by applying a non apodizing current profile consisting on a DC component of 2.0 mA $cm^{-2}$ with a superimposed alternating current (AC) sinusoidal component with variable amplitude (see fig 1). The amplitude (A) and the average current ($I_0$) were modulated.

We investigated the influence of period (T), $I_0$, and A modifications of the sinusoidal component on the optical characteristics of the obtained structures (reflectance bands of the NAA rugate filters).

## 3. Results

Figure1 shows the characteristic current and voltage evolution during the fabrication of NAA rugate filters. In this approach, we performance the current and voltage profiles, modulating the period (T), current($I_0$), and Amplitude (A) parameters in order to minimize the sidelobes and get a maximum reflectance peak as high as possible in the reflectance spectra. We observed how the current density profile used throughout the experiments resulted in an initial transitory voltage that reach values of 60 volts when we increase the current in 1 or 2 mA respectively (Figure1), which corresponds to the growth of the NAA barrier layer at the bottom of the pores, followed by a sinusoidal voltage profile oscillating between 45 and 55 volts with an average value of 50V that resembles the applied current profile. A look at the electrochemical fabrication curves reveals a delay of the voltage with respect to the current.

In order to calibrate the position of the maximum reflectance peak ($\lambda_0$), we fabricated in a first stage, three samples with periods of T = 150,200,250s and in a second stage three sets of samples with a current $I_0$= 3,4,5mA for each period (T) (see Figs 2,3). Consequently by increasing the period time, we increased the time of the period of the pore diameter variations and, thus, tuned the position of the $\lambda_0$ reflectance peak to long wavelengths, also increasing this parameter (T) we reduce the oscillations registered in the profiles of the reflectance spectra. By increasing the average current ($I_0$) shifts the reflectance peak ($\lambda_0$), towards short wavelengths and makes higher this peak or reflectance band.

## 4. Conclusions

A rugate filter is a kind of interference filter and it shows a high reflectivity 'stop band' in a specific range of wavelength. NAA rugate filters were fabricated using a current control method based on a sinusoidal current profile with a maximum amplitude of just 2 mA $cm^{-2}$ and a voltage profile contained within 50 +/- 5 V. In order to see how shifts the position of the maximum reflectance peak along the wavelength spectra we have varying several parameters during its fabrication process like Period (T), amplitude(A) and average current ($I_0$). Therefore, the position of the peak wavelength can be accurately tuned by modulating the period time and the average current ($I_0$). Another important point is that the height of this peak ($\lambda_0$) enhances when we decrease the period (T) and also increasing the average current ($I_0$) in rugate filters fabrication. This process allows the fabrication of highly reflective peaks with just 50 periods. Moreover, for as-produced rugate filters, the reflectance peaks were narrow (less than 30 nm) which is an important feature, apart from the aforementioned for the development of highly chemical and biochemical sensors based the monitorization of the position of the reflectance peak.

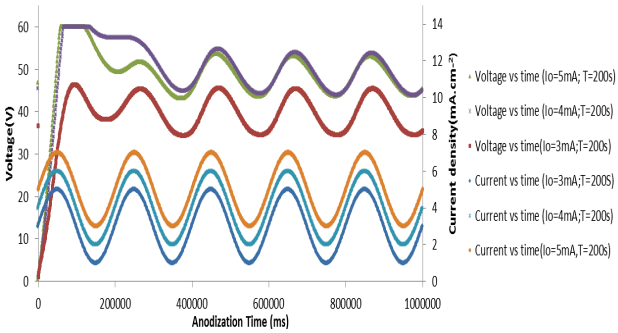


**Fig.1.** Characteristic current and voltage evolution during the fabrication of NAA rugate filters.

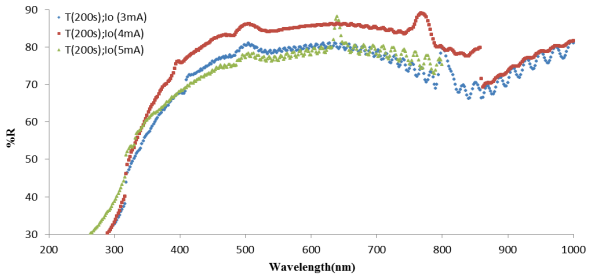


**Fig.2.** Reflectance spectra of NAA rugate filters anodized with a period of T=200s and a Io=3,4 and 5 mA for 50cycles.

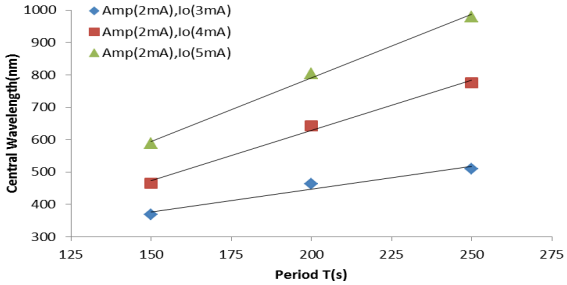


**Fig.3.** Central Wavelength λ0 position of the reflectance peak as function of Period time (T).

**References**.

[1] Bovard BG, "Rugate filter theory: an overview", Appl Opt, 32. 5427-5442. 1993.

[2] Kumeria T., "Structural and optical nanoengineering of nanoporous anodic alumina rugate filters for real-time and label-free biosensing applications", Anal Chem, 86. 1-2. 2014.

[3] Berger M.G., "Dielectric filters made of PS: advanced performance by oxidation and new layer structures". Thin Solid Films, 207. 237-240. 1997.

[4] Rahman M. M., "Tuning the photonic stop bands of nanoporous anodic alumina-based distributed brag reflectors by pore widening", ACS Appl Mater Interfaces, 5. 13375-13381. 2013.

# NEW $WO_3$ SOLID–STATE SURFACES FOR LASER DESORPTION/IONIZATION MASS SPECTROMETRY FOR HIGH THROUGHPUT METABOLOMICS

**D. Vilalta[1,2], N. Ramírez[1,2], R. Calavia[3], P. Ràfols[1,2], M. Vinaixa[1,2], O. Yanes[1,2], X. Correig[1,2]**

[1]Metabolomics Platform, IISPV, Universitat Rovira i Virgili, Campus Sescelades, Carretera de Valls, s/n, 43007 Tarragona, Catalonia

[2]CIBERDEM, Spanish Biomedical Research Centre in Diabetes and Associated Metabolic Disorders, Bonanova 69, 6th floor, 08017 Barcelona, Catalonia

[3]MINOS-EMAS, Universitat Rovira i Virgili, Campus Sescelades, Carretera de Valls, s/n, 43007 Tarragona, Catalonia

## Abstract

MALDI-MS is a technique commonly used in proteomics, but limited in metabolomics due to the presence of interference peaks in the low mass range (<1000 Da) inherent to the organic matrices needed for the correct compound ionization. To overcome this, different solid-state substrates have developed in the last years, such as NIMS (Nanostructure Initiator Mass Spectrometry).

In this study, we have developed and characterized three different solid-state substrates based on $WO_3$: two kinds of $WO_3$ surfaces and one NIMS modified with $WO_3$ nanoparticles. Performance of the surfaces has been tested with mixtures of 20 metabolites standards and in urines from a biological study. Results have been compared with those obtained with a standard NIMS surface.

## 1. Introduction

Matrix Assisted Laser desorption/ionization mass spectrometry (MALDI-MS) is commonly used in proteomics because of the easy sample preparation, and fast analysis. However, the applicability of this technique in metabolomics is limited due to the presence of interference peaks in the low mass range (<1000 Da) inherent to the organic matrices needed for compound ionization [1]. To overcome this, in the recent years solid-state surfaces have been introduced for LDI-MS metabolomics applications that allow the ionization of a wide mass range of metabolites with reduced background noise. One of this surfaces is NIMS (Nanostructure Initiator Mass Spectrometry) [2], based on a layer of porous silicon etched with hydrofluoric acid.

Here, we introduce $WO_3$-based surfaces as a valuable alternative for LDI-MS metabolomics applications. Performance of the $WO_3$-surfaces was tested in a biological study consisting in the analysis of urine from rats before and after 3,4-Metilendioximetamfetamina (MDMA) administration.

## 2. Methods

Three different $WO_3$-based surfaces were fabricated for this study: two kinds of anodized layers of $WO_3$ on silicon, one just anodized with tartaric acid by 100 seconds ($WO_3$) [3] and another anodized with tartaric and a layer of bis(heptadecafluoro-1,1,2,2-tetrahydrodecyl)tetramethylsiloxane ($WO_3$-BisF17). We have also functionalized a NIMS with $WO_3$ nanoparticles (NIMS-$WO_3$) deposited by sputtering with the aim to explore the possible changes in NIMS properties when functionalized with $WO_3$ nanoparticles. As a reference, we have compared the performance of these $WO_3$ surfaces with a standard NIMS.

The performance of the surfaces was checked using 20 standard compounds (from m/z 90 to 800) of common endogen metabolites, including amino acid and short chain acids. As example of the performance in biological studies, urines from rats treated with 3,4-Metilendioximetamfetamina (MDMA) were also analyzed with these surfaces. The MS spectra were acquired with a Bruker UltrafleXtreme MALDI-TOF instrument, between 1 and 1000 Da with a Nd-YAG laser at 355 nm and 500 Hz in positive reflection mode. The main analytical parameters (i.e. laser intensity, attenuation and shots) were optimized for each surface.

## 3. Preliminary Results

As commented above, background noise in the low mass range is one of the main limitations for the applicability of LDI-MS in metabolomics. Fig. 1 shows the background noise of the studied surfaces. As it can be seen, the $WO_3$ surfaces developed in this study presented significantly less peaks with lower intensities

than those found in the reference surface (NIMS). In this respect, $WO_3$-BisF17 and NIMS-$WO_3$ presented less than 120 background peaks under 1000 Da with median intensities under 200 a.u. whereas NIMS showed more than 500 peaks in the same region with 1000 a.u. median intensities. It is worth mentioning that the functionalization of NIMS with $WO_3$ nanoparticles drastically reduces the NIMS background noise.

Regarding the performance of the surfaces with the metabolites standards, NIMS-$WO_3$ and $WO_3$-BisF17 were able to detect all 7 lipids, being more intense in the NIMS-$WO_3$, showed in Fig 2. The performance of the surfaces with most of the polar standards was similar in all surfaces, with average intensities between 1,000 and 100,000 a.u. (see Fig. 3).

The biological study was conducted by analyzing the urine from 12 rats treated with MDMA. Prior to the LDI-MS analysis, urines were just diluted to a factor of 1:10. All the studied surfaces showed peaks inherent to the urine samples, including creatinine. The changes in the urine metabolome were determined by comparing the basal urine with the rat urine 24 hours after the intervention, finding statistical significant differences before and after the treatment for all surfaces. Fig. 4 shows the Principal Component Analysis (PCA) between the two classes (Before (Red) and after 24h (Blue) of the MDMA administration) using the $WO_3$-BisF17 surface which demonstrates the suitability of these surfaces on biological studies.

## 4. Conclusions

We have demonstrated the high performance of the $WO_3$ developed surfaces for LDI-MS metabolomics. These surfaces present much lower background noise in the low mass range area when compared with a standard NIMS surface. The functionalization of NIMS with $WO_3$ nanoparticles, not only reduces background noise, but also enhances its properties as LDI-MS material. NIMS-$WO_3$ performed better for lipid compounds, but the performance with polar metabolites was comparable in all surfaces. The applicability of the developed surfaces in biological studies has been also proved.

## 5. References


[1] S. Identifi-, "Laser Desorption Ionization of Proteins with Molecular Masses Exceeding 10000 Daltons," vol. 2301, no. 29, pp. 2299–2301, 1988.

[2] H.-K. Woo, T. R. Northen, O. Yanes, and G. Siuzdak, "Nanostructure-initiator mass spectrometry: a protocol for preparing and applying NIMS surfaces for high-sensitivity mass analysis.," *Nat. Protoc.*, vol. 3, no. 8, pp. 1341–9, Jan. 2008.

[3] J. Zeng, M. Hu, W. Wang, H. Chen, and Y. Qin, "NO2-sensing properties of porous WO3 gas sensor based on anodized sputtered tungsten thin film," *Sensors Actuators B Chem.*, vol. 161, no. 1, pp. 447–452, Jan. 2012.


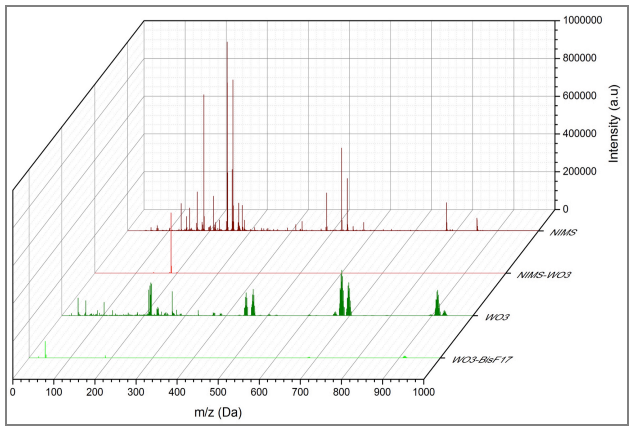


**Fig. 1**. Background noise of the analyzed surfaces.

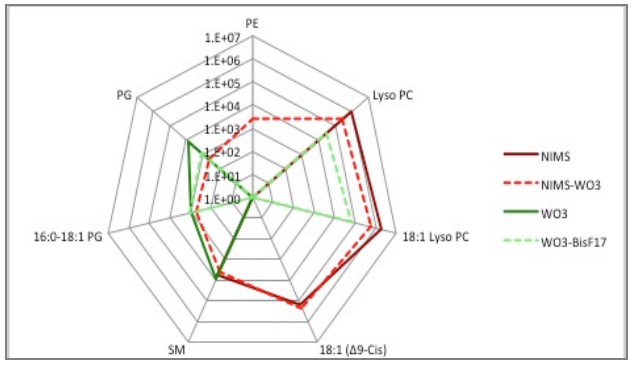


**Fig. 2.** Intensity response of the Lipid standard compounds.

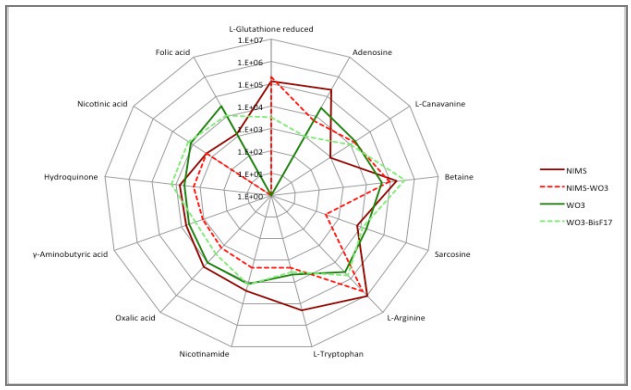


**Fig. 3.** Intensity response of the Polar standard compounds. All the surfaces work in the same intensity range.

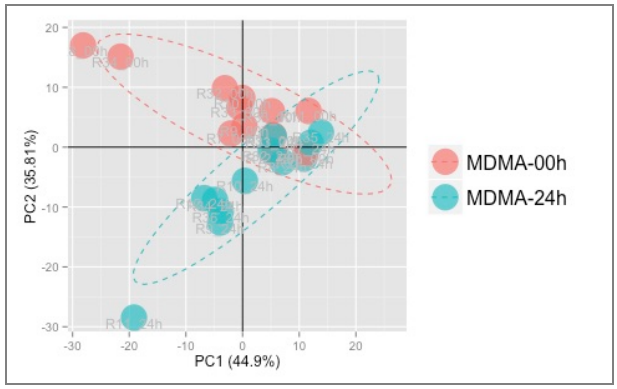


**Fig. 4.** PCA between the two classes (Before (Red) and after 24h (Blue) of the MDMA administration) using the $WO_3$ surface.